2011

Thermal diffusivity determination in SN-based lead-free solder alloys

Manijeh Mohammad Alipour

THERMAL DIFFUSIVITY DETERMINATION IN SN-BASED LEAD-FREE SOLDER ALLOYS

by

MANIJEH MOHAMMAD ALIPOUR

A DISSERTATION

Submitted in partial fulfillment of the requirements
for the degree of Doctor of Philosophy
in
Materials Science
in
Department of Materials Science
to
The School of Graduate Studies
of
The University of Alabama in Huntsville

HUNTSVILLE, ALABAMA

2011

In presenting this dissertation in partial fulfillment of the requirements for a doctoral degree from the University of Alabama in Huntsville, I agree that the Library of this University shall make it freely available for inspection. I further agree that permission for extensive copying for scholarly purposes may be granted by my advisor or in his absence, by the Chair of the Department or the Dean of the School of Graduate Studies. It is also understood that due recognition shall be given to me and to The University of Alabama in Huntsville in any scholarly use which may be made of any material in this dissertation.

M. Alyoun 7/15/11

(Student signature) (Date)

DISSERTATION APPROVAL FORM

Submitted by Manijeh M. Alipour in partial fulfillment of the requirements for the degree of Doctor of Philosophy in Materials Science and accepted on behalf of the Faculty of the School of Graduate Studies by the dissertation committee.

We, the undersigned members of the Graduate Faculty of The University of Alabama in Huntsville, certify that we have advised and/or supervised the candidate on the work described in this dissertation. We further certify that we have reviewed the dissertation manuscript and approve it in partial fulfillment of the requirements for the degree of Doctor of Philosophy in Materials Science.

Committee Chair

Dr. Michael Banish

(Date)

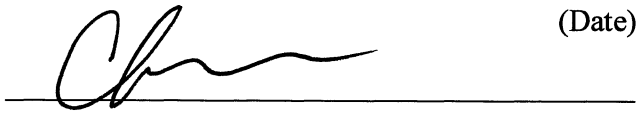

Dr. C. P. Chen

Dr. Ramon Cerro

Dr. Robert Naumann

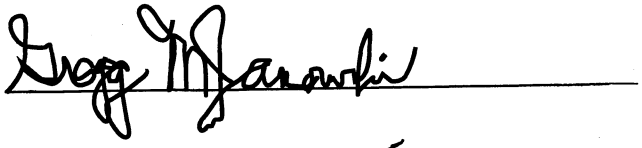

Dr. Gregg Janowski

Department Chair

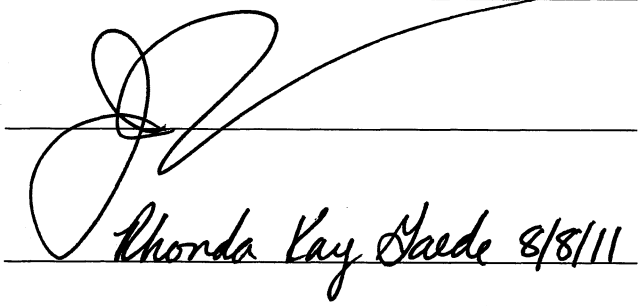

College Dean

Rhonda Kay Gaede 8/8/11

Graduate Dean

ABSTRACT

The School of Graduate Studies
The University of Alabama in Huntsville

Degree: Doctor of Philosophy College/Dept.: Science/Materials Science
Name of Candidate: Manijeh Mohammad Alipour
Title: Thermal Diffusivity Determination in Sn-based Lead-free Solder Alloys

The thermal diffusivities of three Sn-based solder alloys (Sn-3%wtAg-0.5%wtCu, Sn-4%wtAg-0.5%wtCu, and Sn-3.8%wtAg-0.7%wtCu), were determined from room temperature to up to 120°C. In addition to the lead-free alloy, the thermal diffusivity of the binary constituent alloys Cu_6Sn_5 and Ag_3Sn were measured over the same temperature range. For these studies, cylindrical samples of 6cm diameter and 1cm thickness were used. The temperature and the resulting thermal diffusivities were measured at seven different points of each sample in 5-10°C intervals. The heat pulse used leads to a 3-5°C temperature increase during the measurement. The thermal diffusivity between each two points is calculated using the logarithm gradient of the measured temperature difference between each pair versus time. The thermal diffusivity of the binary alloys showed a slight increase in thermal diffusivity with increasing temperature. This is opposite behavior from Sn matrix that has a rather strong decrease in thermal diffusivity with increasing temperature. In the lead-free alloys substantial differences were observed in the thermal diffusivity in both the different locations and sample temperatures. In some cases these differences were close to 300%. COMSOL Multiphysics was used to simulate the experiment and the heat flow in different phases in the sample and the effects of size, distribution and direction of the intermetallic

phases and grain boundary mismatch on the overall thermal diffusivity. The experimental differences observed between the thermal diffusivities of different measurement pairs in each sample are explained by the study of the microstructure and the presence of intermetallic compounds and dislocations in the structure.

Abstract Approval: Committee Chair _____

Department Chair _____

Graduate Dean Rhonda Kay Gaede 8/8/11

ACKNOWLEDGMENTS

I would like to express my sincere gratitude to my advisor, Dr. Michael Banish, for his guidance and support throughout my years at UAH. This work would have never been possible without his wisdom, care and inspiration. I would also like to thank my other committee members, Dr. C. P. Chen, Dr. Ramon Cerro, Dr. Robert Naumann and Dr. Gregg Janowski for their help and support during the preparation of this work and also during my studies at UAH.

Others I would like to thank for their support during the course of this work are the department of Chemical Engineering, Dr. Robert Lindquist, Dr. Richard Rhodes and the Office of the Vice President for Research and the Research Institute for their financial support, and Mr. Ron Carter from Nextek. I also appreciate Dr. John Williams for providing and helping me with COMSOL, and last but not least, Mr. Trevor Bowers who never hesitated to help me with his extensive knowledge of Lead-free solder alloys.

Also, I would have not been able to finish this work without the encouragement and help of my family and best friends; my parents, Farzaneh and Masoud, for the unconditional love and support they gave me all my life. Even though they could not be here with me, the thought of them always kept my heart warm and helped me go forward. Also my beloved brother, Siavash, whose presence here made Huntsville a second home away from home for me, and my lovely Hooman who, apart from his nonstop encouragement and kindness, helped me whenever my knowledge in computers came up short.

TABLE OF CONTENTS

Page

LIST OF FIGURES

Figure Page

LIST OF TABLES

LIST OF SYMBOLS

Symbol	Definition
T	Temperature
r	Radial coordinate
R	Radius of the sample
T_i	Temperature at position i
ΔT_{ij}	Temperature difference between positions i and position j
t	Time
t_e	Time at the end of pulse
κ	Thermal diffusivity
K	Thermal conductivity
ρ	Density
C_p	Heat capacity
Q''	Constant heat flux
h	Step function
J_i	Bessel function of order i
α	Roots of Bessel function
α_1	First positive root of Bessel function

CHAPTER 1
INTRODUCTION

The main goal of this research is to determine the thermal diffusivity of three of the most promising Sn-Ag-Cu solder alloys starting at room temperature to up to 120^0C. These alloys are Sn-3%wtAg-0.5%wtCu (SAC305), Sn-4%wtAg-0.5%wtCu (SAC405), and Sn-3.8%wtAg-0.7%wtCu (SAC387) which are the hypoeutectic, hypereutectic, and eutectic compositions, respectively. The method used to determine the thermal diffusivity is one developed by Brantschen et al. and used on Stainless Steel and later used by Hernandez for Portland cement. An earlier version of this work was first done by Pourpoint and Banish and applied on graphite. This method is later explained in Chapter 2 of this work.

The thermal diffusivity measurements were performed on the three alloys twice within one year's time, and also on the intermetallic compounds formed at this composition. The thermal diffusivity of the intermetallic compounds present in these alloys has not been measured before and is done for the first time in this work. These compounds are introduced and explained in Section 1.4. After the thermal diffusivity values for all alloys were determined experimentally, the microstructures were studied carefully to explain the results. At the end, the experimental procedure was modeled by COMSOL Multiphysics and the outcome was compared to the experimental results.

Section 1.1 of the introduction explains thermal diffusivity and its importance in electronics applications. Also the common methods of thermal diffusivity measurement are explained in this section. Section 1.2 briefly explains the procedure used in this method to determine the thermal diffusivity and shows the results of the previous work using this method. In Section 1.3 the importance and applications of lead-free solder alloys in electronics industry is elaborated and Sn-Ag-Cu alloys (SAC in short) are introduced as good candidates to substitute Sn-Pb alloys. These alloys are studied in detail in Section 1.4 to show the composition, phase diagrams, and the intermetallic compounds existing at these compositions. In Section 1.5 the previous work on lead-free solder alloys is reviewed and the results of the effects of different parameters on thermal and mechanical properties and microstructure are briefly reported. Section 1.6 contains a short review of dislocations and their effects on mechanical and thermal properties, and Section 1.7 concludes the first chapter with objectives and outlines.

The analytical method and the mathematical formulation are summarized in Chapter 2 to fully elaborate the reason behind the algorithm used to determine the thermal diffusivity from the experimental temperature versus time results.

In Chapter 3 the sample preparation, experimental set-up and test procedures are shown in detail and the process of data acquisition is explained. The steps of surface preparation for microstructure determination and also the differential scanning calorimetry are also shown in this chapter.

Chapter 4 shows the results and discussion, and Chapter 5 explains the simulation process using COMSOL Multiphysics. Chapter 6 is the conclusion.

1.1 Thermal Diffusivity

Thermal diffusivity is defined as the thermal conductivity divided by the volumetric heat capacity of the material, and is shown with α, κ or D (κ is used in this work). The units of thermal conductivity, density and specific heat capacity are W/m.K, kg/m^3, and J/ (kg·K respectively, so according to equation (1.1) the unit for thermal diffusivity is m^2/s (or cm^2/s).

$$\kappa = \frac{k}{\rho\, Cp}, \tag{1.1}$$

where k is the thermal conductivity (W/m.K).

Thermal diffusivity is in essence the measure of a material's transient thermal response to a change in temperature, in other words, how rapidly a material can adjust its temperature to that of the surroundings.

Agustin Salazar [1] has highlighted the difference between thermal conductivity and thermal diffusivity which is summarized here. While the meaning of k is very well-known, the role of κ is usually undervalued and misunderstood. For instance, it is well known that the thermal conductivity of a metal such as Ni is higher than the thermal conductivity of a polymer and that this is higher than that of air. In contrast, it is not nearly as well known that Ni and air have the same thermal diffusivity. It should be noted that in the modeling of heat transfer, the thermal diffusivity is not the parameter actually used. Most codes ask for the inputs of thermal conductivity, density, and specific heat capacity separately, all of which could have individual errors associated with them.

Whenever there is a temperature gradient ($\triangle T$) into a material, a heat flow of q is established that is given by Fourier's law, which in the case of homogeneous and isotropic materials is as follows [2]:

$$q = -K\nabla T. \tag{1.2}$$

According to equation (1.2), thermal conductivity shows the heat flowing in unit time through a unit area of a layer of the material of unit thickness with unit temperature difference between its faces. This means that a good thermal conductor such as Cu or diamond in contact with a thermal source at high temperature extracts from it much more energy per unit time than a bad conductor such as a polymer or a gas.

The values of thermal conductivity (k) and thermal diffusivity (κ) for some common materials are shown in Table 1.1 [24-33].

Table 1.1 The values of thermal conductivity and thermal diffusivity of some common materials

Material	k (W/m.K)	κ (m^2/s)
Air	0.024 – 0.0457	2.21×10^{-5}
Wood	0.09 – 0.4	8.2×10^{-8}
Alcohol	0.1 – 0.212	7×10^{-8}
Rubber	0.16	1.3×10^{-7}
Water	0.563 – 0.609	1.4×10^{-7}
Stainless Steel	16.3 – 24	4.2×10^{-6}
Copper	353 – 401	1.12×10^{-4}
Aluminum	204 – 249	8.4×10^{-5}
Gold	314 – 318	1.27×10^{-4}
Silver	406 – 430	1.65×10^{-4}

For a homogenous and isotropic medium with temperature-independent thermal properties and no heat generation inside, the differential equation of heat conduction is as follows [2]:

$$\nabla^2 T - \frac{1}{\kappa}\frac{\partial T}{\partial t} = 0\,. \tag{1.3}$$

Thermal diffusivity, κ, is the quantity that measures the change in temperature produced in unit volume of the material by the amount of heat that flows in unit time through a unit area of a layer of unit thickness with unit temperature difference between its faces (the speed of propagation of heat during changes of temperature over time).

In Figure 1.1 the thermal conductivity is represented against the thermal diffusivity for some homogeneous materials: metals (closed circles), ceramics (squares), glasses (triangles), polymers (open squares) and liquids (open circles) [1]. It can be seen that the line passing through the points is not an absolute straight line, showing that in some cases, higher thermal conductivity might not translate directly to higher thermal diffusivity.

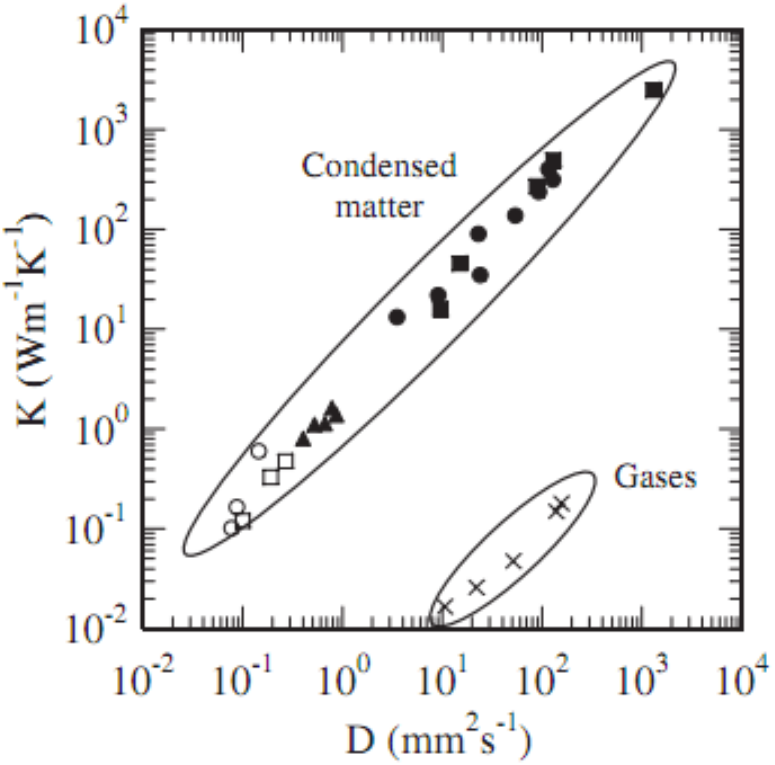

Figure 1.1 Thermal conductivity versus thermal diffusivity for homogeneous materials (closed circles, metals; squares, ceramics; triangles, glasses; open squares, polymers; open circles, liquids; and crosses, gases)

In order to determine the solidification process, as well as practical applicability and determination of the safe operating temperature of different metals, the knowledge of their thermophysical properties (thermal diffusivity in this case) is essential.

There are different conventional methods of determining thermal diffusivity. These methods either use the transient or periodic heat flow and study the temperature change as the heat is applied to the sample. Some of the most common methods are explained below.

Laser Flash Method

The best established method in thermal diffusivity measurement is laser flash method which is based on the analytical solution of the heat conduction problem within a plate that is heated on one or two surfaces by a heat pulse. The schematic of the experimental set-up in this method is presented in Figure 1.2 [3]. This method was first proposed by Parker et. al. of the U.S. Navy Radiological Defense Laboratory in 1960 [4]. In this method the sample was heated by a short heat pulse on the front face, and the temperature rise was measured on the other face. The temperature raise versus time data was then used to determine the thermal diffusivity. This was done by matching an analytical profile with the experimental data which required the knowledge of the temperature and energy profile applied to the samples.

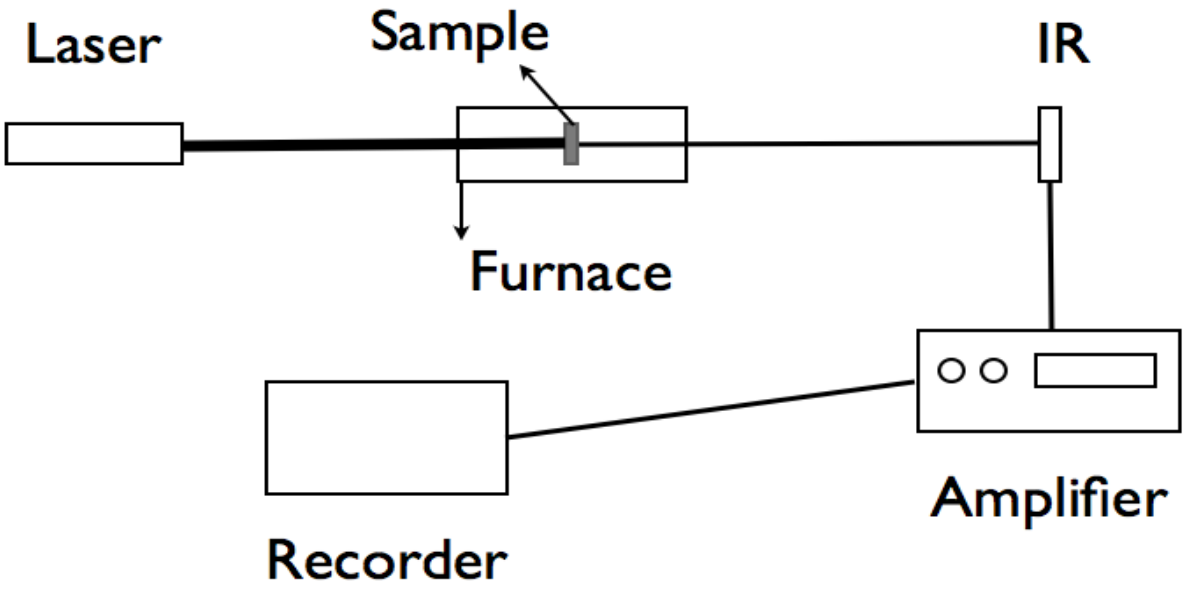

Figure 1.2 The schematic of the experimental set-up in laser-flash system

Thermal Wave Interferometry

Thermal wave interferometry (TWI) is another well-established method of thermal diffusivity measurement. This method is mainly used for coatings and thin slabs [5]. In this method, the propagation of thermal waves between the two surfaces of the material is measured. The interference between propagating and reflected waves changes the phase and the amplitude of the ac component of the surface temperature. Figure 1.3 shows the schematic set-up of the TWI apparatus.

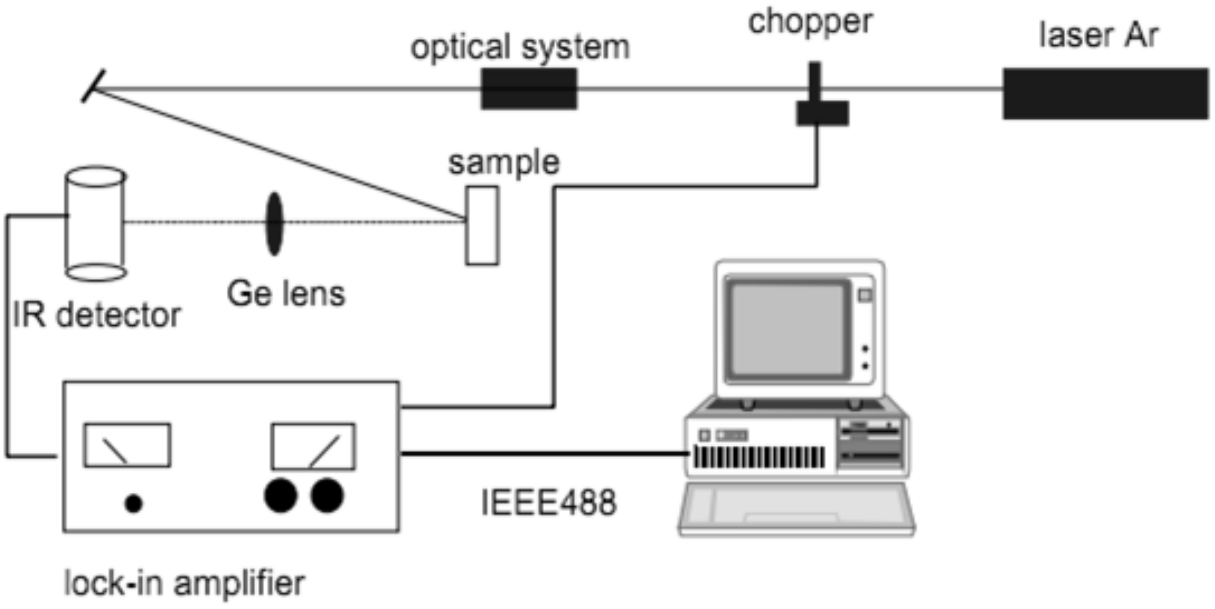

Figure 1.3 The schematic set-up of TWI apparatus

There are other methods of thermal diffusivity measurement such as Thermographic methods (spatially resolved method, lateral thermal waves method, and single side flash method), Angstrom method, etc., which are available in the literature [5, 6, 7].

1.2 Current Method and Previous Work

The method that is used in this work was first developed by Pourpoint et al. for graphite and boron nitride in 2000 [8] and was later used by Brantschen for stainless steel [9] and Hernandez for Portland cement [10]. Pourpoint's methodology used a central heated region and 3 measurement locations while Brantschen's method is similar to this work with heat applied from the walls of the sample and the heat measured at 2 points. The method uses a reduced solution for thermal diffusivity in a cylindrical geometry

using specific measurement locations. A cylindrical sample is isolated from the top and bottom surface to work like an infinite cylinder in which the heat only depends on the radius. The heat pulse is applied from the cylinder wall and the temperature at 7 measurement points on the sample is recorded with respect to time. Then the reduced solution which will be explained in details in Chapter 2 shows that plotting the natural logarithm of the temperature difference at each measurement pair versus time will produce parallel lines the slope of which have a linear correlation with the thermal diffusivity value. The slope of $ln\Delta T$ versus time is used to determine the thermal diffusivity in the sample, and the results are shown in Figures 1.4 to 1.6. The advantage of this method is the fact that there's no need to know the heat flux and the only information needed to determine the thermal diffusivity is the temperature versus time profile after the heat pulse.

Figure 1.4 shows the results for the natural logarithm of the temperature difference versus time in stainless steel [9]. Also Figure 1.5 shows the temperature dependence of thermal diffusivity in the case of stainless steel and compares the results from Brantschen with other published results.

It can be seen in Figure 1.4 that after the heat pulse is finished and the thermocouples come to equilibrium temperature, the $ln\Delta T$ versus time lines become almost perfectly parallel and result in four very close values of thermal diffusivity.

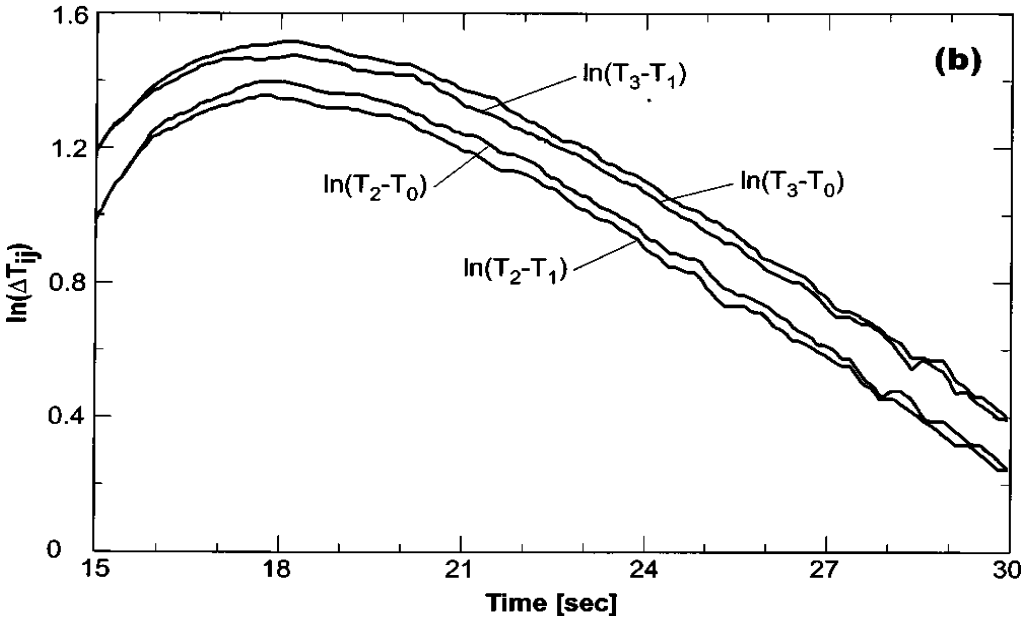

Figure 1.4 The values of $ln\Delta T$ versus time for Stainless Steel for 4 different measurement pairs. The slope of the parallel section is used to determine the thermal diffusivity

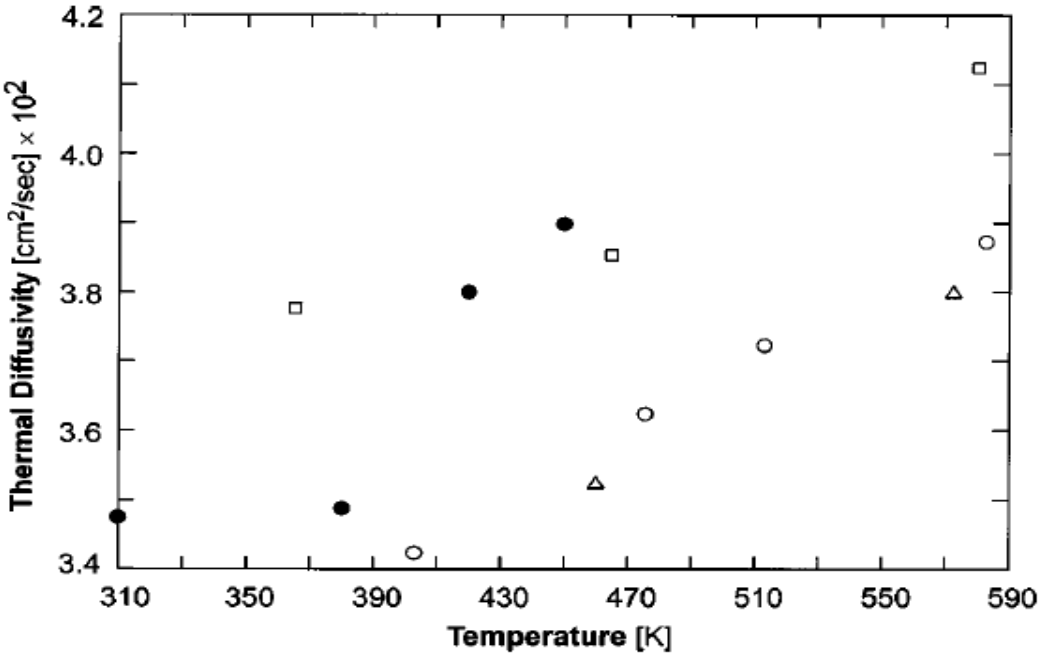

Figure 1.5 Thermal diffusivity values at room temperature and above. Solid circles are the result of the current method for 304 stainless steel [9].

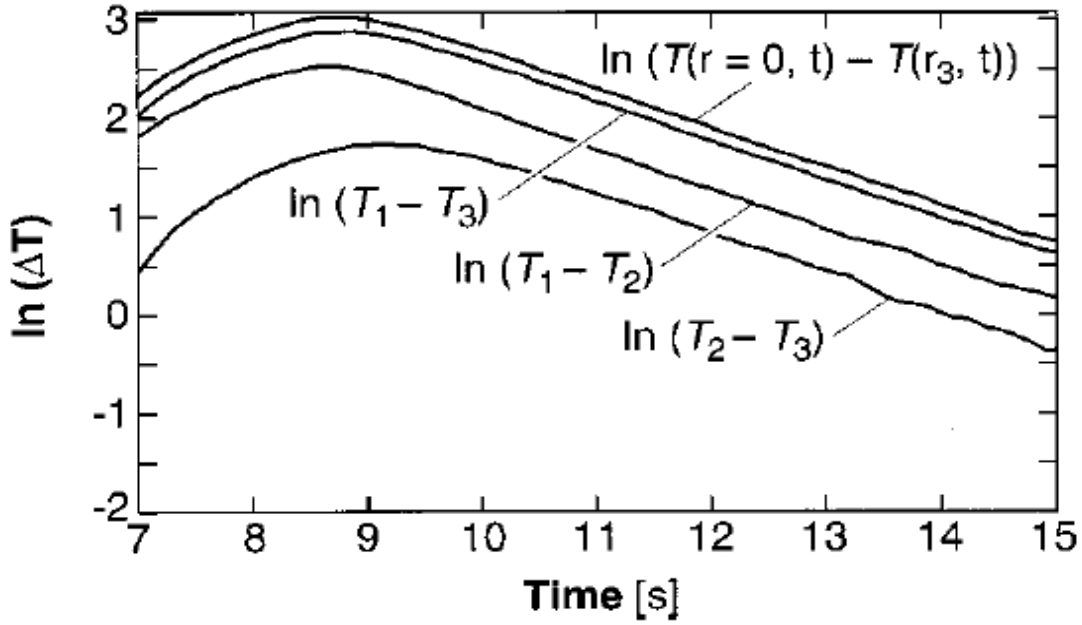

Figure 1.6 The values of lnΔT versus time for Graphite for 4 different measurement pairs. The slope of the parallel section is used to determine the thermal diffusivity [8].

Figure 1.5 shows the dependence of thermal diffusivity on temperature. The solid circles are the values from Brantschen and triangles, squares and empty circles are from the literature.

Figure 1.6 shows the results for graphite [8]. This graph also confirms the precision of the method with parallel lines of $ln\Delta T$ versus time after the equilibrium temperature is reached.

The current work applies the same principles and experiment set-up on three different lead-free, tin-based solder alloys and their intermetallic compounds and the results will be compared with the previous work later in Chapter 4.

1.3 Lead-Free Solder Alloys

Since European Restriction of Hazardous Substances (RoHS) and Waste in Electrical and Electronic Equipments (WEEE) banned the use of Pb in electronics in 2006, extensive research has been conducted to find the best substitute for Pb solder alloys.

The main criteria that the substitute alloy has to meet are summarized by Seelig [11]. The substitute alloy should not have any environmental toxicity or negative impact. The base material must be available in sufficient quantity for future productions. The melting point should be similar to that of the SnPb eutectic alloy (preferably less than 200°C). The thermal and electrical conductivity should be similar, and mechanical properties such as joint strength and thermal fatigue should be satisfactory. The alloys need to be low cost and compatible with the current processes. Due to the numerous requirements of the substitute alloy, there has not been a single alloy chosen to be the best option yet. Depending on the property (wetting, creep, fatigue, thermal conductivity, etc.) that is being compared for different possible substitutes, a different optimum compound is suggested in different studies which are not in agreement in all cases. This is why a universal compound has not been agreed on yet. The alloys studied most as possible substitutes have been SnAg, SnAgBi, SnAgCu, SnZn, SnCuIn, and SnAg-BiCuGe. SnAgCu alloys have shown to be the most promising option among the proposed alloys [13]. Japan has chosen Sn-3%Ag-0.5%Cu as the optimum option, where the EU has chosen the eutectic composition of Sn-3.7%Ag-0.8%Cu and the US has been using the Sn-3.9%Ag-0.6%Cu alloy [12]. One of the issues in the use of lead free solder alloys is that there are a multitude of alloys that have very similar melting points. This is

a severe problem in circuit boards repair. Unless the board is exactly matched with the lead-free solder alloy used, a repair process may lead to mixed solders and different mechanical and thermal failures on the board, even within individual components on the board. Some of the results from these studies will be shown in Section 1.5.

1.4 Sn-Ag-Cu Solder Alloys

As was mentioned before, according to previous research, Sn-Ag-Cu (SAC for short) alloys seem to be the best substitutes for Sn-Pb alloys. The phase diagram of these alloys is presented in Figure 1.7. Since the amounts of Ag and Cu in the alloys of interest in this research are small, the Sn-rich region of the phase diagram is shown separately in Figure 1.8. The area of interest in this work is shown with a red circle in Figure 1.7. The exact composition of the three alloys used in this research is shown with red dots on Figure 1.8. The composition of the alloys is shown in Table 1.2. Note the melting temperature "range" in the Table, which shows the uncertainty in the melting temperature and the eutectic point in the literature.

Table 1.2 The alloy compositions used in this work

	Sn (wt%)	**Ag (wt%)**	**Cu (wt%)**	**Melting temperature (°C)**
SAC305 (hypereutectic)	96.5	3	0.5	217-218
SAC405 (hypoeutectic)	95.5	4	0.5	217-218
SAC387 (eutectic)	95.5	3.8	0.7	217-218

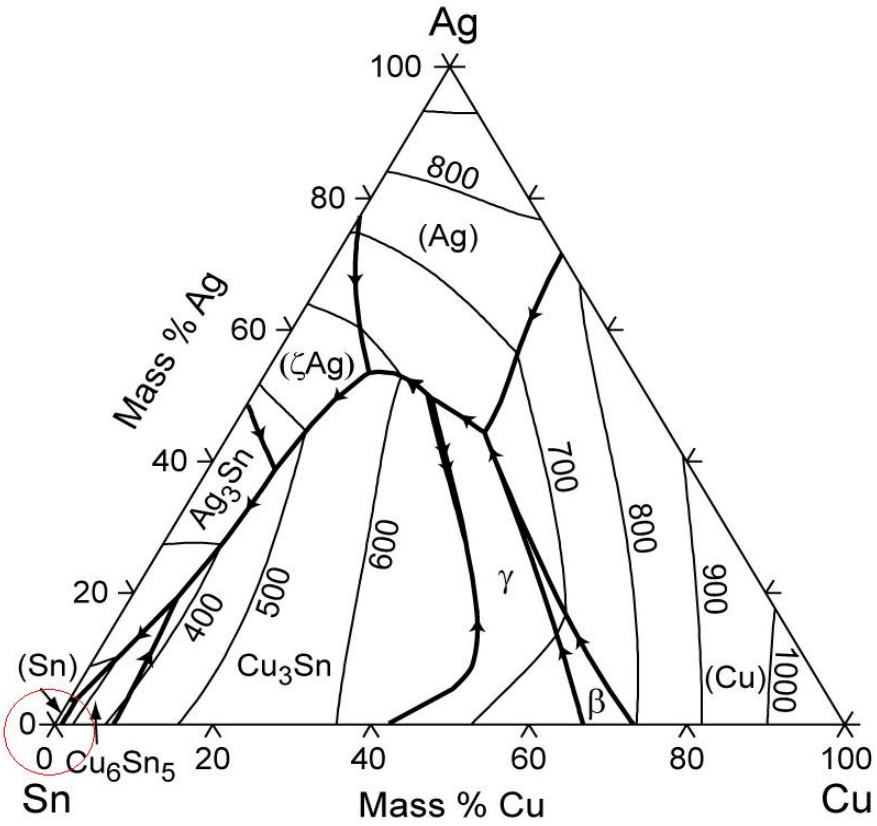

Figure 1.7 The ternary phase diagram of Sn-Ag-Cu. The area where the alloys in this work lie is shown by the red circle [23].

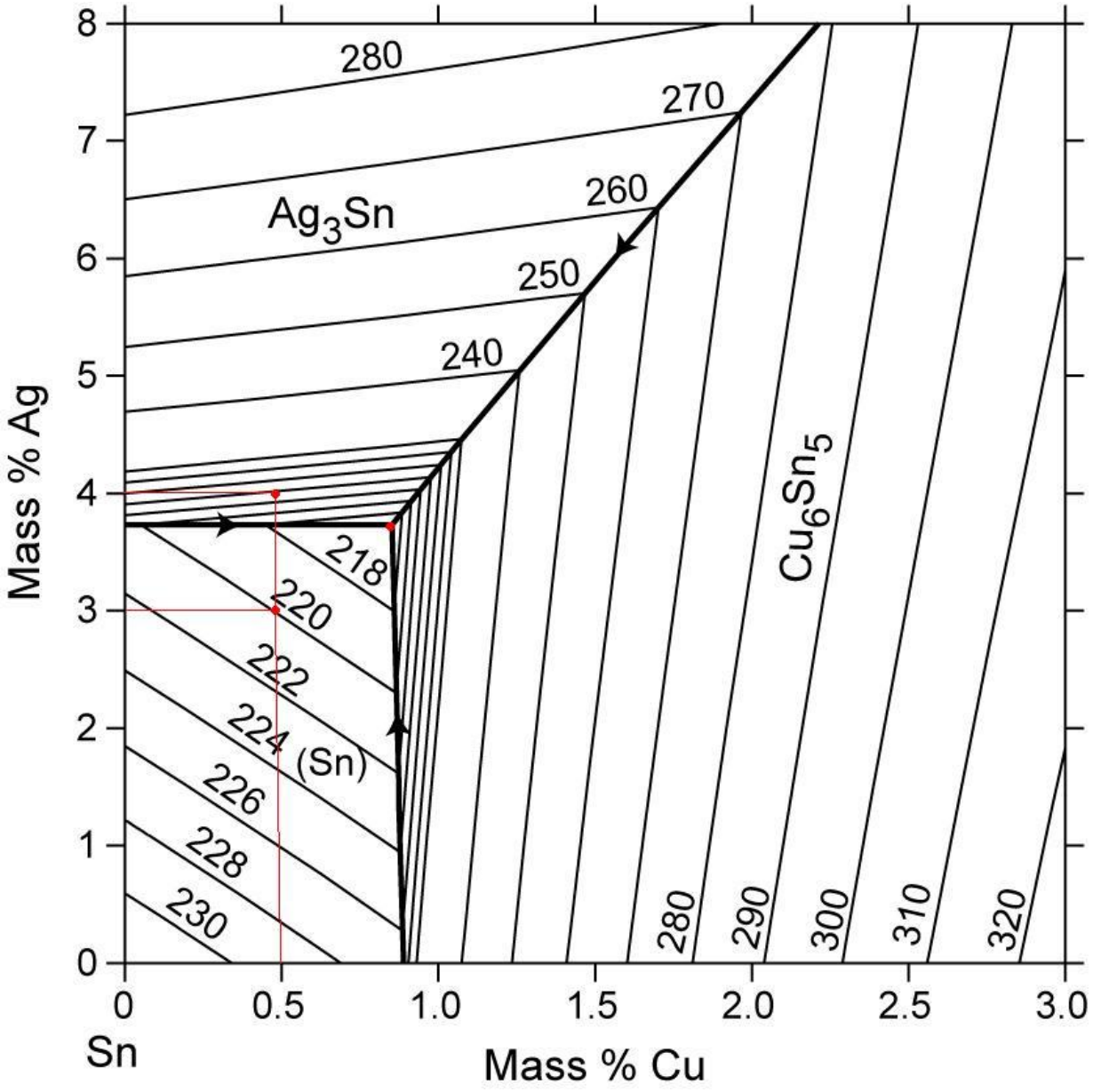

Figure 1.8 The Sn-rich section of the Sn-Ag-Cu phase diagram. The alloys used in this work are shown with red dots [23].

The compositions in Table1.1 are shown with red dots in Figure 1.8. The eutectic compound is easily recognizable at the point of 0.7%Cu and 3.8%Ag. And the other two compounds are the hypo (before) and hyper (after) eutectic compounds. These alloys are going to be called SAC387, SAC405 and SAC305 from now on.

The phase diagram also shows the intermetallic compounds that exist at this composition. It can be seen that Cu_6Sn_5 (η phase), Ag_3Sn (θ phase) and Sn (β phase) are the main compounds present. The same experimental procedure was performed on these intermetallic compounds to determine their thermal diffusivity, which to the best knowledge of the author is something that has not been done before.

The effects of these intermetallic compounds (IMCs) on different solder properties have been studied by different research groups. The overall results show that the properties strongly depend on the size and orientation of these compounds. The size of these intermetallic compounds depends on the alloying composition and the cooling rate. Some of the research carried out on the effect of intermetallic compounds and microstructure on the properties, and the effect of different parameters on the size and shape of these phases are summarized in Section 1.5.

1.5 Intermetallic Compounds and Solder Properties

Park et al. [14] report that since Sn and SAC alloys in general, have anisotropic properties, the orientation and the number of grains strongly affects the failure of SAC alloys.

They studied fatigue along different directions in the joint and observed that fatigue

cracks propagate along the grain boundaries and the IMCs where the movement of dislocations is limited.

Sundelin et al. [15] studied the microstructure of the IMCs for different compositions and substrates, and also investigated the effect of cooling rate and aging on shear strength. They concluded that slower cooling rate increases the size of Ag_3Sn which in turn decreases the shear strength. Also Ag_3Sn coarsens significantly with aging which decreases the shear strength.

Kung et al. [16] report that the presence of brittle intermetallic compounds has an adverse effect on the mechanical deformation properties of SAC alloys. And since fast cooling is not always practical, they suggest the addition of minute amounts of Zn to SAC alloys to reduce the amount of undercooling during solidification, thereby suppressing the formation on large intermetallic compounds. The results of this work shows that addition of 0.1% Zn to the alloy refines the microstructure considerably, thus improving the mechanical properties.

Yu et al. [20] have suggested the addition of rare earth elements to refine the structure. The results show that the addition of 0.1-0.25% of RE can refine the microstructure significantly. The micrographs of this effect are presented in Figure 1.9. They concluded that after the addition of rare earth elements, due to the fine and uniform microstructure, the tensile strength and elongation were improved. In addition, the wetting properties were also enhanced. All these results indicated that adding trace rare earth elements was an efficient way to develop new solders.

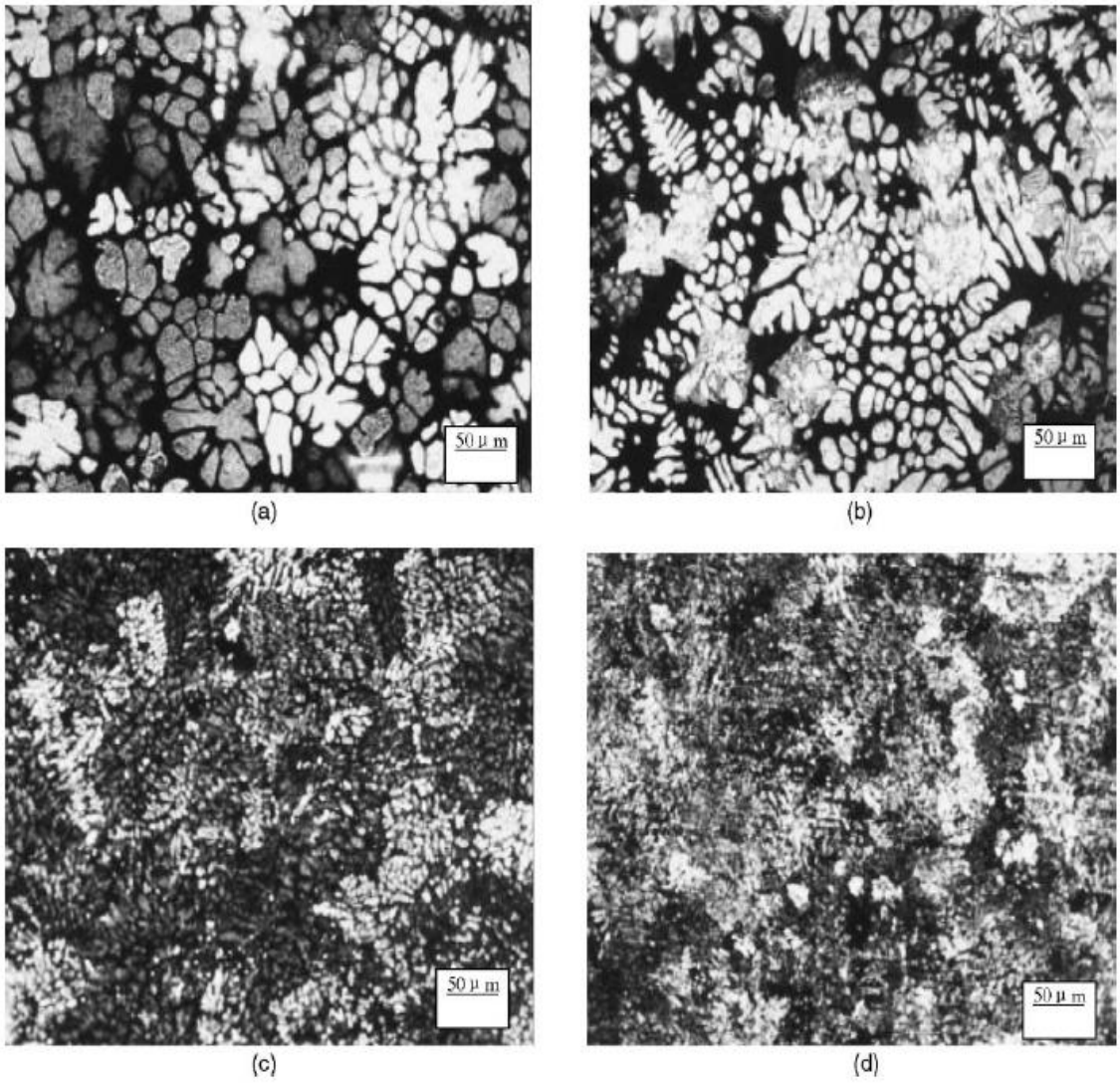

Figure 1.9 The effect of RE addition on the microstructure [20]. (a) Sn2.5% Ag0.7% Cu; (b) Sn3.5% Ag0.7% Cu; (c) Sn3.5% Ag0.7% Cu0.1% RE; and (d) Sn3.5% Ag0.7%Cu0.25% RE.

There are multiple studies [17, 18, and 19] that investigate the effect of aging and thermal cycling on the size of intermetallic compounds and they all agree that aging and thermal cycling increases the size of the IMCs which in turn affects the grain boundary and the density of dislocations which will be discussed in Section 1.6.

1.6 Dislocations

Dislocations are crystallographic defects or irregularities within the crystal structures. In 1940 both Bragg and Burgers introduced the theory that the boundaries between crystals of the same structure can be considered as arrays of dislocations. If two grains have even the slightest difference in their orientation, a dislocation model can be drawn for the boundary. The greater the angular rotation of one crystal relative to the other, the greater is the inclination of the crystallographic planes that terminate as dislocations at the boundary [34]. The mechanical properties of polycrystalline metals usually show a strong dependence on grain size. The smaller the grain size, the greater is the hardness or flow-stress. There is a linear relationship between the flow-stress and the square root of the dislocation density proposed by Hall and Petch [35, 36].

The effects of dislocations and grain boundaries on different properties of crystalline solids have been studied for many years. Since the main subject of this work is the thermal diffusivity measurement, some examples of other work on the effect of dislocations on thermal properties are presented in this section. Hopkins et al. [37] investigated the effect of dislocation density on thermal boundary conductance across GaSb/GaAs interfaces. The results showed that the thermal boundary conductance across the GaSb/GaAs interfaces decreases with increasing strain dislocation density.

Voyiadjis et al. [38] studied the effect of dislocation density evolution on the thermomechanical response of metals with deferent crystal structures at low and high strain rates and temperatures. A model was proposed based on the thermal activation energy and dislocation interaction mechanisms. The simulation was performed for bcc, fcc and hcp metals at high and low strain rates and temperatures. The results of the simulations are in good agreement with experimental results from other work on different metals with different crystal structures. In bcc metals, the thermal yield stress shows strong dependence on the strain rate and temperature. The thermal stress in fcc metals is strongly dependent on the plastic strain due to domination of the dislocation intersections on the mechanisms behavior of the thermal activation analysis. In hcp metals the thermo-mechanical behavior shows a combination between the plastic deformation behavior of both bcc and fcc structures.

1.7 Objectives and Outline

As it was mentioned before, the thermal properties of SAC alloys have not been investigated as well as their mechanical properties. And since the importance of the knowledge of heat propagation and thermal diffusion in solder joints is known, and the consistency of the results of the proposed method has been shown before, the following work will focus on determining the thermal diffusivity of the three abovementioned alloys and their intermetallic compounds, and the effects of these IMCs, their size, distribution and direction on the overall thermal diffusivity with both experimental and simulation methods.

CHAPTER 2
ANALYTICAL METHOD

In this chapter, the derivation of the equation used in determining the thermal diffusivity using the temperature versus time data is explained using the work of Brandtschen et al. In Section 2.1, an infinite series solution is developed based on an isolated cylinder heated from the walls. In Section 2.2 the simplified results that determine the measurement points on the sample which yield in a linear equation are shown, and in Section 2.3, numerical models are presented that determine the ideal temperature profile shape and the resulting temperature gradient between each measurement pair.

2.1 Mathematical Formulation

In this setup, a cylinder with insulated top and bottom faces is assumed to be heated on the walls. Since there is no heat exchange from the two faces, the problem is similar to the case of an infinite cylinder where the temperature gradient only depends on *r*, the radius of the cylinder. Furthermore, the cylinder is assumed to be axially symmetric so there's no angular dependence. This setup is shown in Figure 2.1.

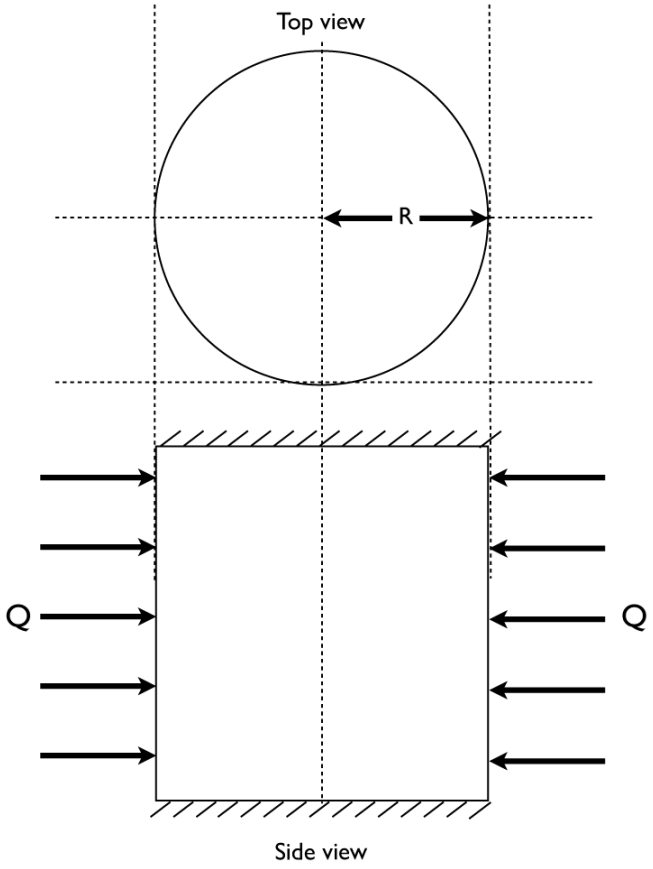

Figure 2.1 Infinite cylinder of radius *R* with a constant heat flux of *Q"* applied to the walls

The initial temperature of the cylinder is assumed to be T_0 and the constant heat flux of *Q"* is applied to the surface from time 0 to t_e. The dependence of the temperature on position and time, T(r, t), is obtained from the transient form of the heat equation in cylindrical coordinates:

$$\frac{1}{r}\frac{\partial T}{\partial r} + \frac{\partial^2 T}{\partial r^2} = \frac{1}{\kappa}\frac{\partial T}{\partial t}\,. \tag{2.1}$$

The boundary conditions for this equation are

$$T(r,0) = T_0 \,. \tag{2.2}$$

And at $r=R$ the heat flux of Q'' is applied:

$$-\kappa \frac{\partial T}{\partial r} = Q"[1 - h(t - t_e)] \,. \tag{2.3}$$

Here h is the unit step or *Heaviside* function, and k is the thermal conductivity. Using Laplace transformation, T(r, t) can be written as [2]

$$T(r,t) = f(r,t) + h\,(t - t_e)\, f(t - t_e) \,. \tag{2.4}$$

The inverse Laplace transformation of this expression is determined by Carslaw and Jeager [3] as follows:

$$f = -\frac{Q"R}{\kappa}\left\{\frac{2\kappa t}{R^2} + \frac{r^2}{2R^2} - \frac{1}{4} - 2\sum_{S=1}^{\infty} e^{-\frac{\kappa \alpha_S 2 t}{R^2}} \frac{J_0\left(\frac{r\alpha_S}{R}\right)}{\alpha_S{}^2 J_0(\alpha_S)}\right\} . \tag{2.5}$$

α_s in this equation shows the positive roots of $J_1(\alpha)$. It should be noted that in equation (2.5), T_0 is assumed to be zero. In the present case, the initial temperature value is added to the result.

The Heaviside function is 0 or 1 depending on whether or not the heat is applied to the system. For this reason, the solution to the problem is divided into two cases which are presented below:

(1) For $t \leq t_e$ (during heating), the second term on the right hand side of equation (2.4) is equal to zero, so the temperature distribution can be shown as

$$T(r,t) =$$

$$-\frac{Q"R}{\kappa}\left\{\frac{2\kappa t}{R^2}+\frac{r^2}{2R^2}-\frac{1}{4}-2\sum_{S=1}^{\infty}e^{-\frac{\kappa\alpha_S 2t}{R^2}}\frac{J_0\left(\frac{r\alpha_S}{R}\right)}{\alpha_S{}^2 J_0(\alpha_S)}\right\}+T_0. \tag{2.6}$$

(2) For $t \geq t_e$ (after heating) the temperature distribution becomes

$$T(r,t) =$$

$$-\frac{Q"R}{\kappa}\left\{\frac{2\kappa t}{R^2}+\frac{r^2}{2R^2}-\frac{1}{4}\right\}+\frac{Q"R}{\kappa}2\sum_{S=1}^{\infty}e^{-\frac{\kappa\alpha_S 2t}{R^2}}\frac{J_0\left(\frac{r\alpha_S}{R}\right)}{\alpha_S{}^2 J_0(\alpha_S)}+$$

$$\frac{Q"R}{\kappa}\left\{\frac{2\kappa(t-t_e}{R^2}+\frac{r^2}{2R^2}-\frac{1}{4}\right\}= \tag{2.7}$$

$$-\frac{Q"R}{\kappa}2\sum_{S=1}^{\infty}e^{-\frac{\kappa\alpha_S 2(t-t_e)}{R^2}}\frac{J_0\left(\frac{r\alpha_S}{R}\right)}{\alpha_S{}^2 J_0(\alpha_S)}+T_0\ .$$

In our case the temperature profile is needed only after the end of the pulse. Therefore, only the relaxation modeled by equation (2.7) is studied here. Rearranging and factoring of equation (2.7) yields to the final expression for temperature distribution in the cylinder versus time:

$$T(r,t) =$$

$$-\frac{Q"R}{\kappa}\left\{\frac{2\kappa t_e}{R^2}-2\sum_{S=1}^{\infty}\left[e^{-\frac{\kappa\alpha_S 2t}{R^2}}\left(1-e^{-\frac{\kappa\alpha_S 2t}{R^2}}\right)\right]\frac{J_0\left(\frac{r\alpha_S}{R}\right)}{\alpha_S{}^2 J_0(\alpha_S)}\right\}+T_0\ . \tag{2.8}$$

2.2 Simplification and Linearization

To simplify the model, the infinite summation can be reduced by eliminating the n=2 term. This term can be zero if the temperature measurement points, r, are chosen in a way that $r\alpha_2/R=\upsilon_n$ corresponding to the first two zeros of J_0, i.e. $J_0(\upsilon_n) = 0$. The values of υ_n are 2.4048 and 5.5201, respectively. With $\alpha_2=7.01559$, this results in the two values of r for which the $n=2$ term can be eliminated:

$$\frac{r_1}{R} = \frac{\upsilon_1}{\alpha_2} = 0.342779 \tag{2.9}$$

and

$$\frac{r_2}{R} = \frac{\upsilon_2}{\alpha_2} = 0.78683\,. \tag{2.10}$$

The value for $\frac{\upsilon_3}{\alpha_2}$ would be 1.23349 which is outside of the sample ($\frac{r_3}{R} > 1$).

The $n \geq 3$ terms decay rapidly with time; therefore, they are not included in the final form of the equation. Substituting the results from equations (2.9) and (2.10) and $\Delta T_{ij}=T(ri,r)-T(rj,t)$ in equation (2.8) gives the final closed form of the temperature versus time at measurement locations as follows:

$$\Delta T_{ij} = e^{-\frac{\kappa {\alpha_1}^2 t}{R^2}} \frac{2Q"R}{k} \left(1 - e^{-\frac{\kappa {\alpha 1}^2 t_e}{R^2}}\right) \frac{J_0\left(\frac{r_i-\alpha_1}{R}\right)-J_0\left(\frac{r_j-\alpha_1}{R}\right)}{{\alpha_1}^2 J_0(\alpha_1)}\,. \tag{2.11}$$

It can be seen that in equation (2.11), only the first exponential term depends on time, while the other terms only depend on the measurement locations. Taking the natural logarithm of both sides in equation (2.11) gives the final simplified solution

$$\ln(\Delta T_{ij}) = -\frac{\kappa {\alpha_1}^2 t}{R^2} + \ln(\beta_{ij}), \tag{2.12}$$

where

$$\beta_{ij} = \frac{2Q"R}{k}\left(1 - e^{-\frac{\kappa {\alpha 1}^2 t_e}{R^2}}\right) \frac{J_0\left(\frac{r_i}{R}\right) - J_0\left(\frac{r_j}{R}\right)}{{\alpha_1}^2 J_0(\alpha_1)}. \tag{2.13}$$

Equation (2.12) is a linear function of time so the thermal diffusivity can be determined by plotting the natural logarithm of temperature differences between the two measurement points, versus time. The slope of this plot contains the constants κ, R and α_1 for a given geometry. As a result of this method, the thermal diffusivity can be determined knowing only the temperature versus time at each location. Note that in this case, the knowledge of the exact heating time or the value of heat flux is not necessary in determining the thermal diffusivity. By dividing the ΔT_{ij} term in equation (2.12) by the $\frac{2Q"R}{k}$ term in the equation (2.11), the argument of the natural logarithm can become dimensionless. At this point, the value of thermal diffusivity can be determined from the slope of the natural logarithm of the temperature difference versus time curve:

$$slope = -\kappa \frac{{\alpha_1}^2}{R^2} \quad \Longrightarrow \quad \kappa = -slope \left(\frac{R}{\alpha_1}\right)^2. \tag{2.14}$$

2.3 Numerical Model

Figure 2.2 shows the numerical solution for the temperature versus time profile of a material with thermal diffusivity of 0.09 cm^2/sec and a heat flux of $Q''=3.5$ W/cm^2. It can be seen that the heat pulse, which is 2 seconds long, reaches point *T3* first and heats it up to 3 degrees. Then it starts cooling down while the other points (T2, T1 and T0) heat up until all point come to an equilibrium temperature of 294.4K. Figure 2.3 shows the $ln\Delta T$ versus time after the temperature starts to reach equilibrium. It can be seen that the slopes of different measurement points have the same value (parallel lines), which can be used in equation (2.14) to yield in the thermal diffusivity of the material.

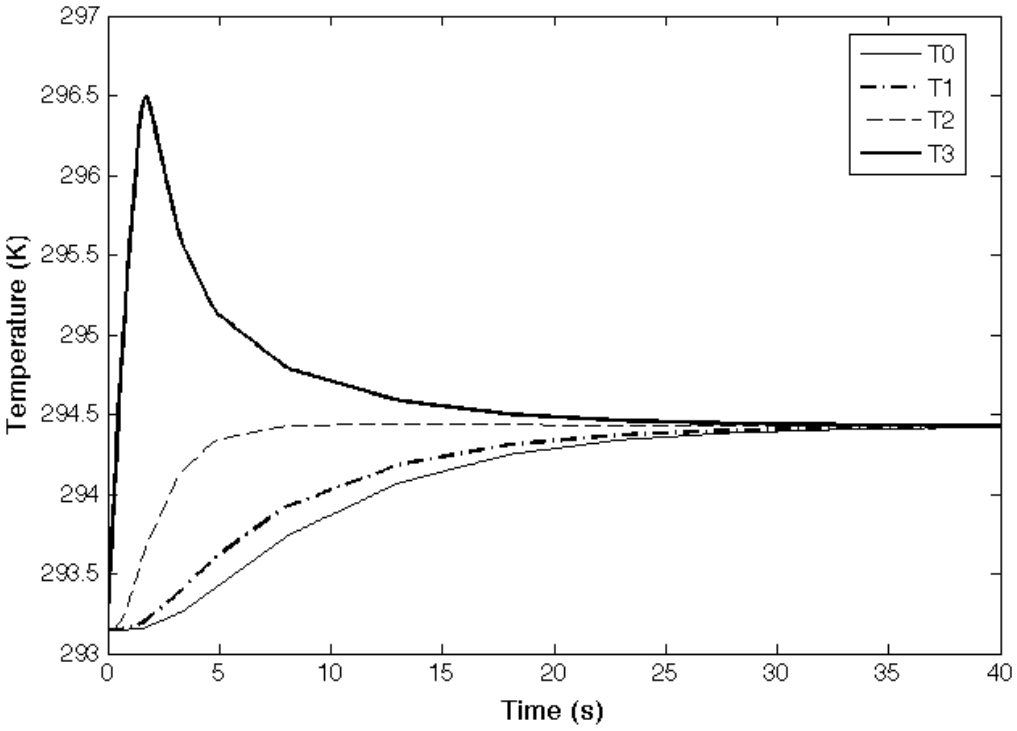

Figure 2.2 Temperature profile versus time at four measurement points (*T0, T1, T2 and T3*)

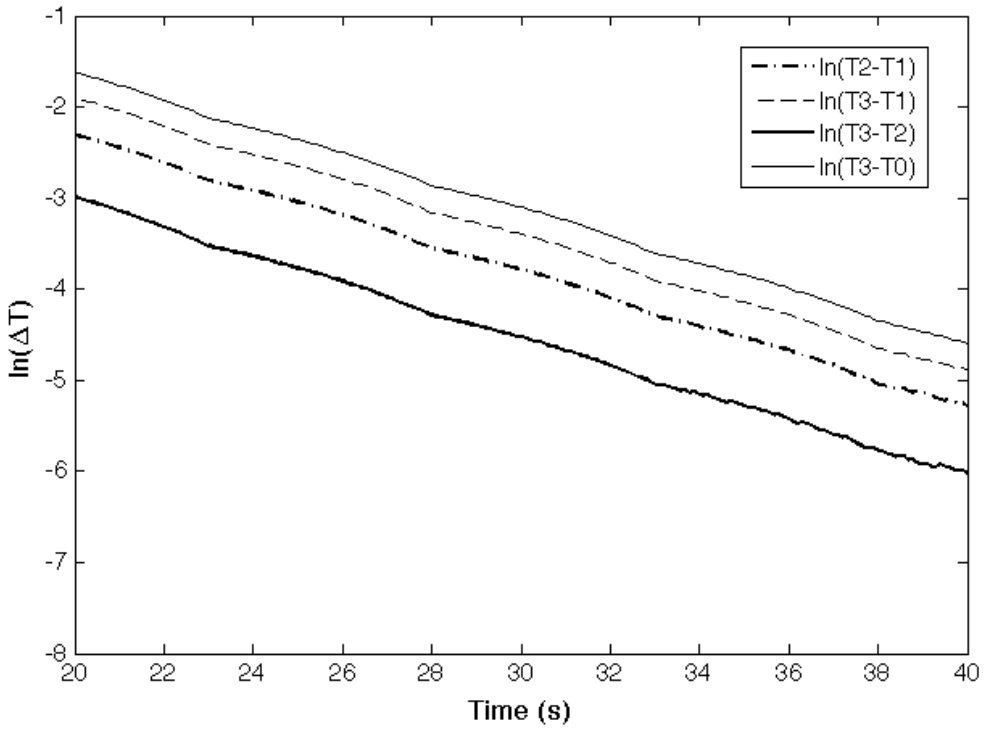

Figure 2.3 $ln\Delta T$ versus time for four different measurement pairs

CHAPTER 3
EXPERIMENTAL

In this chapter, the experimental procedure is explained. Section 3.1 describes the alloys used and the process in which they were cast and machined to the final desired shape. Section 3.2 briefly explains the DSC procedure. Section 3.3 shows the details of the experimental set-up and the equipment used to perform the tests. Section 3.4 shows the data acquisition process and how the temperature versus time data is recorded at measurement points defined in Chapter 2. Section 3.5 describes the metallography and microstructure determination method.

3.1. The Alloys

The alloys used in this experiment were the three SnAgCu (SAC) alloys Sn-3%wtAg-0.5%wtCu, Sn-4%wtAg-0.5%wtCu, and Sn-3.8%wtAg-0.7%wtCu with hypoeutectic, hypereutectic, and eutectic composition, respectively. The experiment was also carried out on Cu_6Sn_5 and Ag_3Sn intermetallic compounds purchased from Indium Corp. of America.

The alloys were received in rod form first and each was later melt on a hot plate and cast in graphite molds into a disk. They were then machined into cylinders of 3cm radius and 1cm height. A total of 7 holes was drilled 3mm deep in each sample to hold the thermocouples. One hole was drilled in the center of the cylinder face (T_0), and

3 pairs of holes were made at 1.03, 2.36 and 2.8cm (r/R= 0.343, 0.787 and 0.933 respectively) distance from the center, each having a 60 degrees rotation (Figure 3.1). The measurement points were designated as T_0 for the center point and T_1, T_2 and T_3 for the pairs.

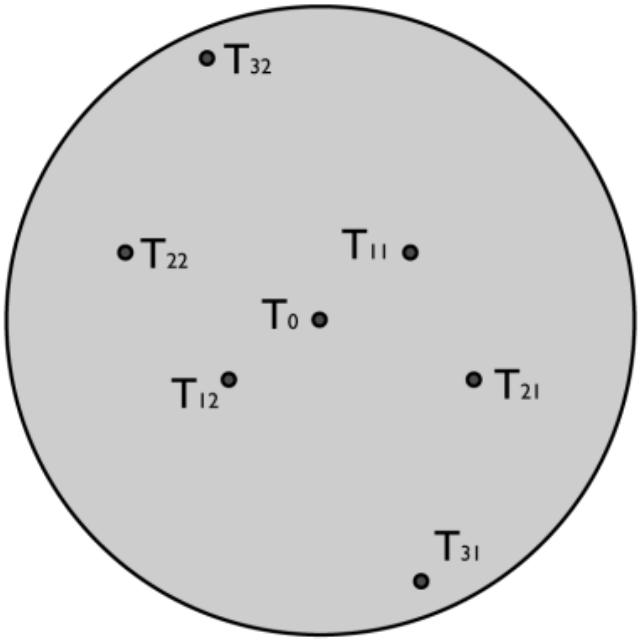

Figure 3.1 The placement of measurement points on the sample

3.2 Differential Scanning Calorimetry

Differential Scanning Calorimetry was performed using an Instrumental Specialists DSC model F5010. Samples sizes of 5 to 10 mg were used with N_2 gas and the reading speed of the machine was set to slow heating rates of 5 and 1 degree per minute to make sure that no phase change is missed.

3.3 The Experiment Set-up

The experiment set-up is shown in Figure 3.2. Minco band heaters were wrapped around the cylinder walls with no overlap, and connected to a Sorensen power source which was set to send two second long heat pulses. Shrinkage bands were used to ensure a uniform contact between the heater and the sample. The sample was mounted on a three-rod base covered with insulation to minimize the heat transfer between the sample and the base. Seven Inconel sheathed (0.1mm diameter) type E thermocouples were inserted in the drilled holes. The insertion depth of the thermocouples was at least 10 times their diameter to ensure that the measurements were good representatives of the sample bulk temperature. Thermal grease was used to provide a better contact between the thermocouples and the sample. The set-up was put in a vacuum chamber (not shown here) and 10^{-5} Torr vacuum was provided using an Alcatel CFF100 vacuum pump in order to minimize heat convection. (See Brentschen [9] for more detailed discussion of minimizing convective contributions.)

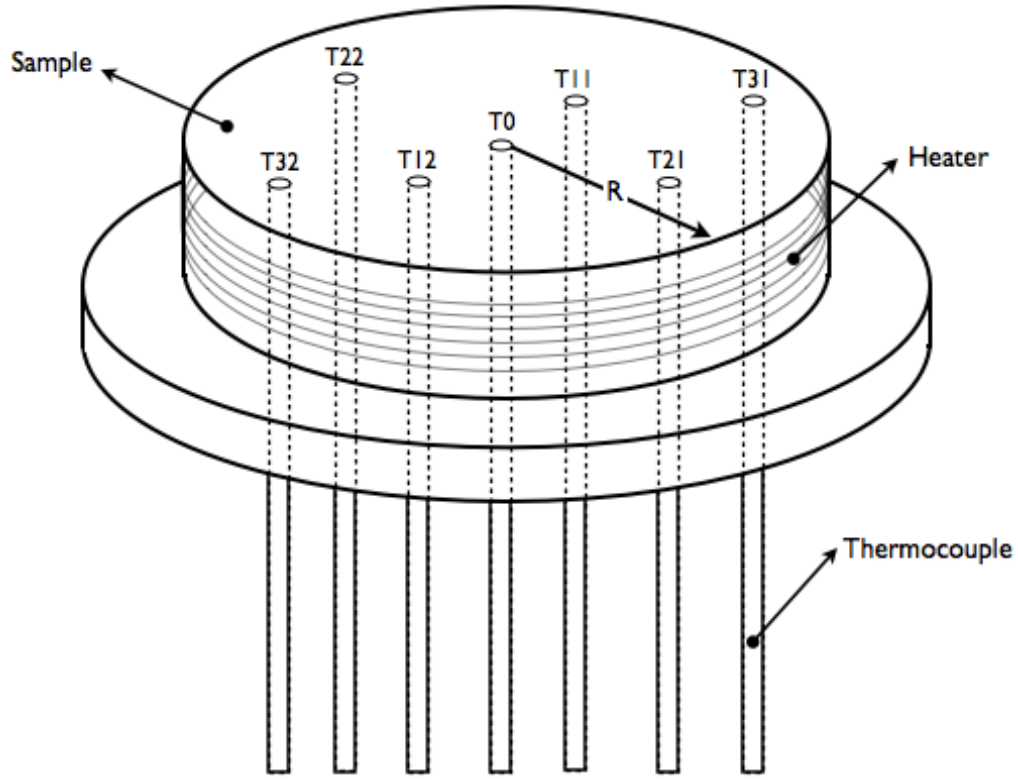

Figure 3.2 The experiment set-up

To measure the thermal diffusivity at higher temperatures, a commercial electrical heater was wrapped around the chamber and the temperature was controlled by adjusting the output voltage of the heater which was connected to a 110V outlet. The experiments were conducted from room temperature (293K) to up to 120°C (393K).

Once the samples were placed on the rods, and vacuum was provided, the heat pulse was applied for 2 seconds using the programmed Sorensen power source while an

IOtech TempScan 1000® with Tempview software was used to record the temperature of the thermocouples at 0.1 sec intervals with 0.1°C resolution. The temperature was recorded for about 40 seconds after the heat pulse, to make sure that all the thermocouples have come to equilibrium temperature.

3.4 Data Acquisition

The results from Tempview software were the temperature versus time from t=0 (before the heat pulse was applied), to t=40s (after all thermocouples came to equilibrium). The results were then transferred to Microsoft Excel for further analysis. First, recorded data was calibrated to correct the minute temperature off-set between the thermocouples (typically 0.1-0.2°C difference between the initial temperatures shown by different thermocouples).

The experiment was conducted once on the as-cast samples and was repeated one year later on the same samples.

3.5 Microstructure Determination

In order to determine the microstructure, the samples were first ground with 600 and 800 grid sandpaper. The polishing started with 6 micron and 1 micron alumina powder in oil, and then with 0.05 micron colloidal silica. The microstructure of each polished sample was then observed under optical microscope.

CHAPTER 4
RESULTS AND DISCUSSION

In this section, the results of the experiments are presented in seven separate categories. As it was seen in the phase diagram in Figure 1.7, the main intermetallic compounds formed in the SAC solder alloys at the present composition are Cu_6Sn_5 and Ag_3Sn. Section 4.1 shows the differential scanning calorimetry (DSC) results for the three alloys. In Section 4.2 the thermal diffusivity results for the two intermetallic compounds are presented. Sections 4.3 and 4.4 show the results of the thermal diffusivity values of the as-cast and processed samples, respectively. Section 4.5 demonstrates the temperature dependence of thermal diffusivity in the alloys. Section 4.6 discusses the difference in the derived values of κ between different measurement pairs in each sample, and finally Section 4.7 shows the microstructure of the solder alloys to explain the results presented in the previous sections.

4.1 Differential Scanning Calorimetry

Differential scanning calorimetry determines the amount of heat necessary to increase the temperature of a substance, versus temperature. This shows the possible phase changes at different temperatures in the material. The results of the DSC experiment performed on SAC305, SAC405, and SAC387 are shown in Figures 4.1, 4.2 and 4.3, respectively. The melting points observed are 218°C, 220°C and 219°C for the

alloys which is slightly higher than the published values. The slightly higher melting point observed in DSC results could be due to the machine not being calibrated.

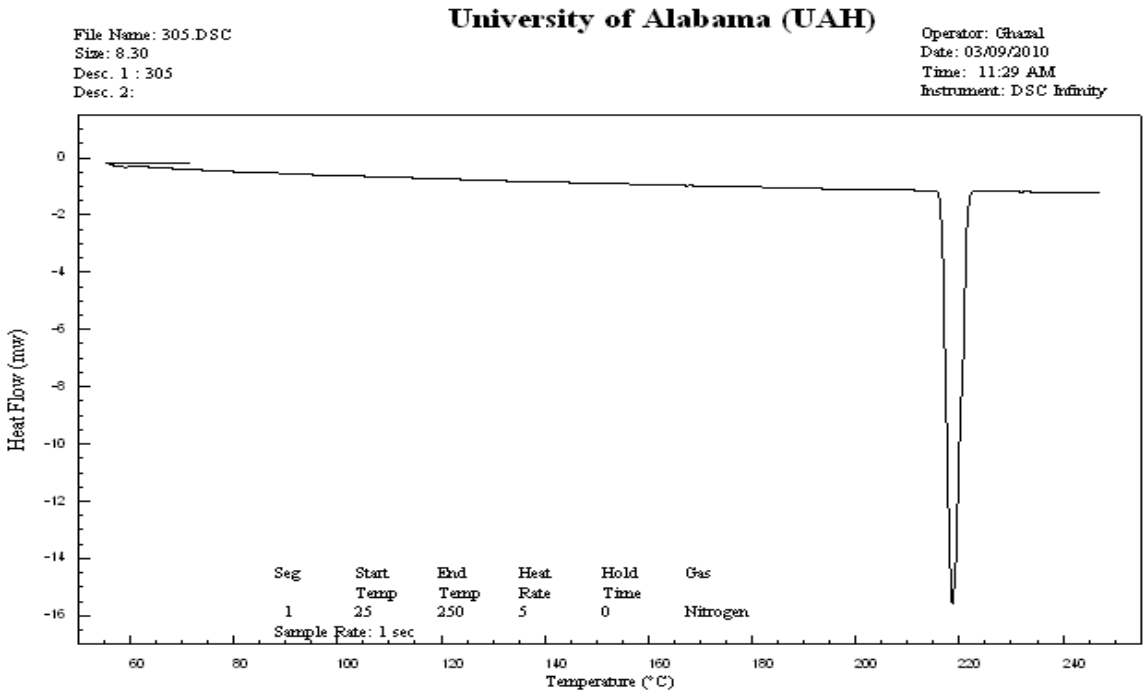

Figure 4.1 DSC results for SAC305

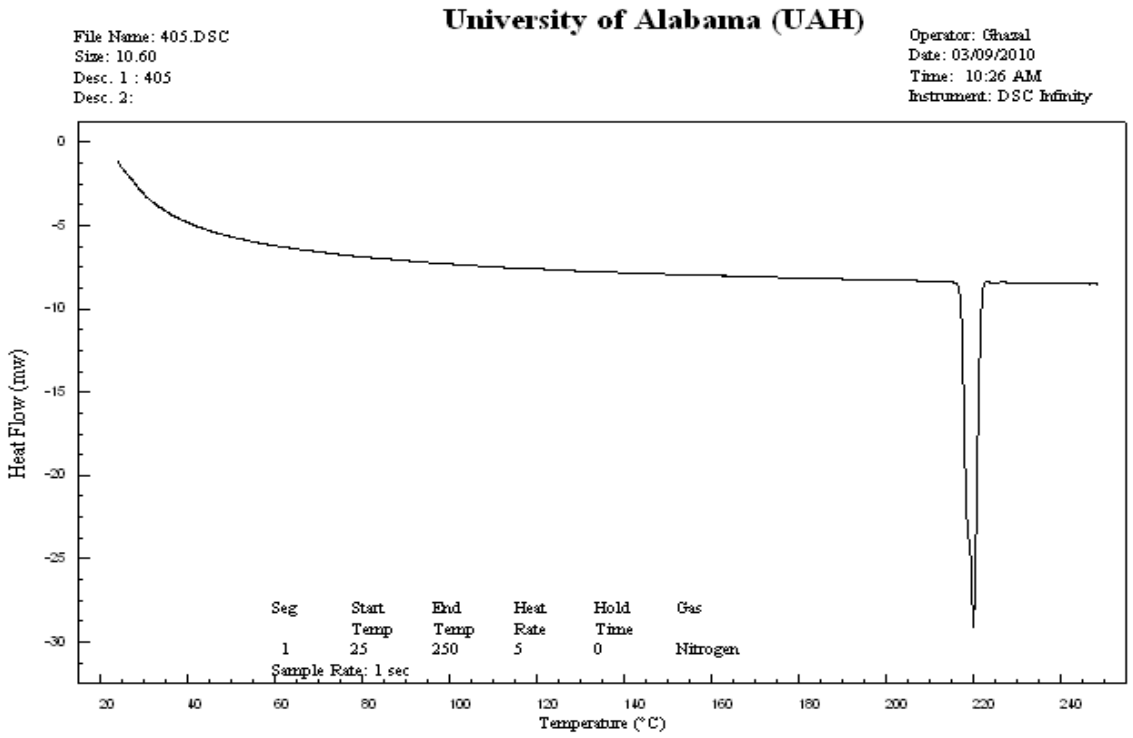

Figure 4.2 DSC results for SAC405

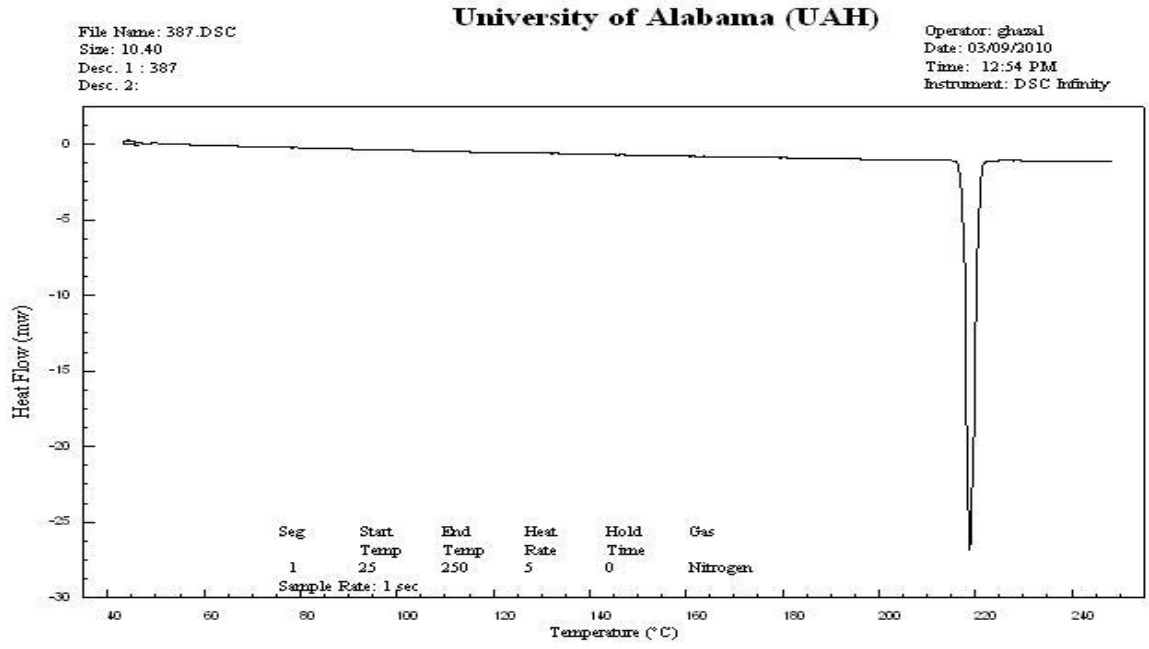

Figure 4.3 DSC results for SAC387

It can be seen in all three cases that the only phase change observed for the alloys from room temperature to 250°C is melting and no other major phase changes are observed. The melting points of the three alloys determined in DSC confirm the published values (Table 1.1).

4.2 Intermetallic Compounds

4.2.a Cu_6Sn_5 Binary Alloy

The ideal form of the temperature versus time profile was presented in Figure 2.1. Figure 4.4 shows the actual profile for Cu_6Sn_5 intermetallic compound at room temperature. It can be seen that the temperature starts at 20.2°C, then the heat pulse is applied and the outer measurement points (*T31* and *T32*) show a temperature rise of about 5°C, and then the middle measurement points (*T22* and *T21*) heat up, and the heat reaches *T11*, *T12* and *T0*.

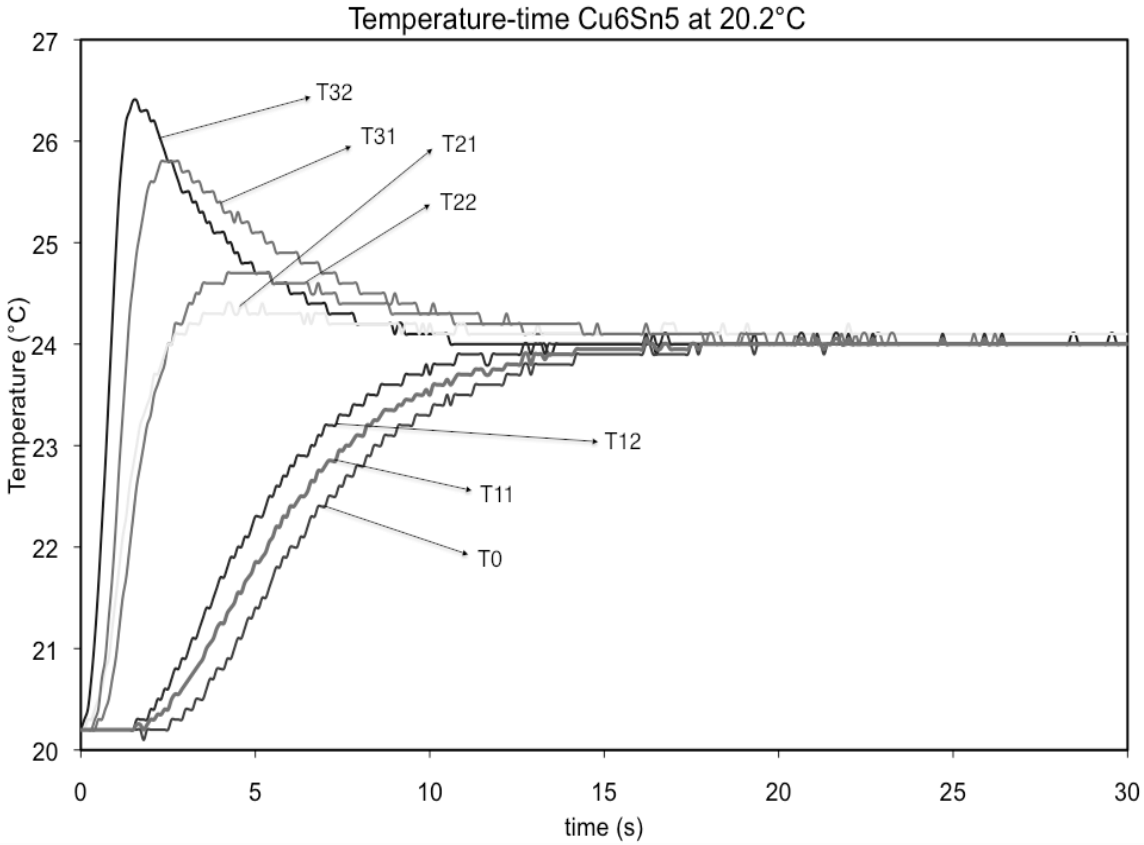

Figure 4.4 Temperature versus time values for Cu_6Sn_5 at 20.2°C

At around 18sec all thermocouples come to equilibrium of 24°C.

In the next step, the natural logarithm of the temperature difference between different pairs is calculated, and the results are shown as parallel lines in Figure 4.5. It can be seen that there are multiple horizontal points in each data set. The reason for this behavior is the rather low resolution of the thermocouples (only 0.1°C) which leads to several equal values of Δln_{ij}, forming the horizontal lines. This is not a source of concern since the differences are cancelled out and the overall slopes of the lines are not affected. The slope of these lines was used in equation (2.14) to determine the thermal diffusivity.

The thermal diffusivity determined from these slopes is 0.1907cm^2/sec. The derived values at higher temperatures are presented in Section 4.4.

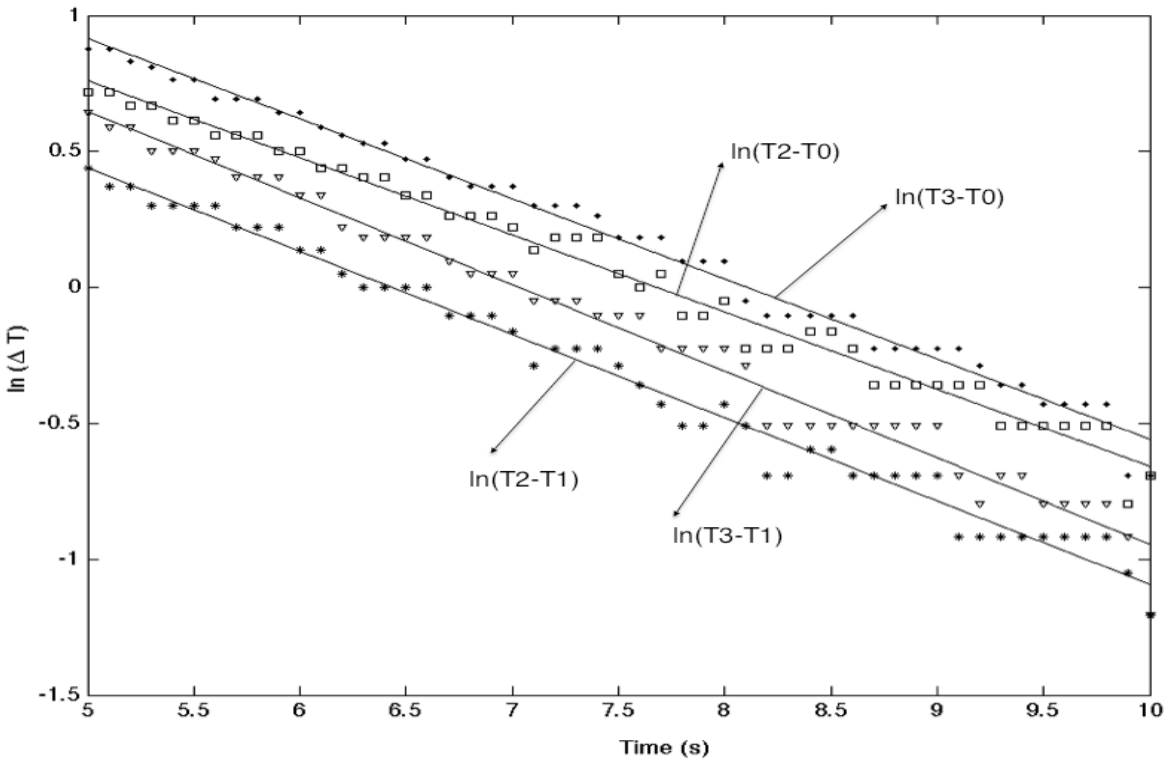

Figure 4.5 The $ln\Delta Tij$ versus time values for Cu_6Sn_5. The slope of these lines determines the thermal diffusivity.

4.2.b Ag_3Sn Binary Alloy

The second intermetallic compound present in the structure is Ag_3Sn. The temperatures versus time results for this compound at room temperature are presented in Figure 4.6. It can be seen again that the temperature starts at 24.8°C, and after the heat pulse is applied, the outer measurement points (*T31* and *T32*) show a temperature rise of

about 7°C, and then the middle measurement points (*T22* and *T21*) heat up, and the heat reaches *T11*, *T12* and *T0*. At around 20 sec all thermocouples come to equilibrium of 27.6°C.

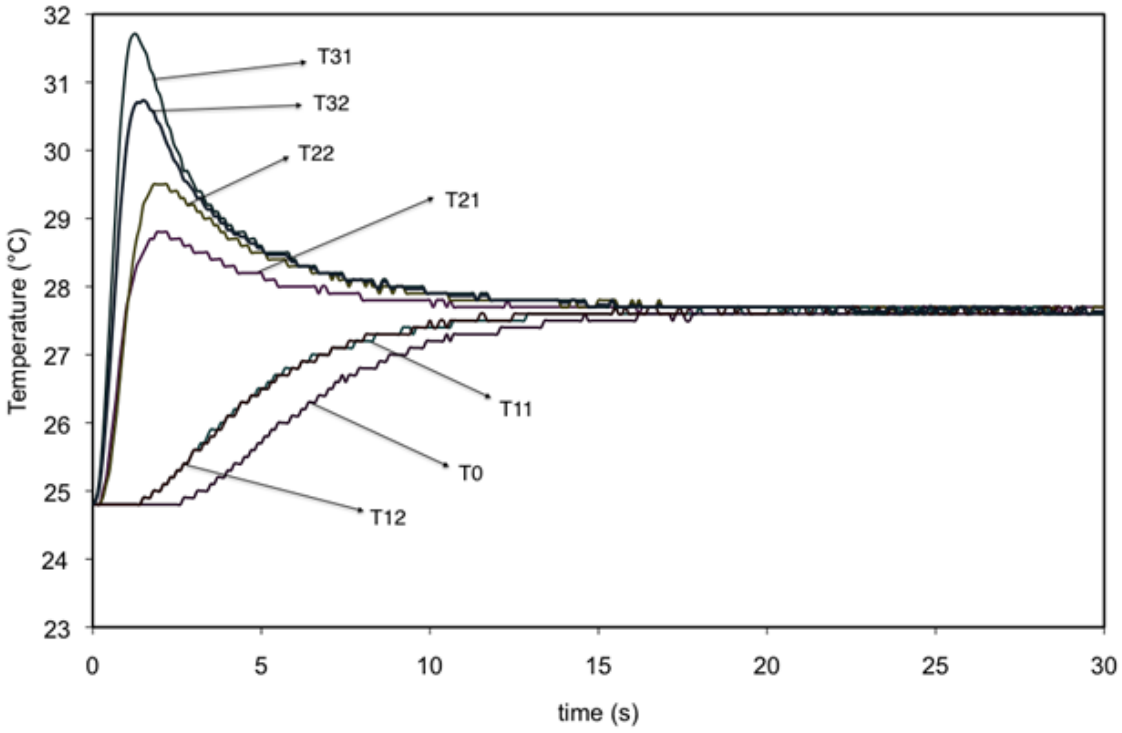

Figure 4.6 Temperature versus time values for Ag_3Sn at 24.8°C

After plotting the $ln\Delta T_{ij}$ versus time for this alloy, the results are shown in Figure 4.7. The value of the thermal diffusivity at this temperature is then derived as 0.17316 cm^2/sec. The values for higher temperatures are presented in Section 4.4.

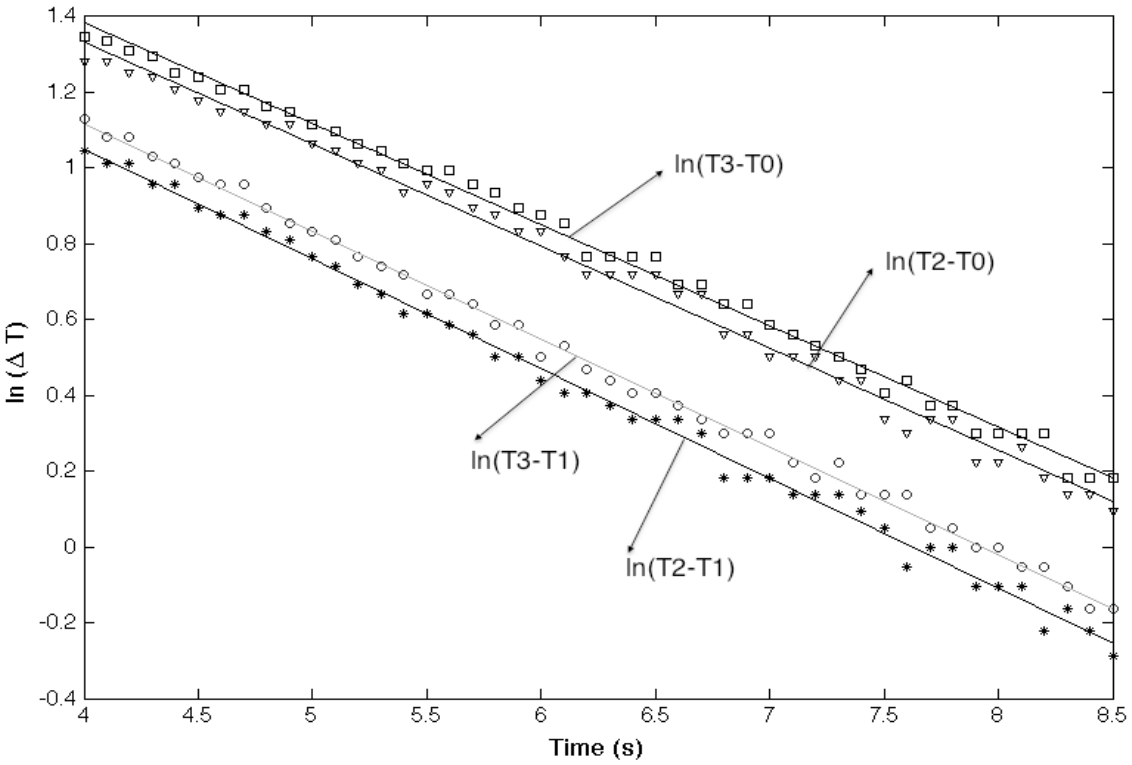

Figure 4.7 The lnΔTij versus time values for Ag_3Sn. The slope of these lines determines the thermal diffusivity.

4.3 SAC As-cast

The temperature versus time values for the three different alloys, hypoeutectic SAC305, hypereutectic SAC405 and eutectic SAC387, are presented in this section. These results correspond to the as-cast samples without any previous processing.

4.3.a SAC305

Figure 4.8 shows the natural logarithm of temperature difference versus time for different measurement pairs at 25.2°C. It can be seen that unlike previous work

(Brantschen and Pourpoint) and the results for the intermetallic compounds presented in Section 4.1, the resulting lines in this case are not parallel and show considerable difference in slopes. This difference reaches to as much as 300% from *T21-T0* to *T22-T0*. In order to investigate and confirm these results, the same experiment was repeated after a year from the first experiment, the results of which are shown in Section 4.3.

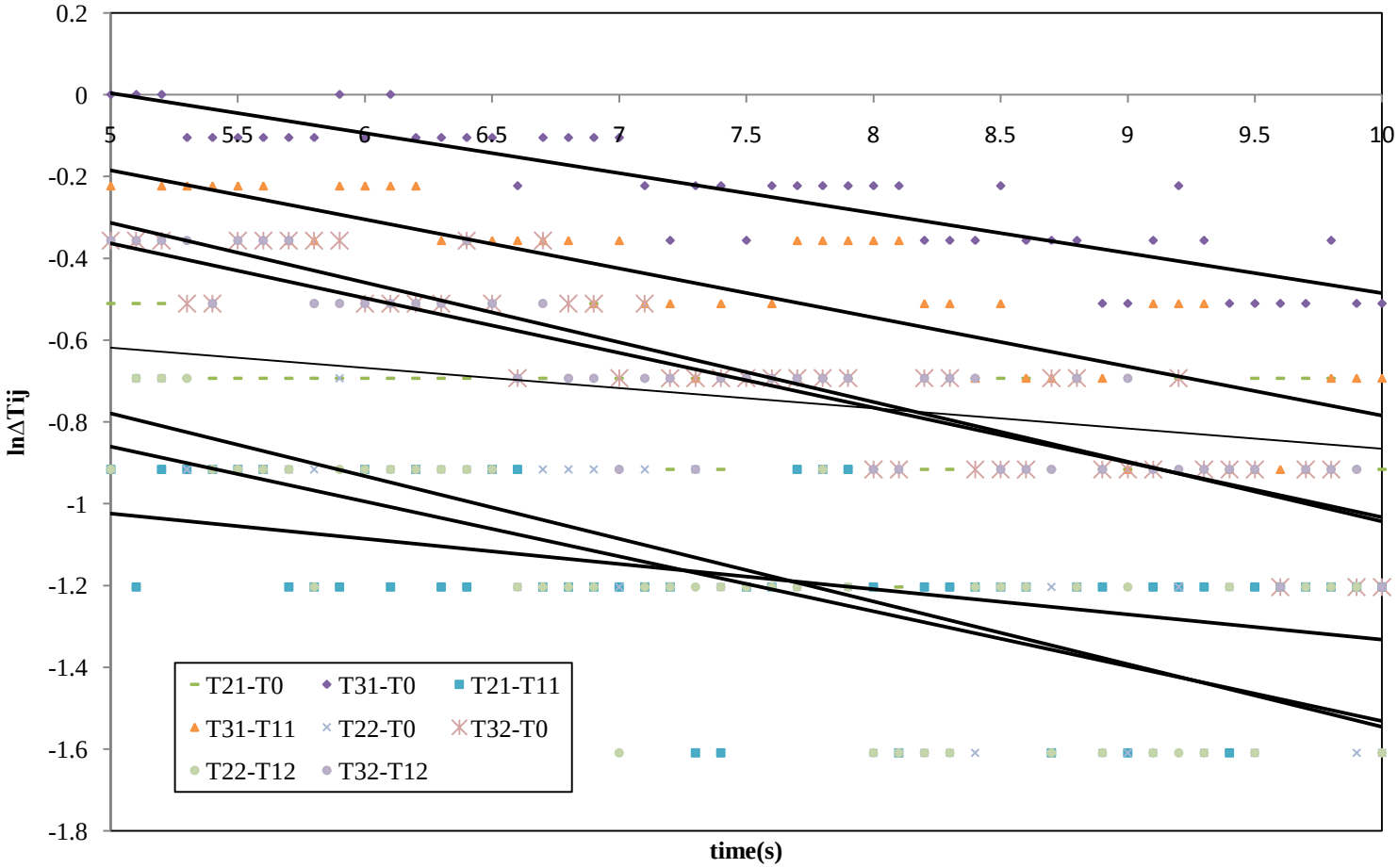

Figure 4.8 $ln\Delta T_{ij}$ versus time values for as-received SAC305 at 25.2°C

4.3.b SAC405 As-received

Figure 4.9 shows the natural logarithm of temperature difference versus time for different measurement pairs at 25.9°C. It can be seen that in this case also, the lines are not parallel and this difference reaches to as much as 285% from *T31-T0* to *T32-T0* pairs. This experiment was also repeated a year after the first set, to see if the same results would be reproduced.

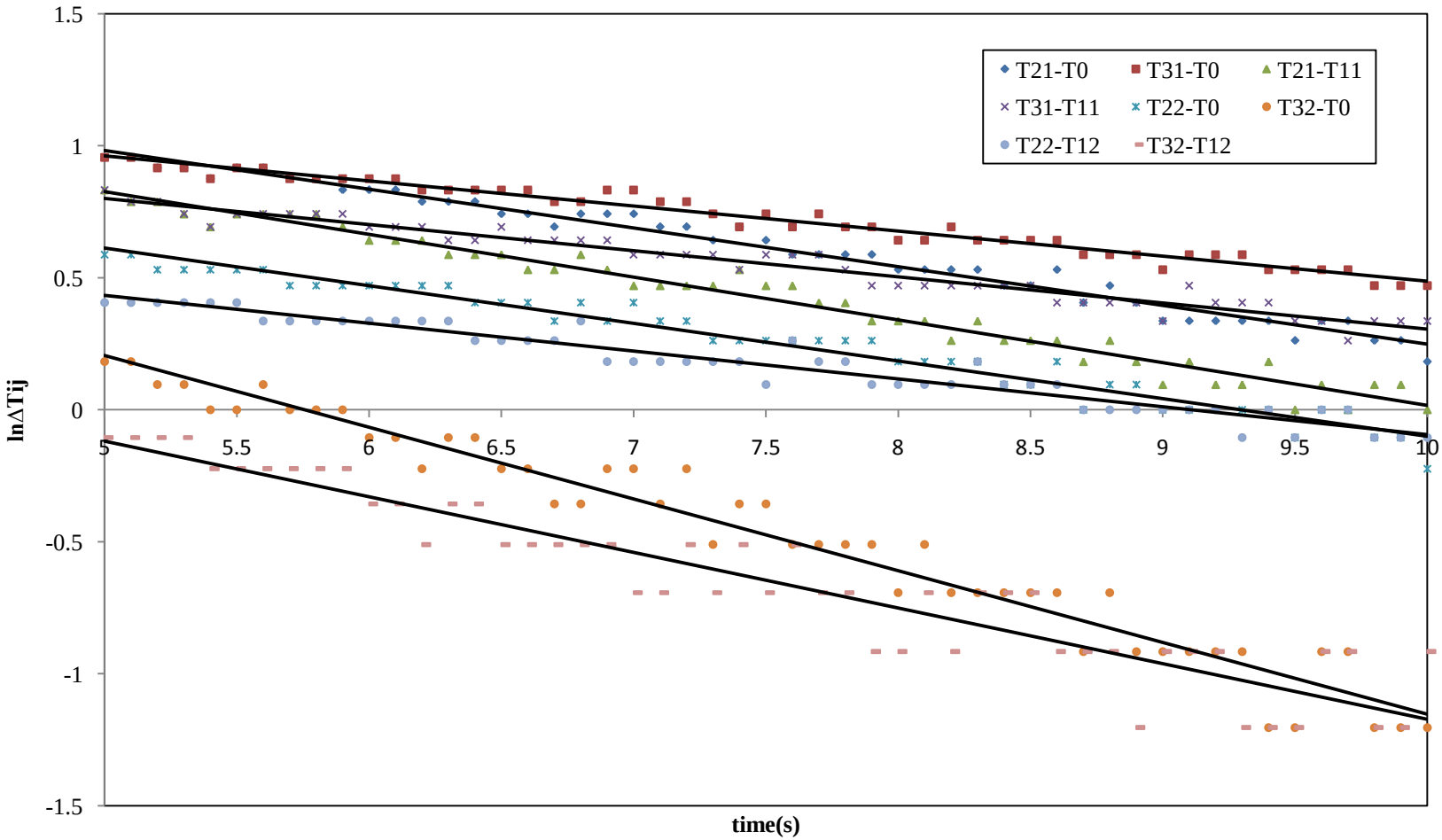

Figure 4.9 *lnΔTij* versus time values for as-received SAC405 at 25.2°C

4.3.c As-received SAC387

Figure 4.10 shows the results for the eutectic compound SAC387. It can be seen that the slopes are still not as close as they were in the intermetallic compounds, but considerably closer that in SAC305 and SAC405. This suggests that the more uniform structure in the eutectic compound could have let to more uniform behavior. This will be discussed in further detail at the end of this chapter.

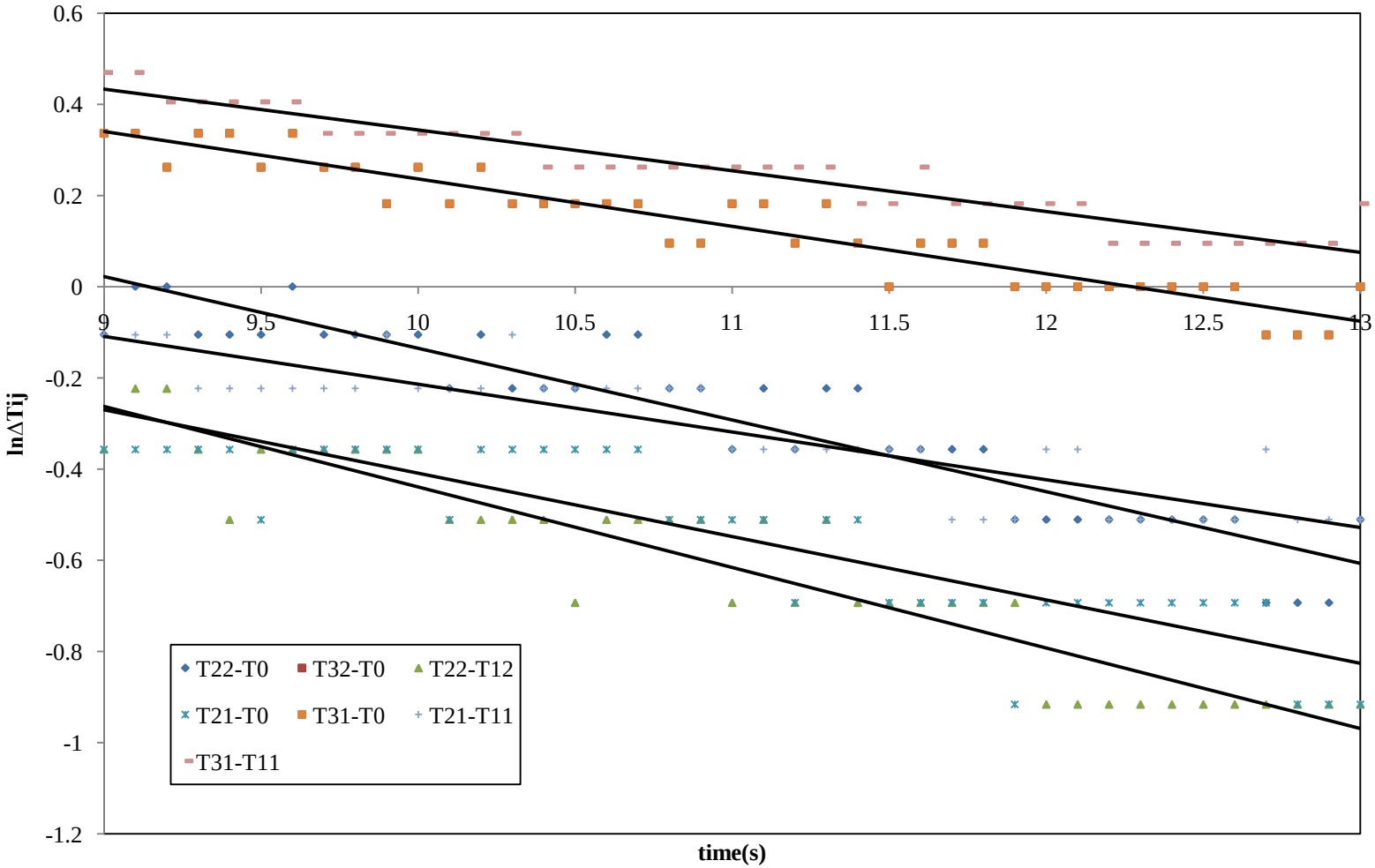

Figure 4.10 *lnΔTij* versus time values for SAC387 at 25.1°C

4.4 SAC Processed

Considering the fact that the slopes of the natural logarithm of the temperature difference between different measurement pairs in SAC305 and SAC405 had drastic differences, hence resulting in different thermal diffusivities, the test on these two alloys were repeated under the same conditions after about a year passed from the first set of tests. It should be noted that these samples were no longer in "as-received" condition and had gone under different thermal processes (being heated to up to 120°C and kept for a sum of about 48 hours, and being affected by the heat pulse for 2 seconds each time the test was performed at each temperature, and staying in room temperature for a year after the first set of tests).

The room temperature results of the new tests on the "processed" samples are presented below. The results at higher temperatures are presented in Section 4.5.

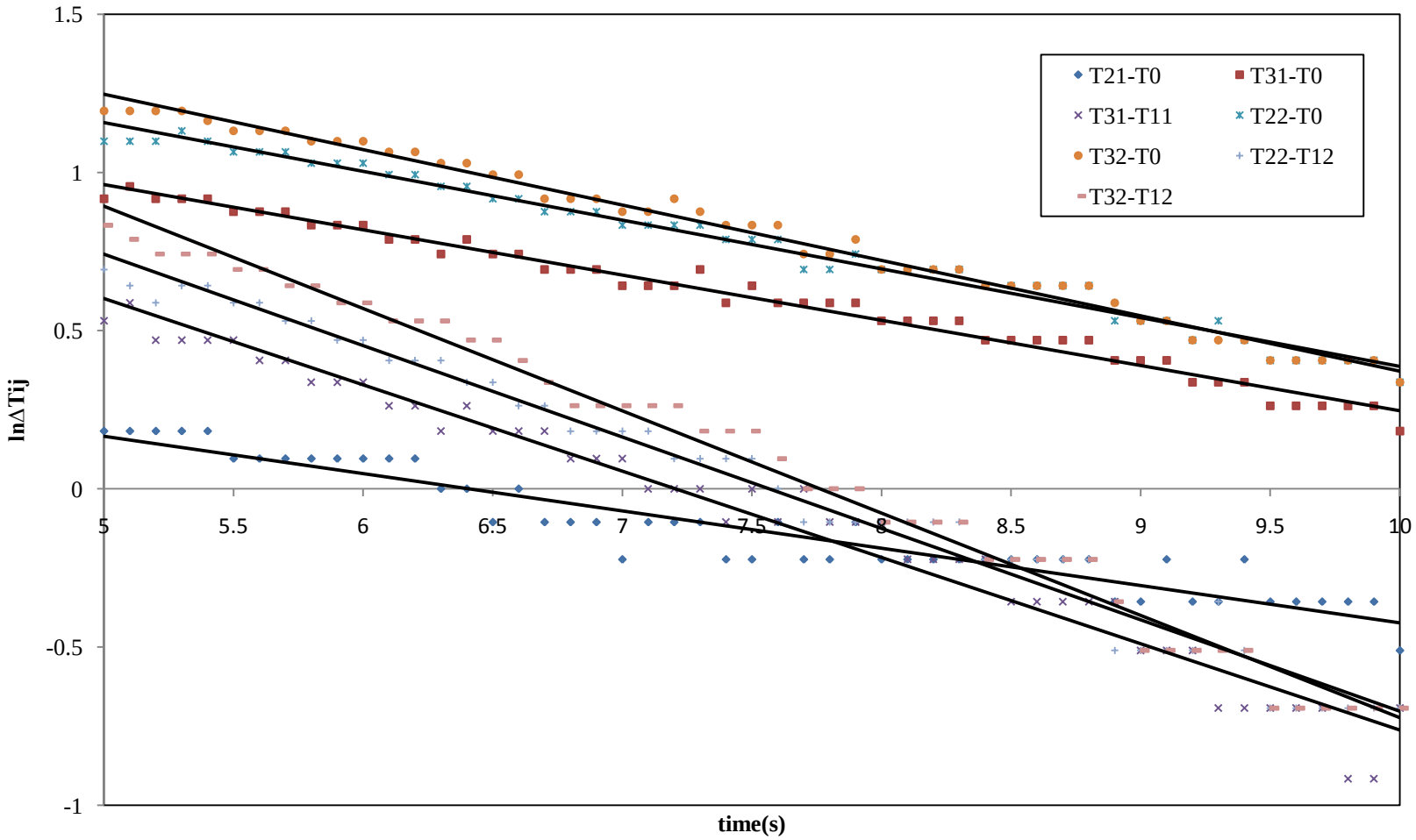

Figure 4.11 *lnΔTij* versus time values for processed SAC305 at 24.2°C

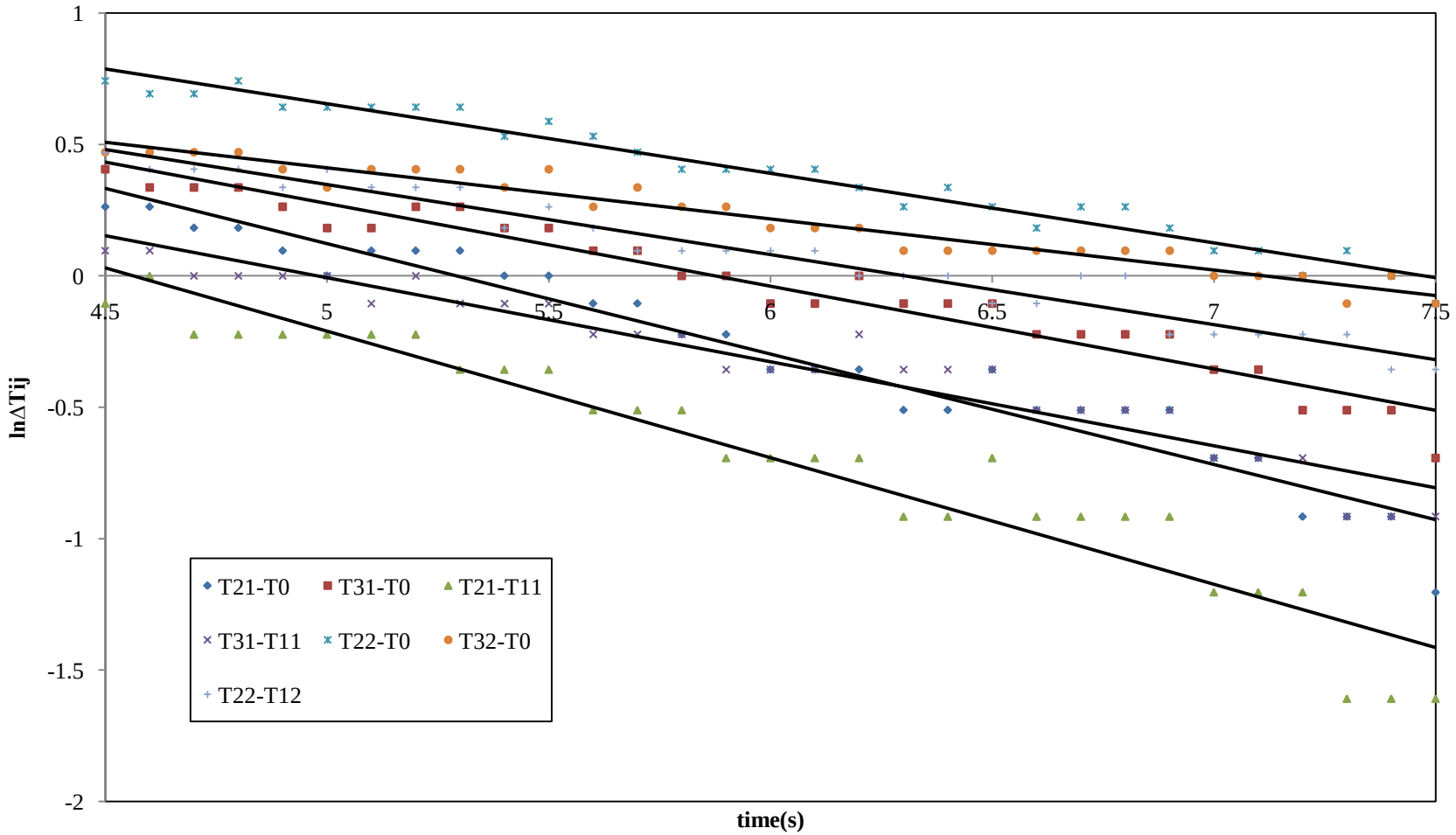

Figure 4.12 *lnΔTij* versus time values for processed SAC405 at 30.7°C

It can be seen that in both cases of SAC305 and SAC405, repeating the test led to results that still have strong differences in the slope between different measurement pairs. This suggests that the difference could be due to the non-uniform distribution of the phases inside the sample, leading different sections of the sample to show different thermal diffusivities. The microstructure of the samples is presented in Section 4.7.

The results for higher temperatures and comparison of the as-received versus the processed samples are presented in Section 4.5.

4.5 κ vs. T

This section presents the thermal diffusivity versus temperature for intermetallic compounds and as-received and processed SAC alloys from room temperature to up to 120°C. The thermal diffusivity versus time curve for pure Sn is shown in Figure 4.13 for comparison.

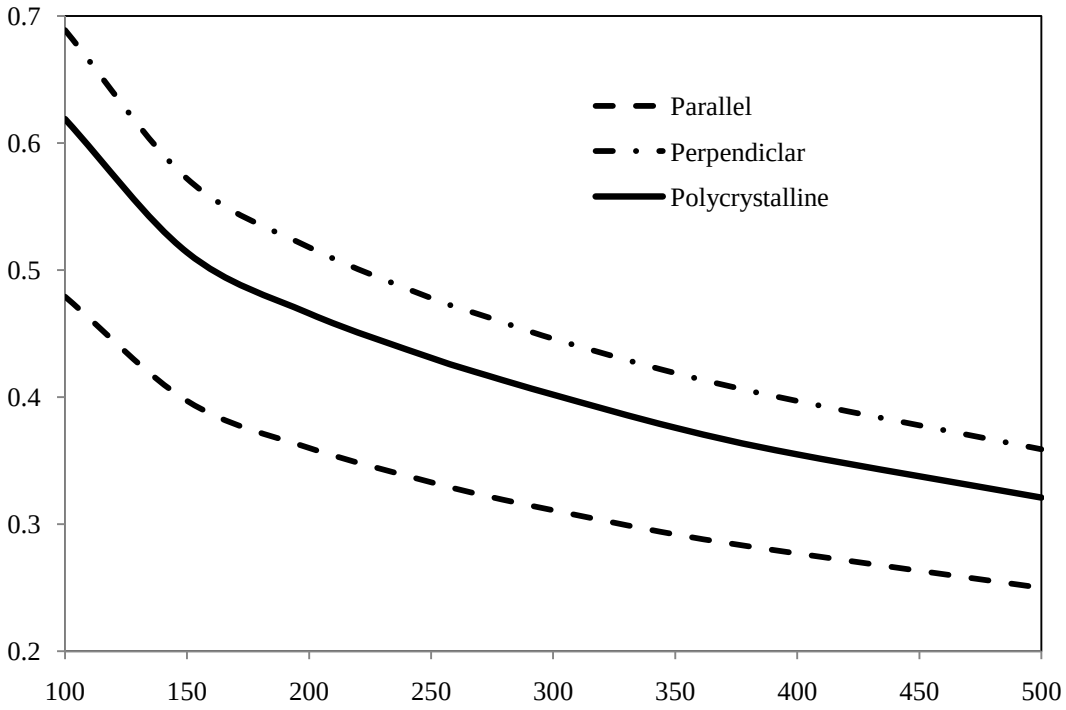

Figure 4.13 The thermal diffusivity of pure Tin with respect to temperature [39]

4.5.a Intermetallic Compounds

Figures 4.14 and 4.15 show the values of thermal diffusivity versus temperature for the intermetallic compounds of Cu_6Sn_5 and Ag_3Sn, respectively.

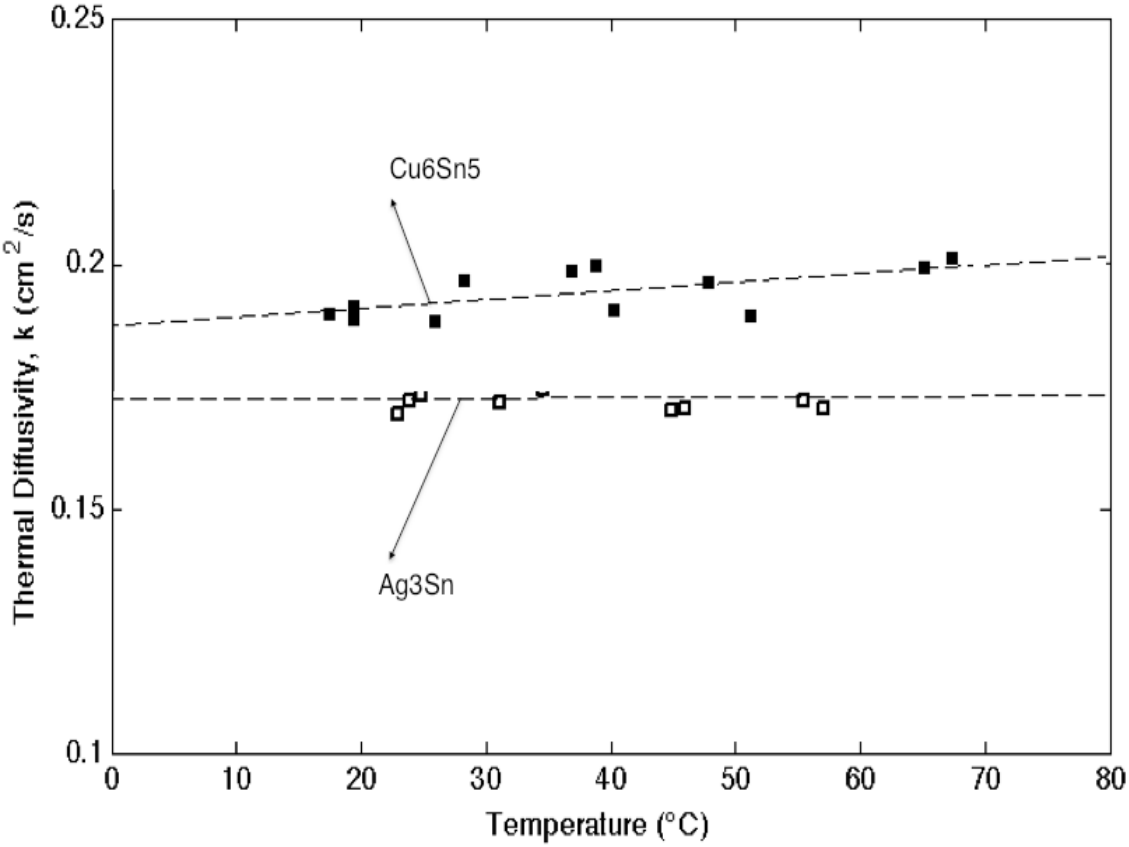

Figure 4.14 The thermal diffusivity versus temperature for Cu_6Sn_5 and Ag_3Sn

It can be seen from Figure 4.14 that the thermal diffusivity in Cu_6Sn_5 alloy shows a slight increase with temperature from room temperature to 80°C; whereas the thermal diffusivity in Ag_3Sn does not show any significant change with respect to temperature. The numerical values of κ versus T are shown in Tables 4.1 and 4.2.

Table 4.1 Thermal diffusivity values for Cu_6Sn_5 from room temperature to 78.1°C

T(°C)	**k(cm2/s)**
20.2	0.1907
22.4	0.1919
22.5	0.1896
30	0.1892
32.7	0.1972
42.7	0.1990
45	0.2001
46.6	0.1913
55.4	0.1966
59.4	0.1903
75.6	0.1996
78.1	0.2016

Table 4.2 Thermal diffusivity values for Ag_3Sn from room temperature to 70.4°C

T(°C)	k(cm^2/s)
23	0.1694
23.9	0.1720
24.8	0.1732
31.1	0.1717
33.9	0.1769
34.6	0.1744
43.9	0.1762
44.9	0.1701
46	0.1705
55.5	0.1721
56	0.1756
57.1	0.1705
68.8	0.1737
70.4	0.1725

4.5.b SAC305

Since the slopes of different $ln\Delta Tij$ versus time differed significantly between different measurement points in this sample, the thermal diffusivity was determined separately for each pair at each measurement temperature. The results of κ vs. T for the as-received and processed SAC305 alloy are shown in Figures 4.15 and 4.16, respectively. The numeric values of the results are shown in Tables 4.3 and 4.4.

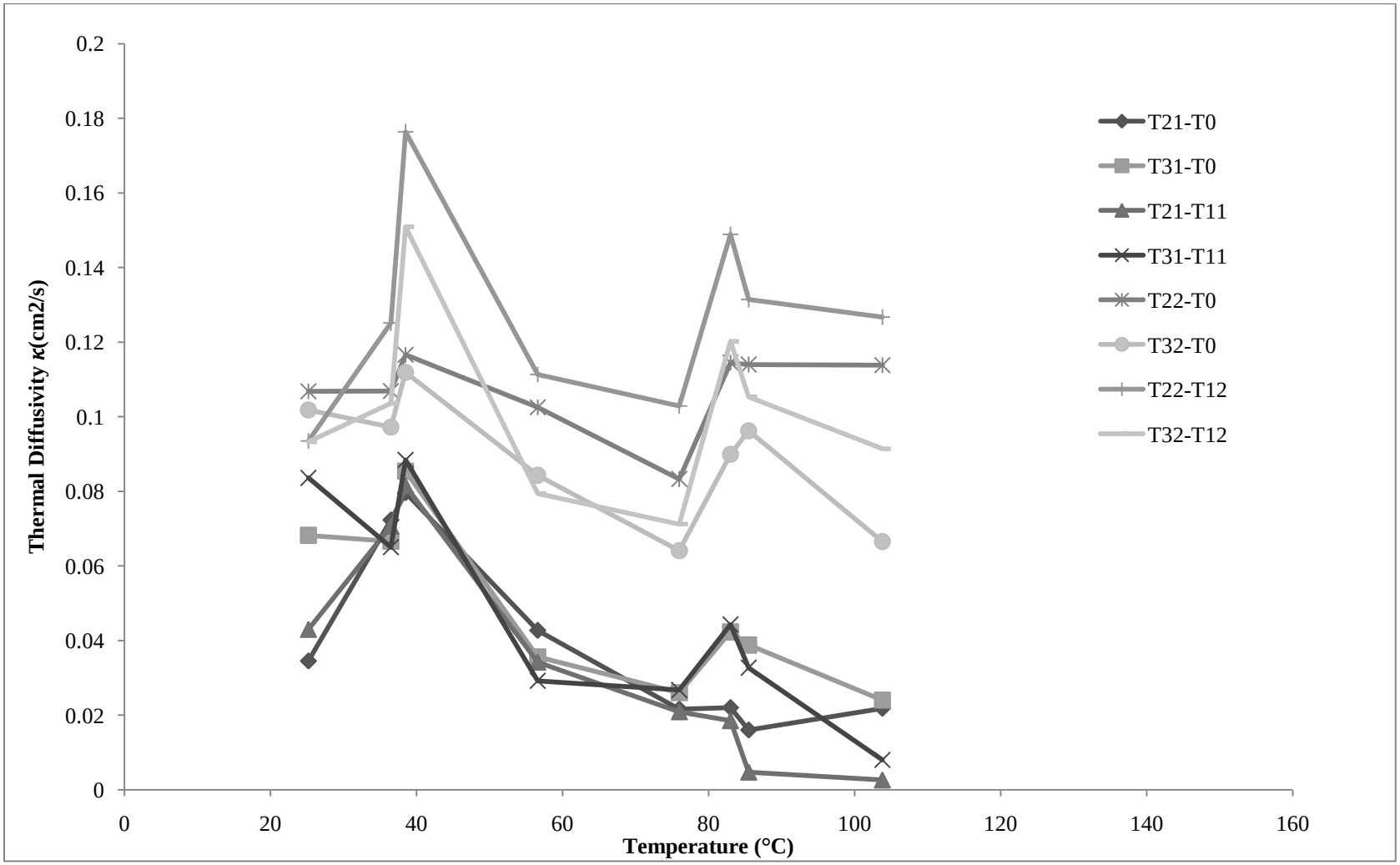

Figure 4.15 Thermal diffusivity versus Temperature in as-received SAC305

Table 4.3 Thermal diffusivity values for as-received SAC305 for different measurement pairs

T(°C)	**k(cm^2/sec)**							
	T_{21}-T_0	**T_{31}-T_0**	**T_{21}-T_{11}**	**T_{31}-T_{11}**	**T_{22}-T_0**	**T_{32}-T_0**	**T_{22}-T_{12}**	**T_{32}-T_{12}**
25.2	0.0345	0.0682	0.0430	0.0836	0.1068	0.1018	0.0935	0.0933
36.5	0.0723	0.0666	0.0707	0.0650	0.1069	0.0972	0.1251	0.1036
38.5	0.0796	0.0854	0.0815	0.0884	0.1166	0.1119	0.1764	0.1509
56.6	0.0427	0.0356	0.0342	0.0292	0.1025	0.0843	0.1113	0.0794
76	0.0216	0.0260	0.0209	0.0267	0.0833	0.0641	0.1029	0.0712
83	0.0220	0.0423	0.0185	0.0443	0.1145	0.0899	0.1489	0.1202
85.5	0.0160	0.0388	0.0047	0.0327	0.1140	0.0962	0.1314	0.1053
103.8	0.0218	0.0240	0.0026	0.0080	0.1138	0.0665	0.1267	0.0914

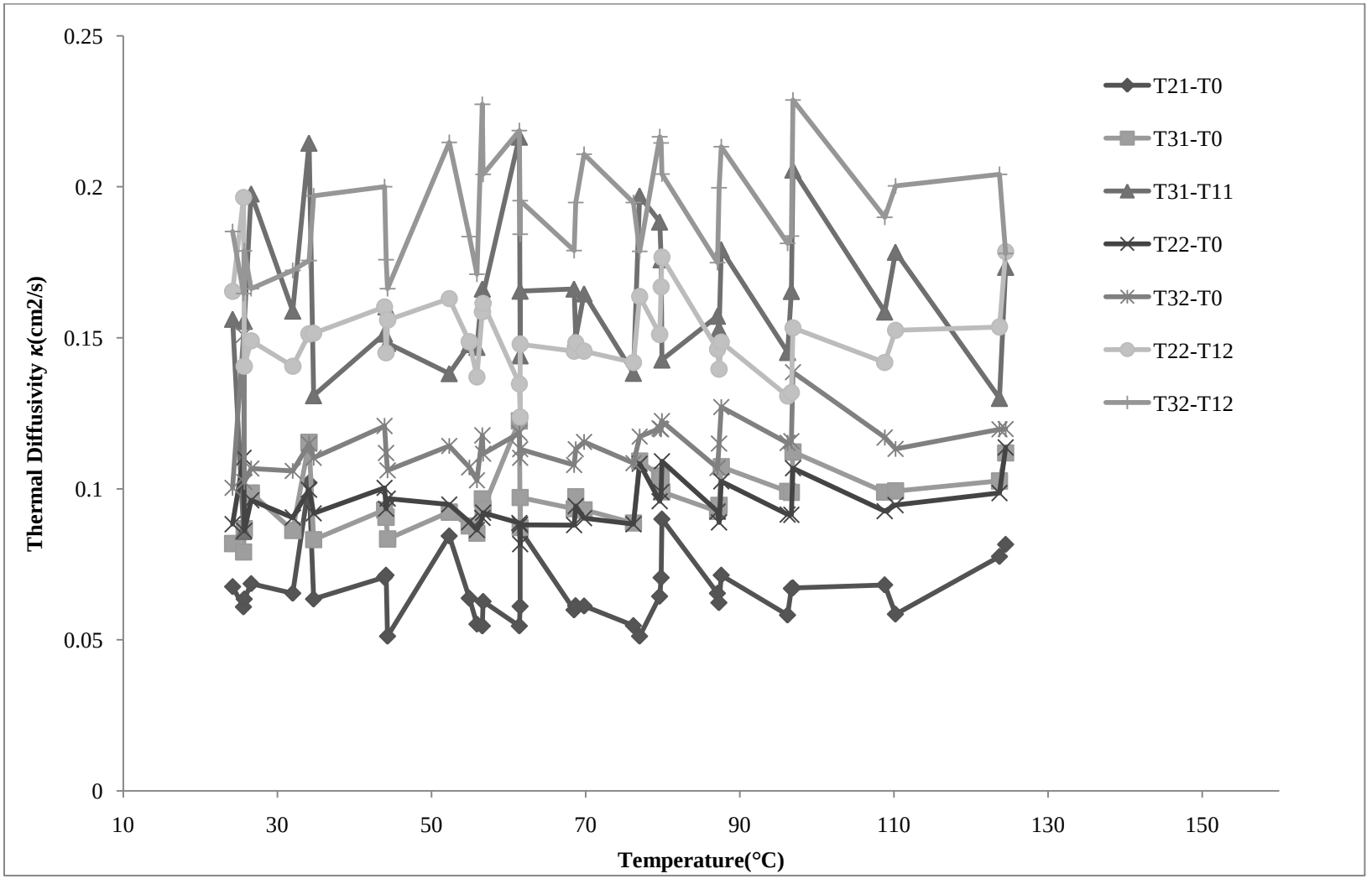

Figure 4.16 Thermal diffusivity versus Temperature in processed SAC305

It can be seen in both Figures 4.15 and 4.16 that thermal diffusivity versus temperature shows a similar behavior with respect to temperature for all measurement points, but as mentioned in Section 4.1, the values are significantly different.

Table 4.4 Thermal diffusivity values for processed SAC305 for different measurement pairs

T	k (cm^2/s)						
	T_{21}-T_0	T_{31}-T_0	T_{31}-T_{11}	T_{22}-T_0	T_{32}-T_0	T_{22}-T_{12}	T_{32}-T_{12}
24.2	0.0676	0.0819	0.1562	0.0883	0.1003	0.1654	0.1852
25.6	0.0609	0.0791	0.0859	0.1103	0.1509	0.1965	0.1647
25.7	0.0635	0.0868	0.1555	0.0861	0.1023	0.1406	0.1788
26.6	0.0686	0.0986	0.1977	0.0962	0.1067	0.1490	0.1663
32.0	0.0654	0.0862	0.1589	0.0905	0.1059	0.1406	0.1723
34.1	0.1020	0.1154	0.2145	0.0997	0.1149	0.1513	0.1756
34.7	0.0635	0.0832	0.1309	0.0919	0.1103	0.1515	0.1970
43.9	0.0707	0.0930	0.1513	0.1003	0.1208	0.1602	0.2000
44.1	0.0714	0.0906	0.1603	0.0934	0.1119	0.1450	0.1759
44.3	0.0512	0.0834	0.1482	0.0968	0.1061	0.1559	0.1663
52.3	0.0844	0.0923	0.1382	0.0948	0.1142	0.1630	0.2147
54.9	0.0638	0.0877	0.1478	0.0890	0.1071	0.1487	0.1835
55.9	0.0552	0.0853	0.1469	0.0864	0.1028	0.1370	0.1711
56.6	0.0546	0.0967	0.1662	0.0904	0.1177	0.1586	0.2273
56.7	0.0627	0.0934	0.1643	0.0921	0.1116	0.1614	0.2041
61.4	0.0546	0.1225	0.2165	0.0887	0.1185	0.1347	0.2186
61.5	0.0611	0.0872	0.1441	0.0817	0.1103	0.1238	0.1843
61.5	0.0864	0.0971	0.1655	0.0881	0.1131	0.1479	0.1954
68.5	0.0599	0.0934	0.1662	0.0880	0.1079	0.1456	0.1789
68.7	0.0613	0.0974	0.1500	0.0943	0.1131	0.1484	0.1948
69.8	0.0612	0.0930	0.1646	0.0903	0.1155	0.1456	0.2108
76.2	0.0547	0.0887	0.1383	0.0883	0.1085	0.1418	0.1948
77.0	0.0512	0.1092	0.1970	0.1083	0.1173	0.1637	0.1786
79.6	0.0644	0.1044	0.1884	0.0959	0.1200	0.1511	0.2166
79.8	0.0706	0.1033	0.1759	0.0989	0.1197	0.1669	0.2145
79.9	0.0900	0.0990	0.1427	0.1091	0.1224	0.1767	0.2042
87.1	0.0654	0.0925	0.1572	0.0925	0.1069	0.1462	0.1749
87.3	0.0623	0.0945	0.1529	0.0889	0.1150	0.1396	0.1997
87.6	0.0714	0.1073	0.1792	0.1025	0.1271	0.1486	0.2133
96.2	0.0582	0.0992	0.1452	0.0915	0.1152	0.1307	0.1813
96.7	0.0670	0.0988	0.1654	0.0914	0.1158	0.1319	0.1837
96.9	0.0672	0.1122	0.2056	0.1068	0.1386	0.1533	0.2287
108.8	0.0682	0.0989	0.1586	0.0926	0.1170	0.1418	0.1899
110.2	0.0585	0.0993	0.1784	0.0946	0.1132	0.1525	0.2003
123.7	0.0776	0.1026	0.1300	0.0986	0.1197	0.1536	0.2041
124.5	0.0816	0.1119	0.1734	0.1137	0.1198	0.1785	0.1779

4.5.c SAC405

Figures 4.17 and 4.18 show the thermal diffusivity versus temperature behavior of as-received and processed SAC405 hypereutectic alloy, respectively. Also Tables 4.5 and 4.6 show the numerical values of κ.

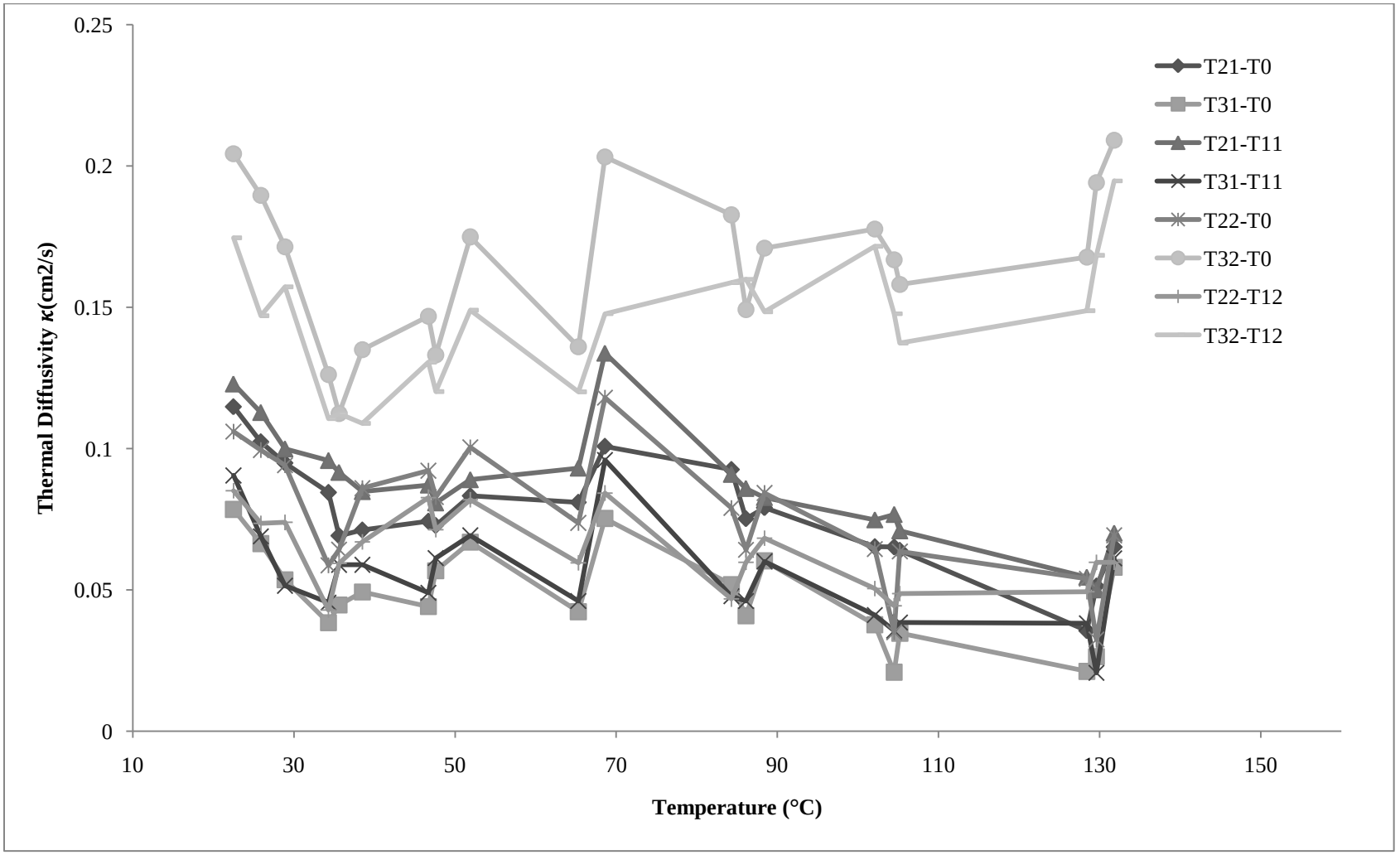

Figure 4.17 Thermal diffusivity versus Temperature in as-received SAC405

Table 4.5 Thermal diffusivity values for as-received SAC405 for different measurement pairs

T(°C)	k(cm^2/sec)							
	T_{21}-T_0	T_{31}-T_0	T_{21}-T_{11}	T_{31}-T_{11}	T_{22}-T_0	T_{32}-T_0	T_{22}-T_{12}	T_{32}-T_{12}
22.5	0.1148	0.0785	0.1229	0.0905	0.1060	0.2043	0.0851	0.1746
25.9	0.1024	0.0664	0.1128	0.0690	0.0995	0.1896	0.0736	0.1470
28.9	0.0949	0.0536	0.0999	0.0515	0.0941	0.1714	0.0739	0.1572
34.3	0.0845	0.0384	0.0958	0.0455	0.0587	0.1262	0.0429	0.1106
35.6	0.0692	0.0447	0.0916	0.0589	0.0643	0.1124	0.0594	0.1124
38.5	0.0712	0.0493	0.0848	0.0589	0.0860	0.1350	0.0670	0.1089
46.7	0.0743	0.0441	0.0871	0.0490	0.0922	0.1468	0.0827	0.1306
47.6	0.0728	0.0568	0.0808	0.0613	0.0829	0.1331	0.0713	0.1202
51.9	0.0833	0.0669	0.0890	0.0693	0.1005	0.1749	0.0819	0.1490
65.3	0.0810	0.0423	0.0931	0.0461	0.0737	0.1360	0.0596	0.1201
68.6	0.1008	0.0753	0.1338	0.0960	0.1180	0.2032	0.0843	0.1477
84.3	0.0926	0.0519	0.0909	0.0478	0.0790	0.1827	0.0468	0.1587
86.1	0.0752	0.0409	0.0859	0.0461	0.0642	0.1492	0.0598	0.1599
88.4	0.0791	0.0603	0.0827	0.0601	0.0843	0.1709	0.0683	0.1484
102.1	0.0653	0.0377	0.0748	0.0411	0.0645	0.1777	0.0505	0.1716
104.5	0.0652	0.0209	0.0767	0.0356	0.0350	0.1668	0.0444	0.1477
105.2	0.0640	0.0347	0.0709	0.0385	0.0636	0.1581	0.0487	0.1373
128.4	0.0356	0.0212	0.0545	0.0382	0.0540	0.1677	0.0494	0.1488
129.6	0.0514	0.0264	0.0500	0.0207	0.0325	0.1941	0.0598	0.1684
131.8	0.0652	0.0580	0.0701	0.0612	0.0693	0.2091	0.0598	0.1947

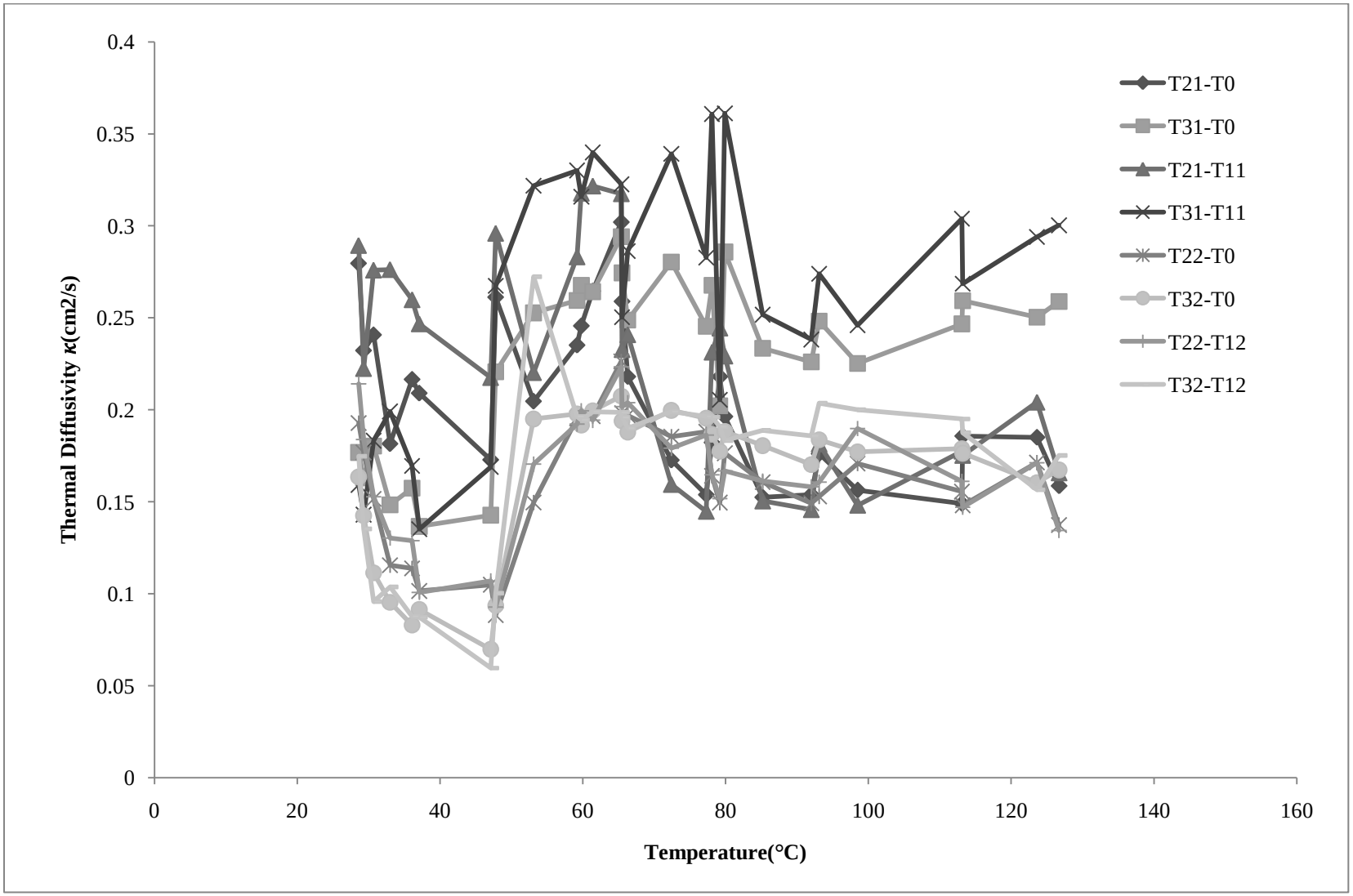

Figure 4.18 Thermal diffusivity versus Temperature in processed SAC405

Table 4.6 Thermal diffusivity values for processed SAC405 for different measurement pairs

T(°C)	k(cm^2/sec)							
	T_{21}-T_0	T_{31}-T_0	T_{21}-T_{11}	T_{31}-T_{11}	T_{22}-T_0	T_{32}-T_0	T_{22}-T_{12}	T_{32}-T_{12}
28.6	0.2796	0.1768	0.2893	0.1592	0.1928	0.1635	0.2141	0.1747
29.3	0.2322	0.1630	0.2224	0.1430	0.1768	0.1425	0.1839	0.1352
30.7	0.2407	0.1803	0.2759	0.1832	0.1516	0.1114	0.1527	0.0957
33	0.1815	0.1483	0.2762	0.1991	0.1155	0.0953	0.1303	0.1037
36.1	0.2165	0.1574	0.2598	0.1695	0.1138	0.0830	0.1288	0.0876
37.1	0.2090	0.1366	0.2467	0.1351	0.1015	0.0914	0.1007	0.0872
47.1	0.1728	0.1427	0.2175	0.1689	0.1049	0.0698	0.1069	0.0596
47.8	0.2612	0.2206	0.2959	0.2674	0.0884	0.0936	0.0927	0.1003
53.1	0.2046	0.2527	0.2202	0.3218	0.1496	0.1950	0.1705	0.2724
59.2	0.2351	0.2594	0.2831	0.3301	0.1954	0.1977	0.1922	0.1963
59.8	0.2456	0.2676	0.3177	0.3158	0.1949	0.1917	0.1995	0.1945
61.4	0.2645	0.2642	0.3216	0.3399	0.1965	0.1995	0.1943	0.1989
65.4	0.3020	0.2941	0.3174	0.3226	0.2263	0.2074	0.2233	0.1986
65.5	0.2589	0.2744	0.2327	0.2503	0.1982	0.1939	0.2017	0.1959
66.3	0.2180	0.2488	0.2408	0.2863	0.1969	0.1878	0.2039	0.1899
72.4	0.1726	0.2803	0.1594	0.3391	0.1854	0.1997	0.1791	0.1990
77.3	0.1538	0.2454	0.1448	0.2827	0.1881	0.1954	0.1863	0.1964
78.1	0.1822	0.2677	0.2313	0.3608	0.1641	0.1867	0.1646	0.1961
79.2	0.2180	0.2022	0.2444	0.2054	0.1495	0.1774	0.1517	0.1908
79.9	0.1963	0.2858	0.2292	0.3612	0.1764	0.1882	0.1668	0.1833
85.2	0.1524	0.2334	0.1504	0.2517	0.1607	0.1805	0.1612	0.1888
92	0.1539	0.2260	0.1457	0.2382	0.1492	0.1702	0.1581	0.1858
93.1	0.1761	0.2482	0.1814	0.2739	0.1529	0.1837	0.1607	0.2036
98.5	0.1563	0.2252	0.1481	0.2460	0.1708	0.1771	0.1898	0.2000
113.1	0.1490	0.2467	0.1775	0.3039	0.1555	0.1788	0.1611	0.1950
113.2	0.1857	0.2593	0.1752	0.2685	0.1481	0.1764	0.1470	0.1875
123.6	0.1850	0.2503	0.2041	0.2940	0.1713	0.1604	0.1712	0.1565
126.7	0.1586	0.2589	0.1657	0.3003	0.1374	0.1673	0.1344	0.1752

4.5.d SAC387

Figure 4.19 and Table 4.7 show the thermal diffusivity versus temperature values for the eutectic composition, SAC387.

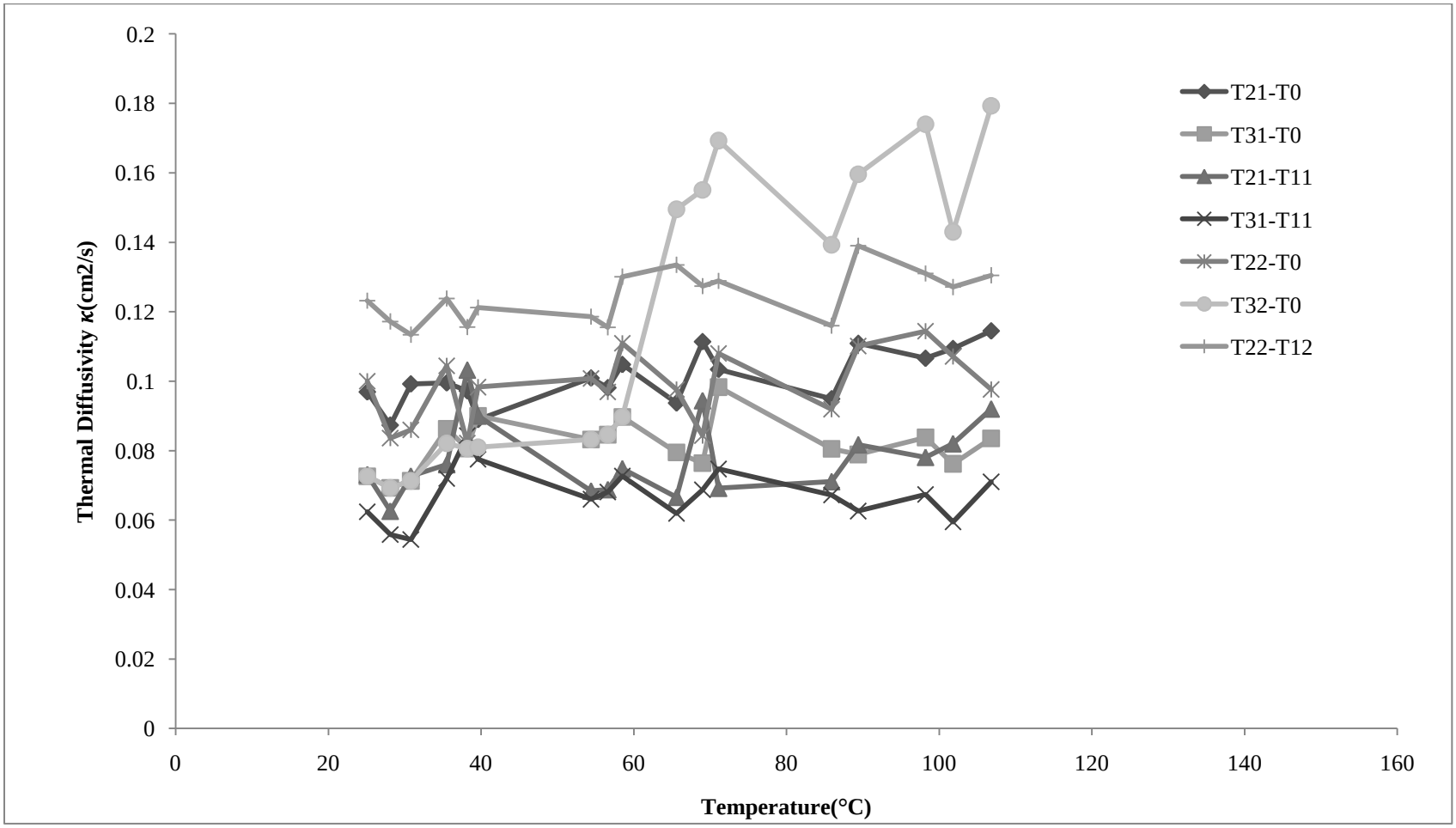

Figure 4.19 Thermal diffusivity versus Temperature in as-received SAC387

It can be seen in Figure 4.19 that the thermal diffusivity shows a steady value with respect to time in all measurement pair except for *T32-T0* in which the thermal diffusivity seems to be increasing with temperature.

Table 4.7 Thermal diffusivity values for as-received SAC387 for different measurement pairs.

T(°C)	**k(cm^2/sec)**							
	T_{21}-T_0	**T_{31}-T_0**	**T_{21}-T_{11}**	**T_{31}-T_{11}**	**T_{22}-T_0**	**T_{32}-T_0**	**T_{22}-T_{12}**	**T_{32}-T_{12}**
25.1	0.0969	0.0726	0.0731	0.0624	0.1000	0.0726	0.1232	0.1740
28.1	0.0873	0.0693	0.0626	0.0558	0.0836	0.0693	0.1172	0.0919
30.8	0.0992	0.0713	0.0727	0.0544	0.0860	0.0713	0.1134	0.0847
35.5	0.0995	0.0863	0.0760	0.0720	0.1044	0.0821	0.1238	0.0933
38.2	0.0972	0.0806	0.1032	0.0843	0.0822	0.0806	0.1156	0.0997
39.6	0.0889	0.0900	0.0900	0.0775	0.0983	0.0810	0.1212	0.0883
54.4	0.1009	0.0832	0.0684	0.0660	0.1008	0.0832	0.1186	0.0872
56.6	0.0981	0.0846	0.0688	0.0681	0.0969	0.0846	0.1155	0.0923
58.5	0.1048	0.0897	0.0748	0.0727	0.1109	0.0897	0.1301	0.1057
65.6	0.0937	0.0795	0.0666	0.0619	0.0976	0.1495	0.1335	0.2511
69	0.1114	0.0764	0.0944	0.0687	0.0843	0.1551	0.1274	0.2623
71.1	0.1034	0.0983	0.0692	0.0747	0.1080	0.1693	0.1289	0.2205
85.9	0.0949	0.0805	0.0711	0.0672	0.0919	0.1393	0.1160	0.2093
89.4	0.1109	0.0789	0.0817	0.0626	0.1101	0.1596	0.1390	0.2572
98.2	0.1066	0.0838	0.0781	0.0674	0.1144	0.1740	0.1310	0.2973
101.8	0.1094	0.0762	0.0820	0.0595	0.1071	0.1430	0.1271	0.1886
106.8	0.1145	0.0835	0.0920	0.0710	0.0976	0.1793	0.1305	0.3097

4.6 Comparison of Different Measurement Pairs

In this section, the results of different measurement pairs are compared to each other. In order to make the graphs more readable, only the values at two temperatures are shown in each graph. The values at room temperature are compared to 80°C to determine if each pair shows the same behavior at different temperatures. Values at other temperatures are shown in Tables 4.4, 4.6 and 4.7 for SAC305, SAC405 and SAC387, respectively.

Figure 4.20 shows the value of thermal diffusivity of each measurement pair at 25.7 °C and 79.8 °C for SAC305.

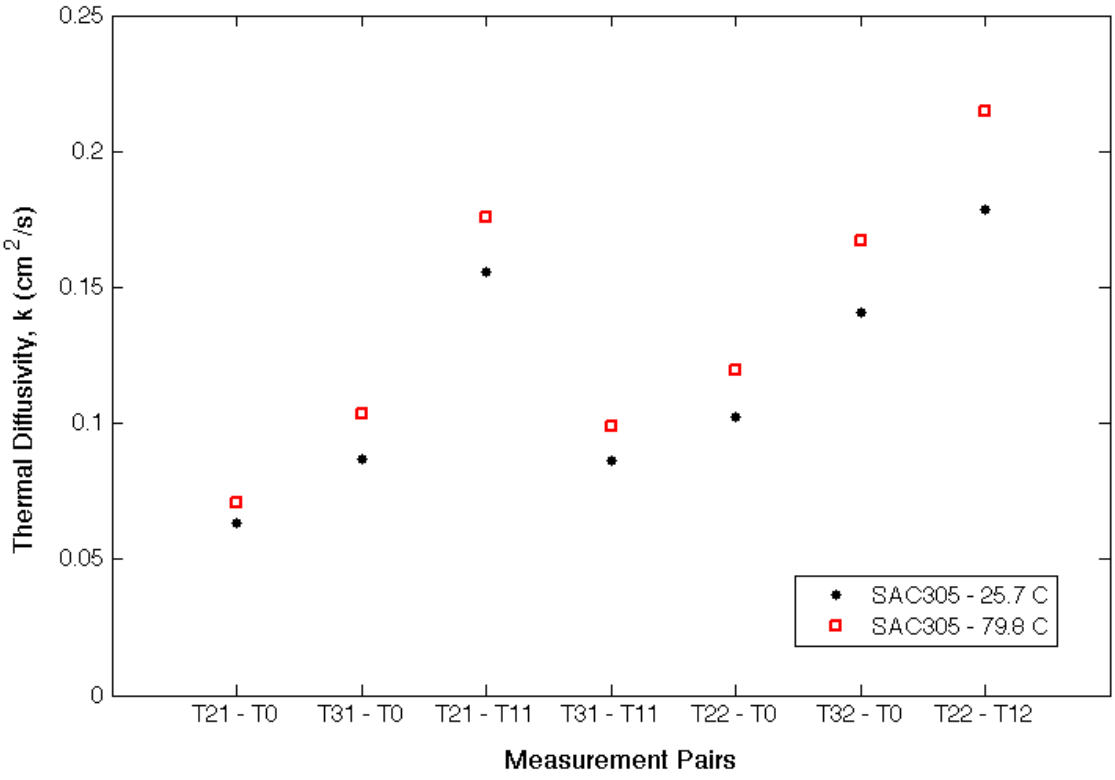

Figure 4.20 The values of thermal diffusivity for each measurement pair at 25.7°C and 79.8°C for SAC305

It can be seen that the values at different measurement points are consistent at both temperatures. T21-T11 and T22-T12 pairs show the highest values of thermal diffusivity compared to the other pairs, whereas T21-T0 pair shows a much lower value. But it should be noted that this trend is maintained at higher temperature.

Figure 4.21 compares the determined values of each pair at 29.3°C and 79.2°C for SAC405 alloy.

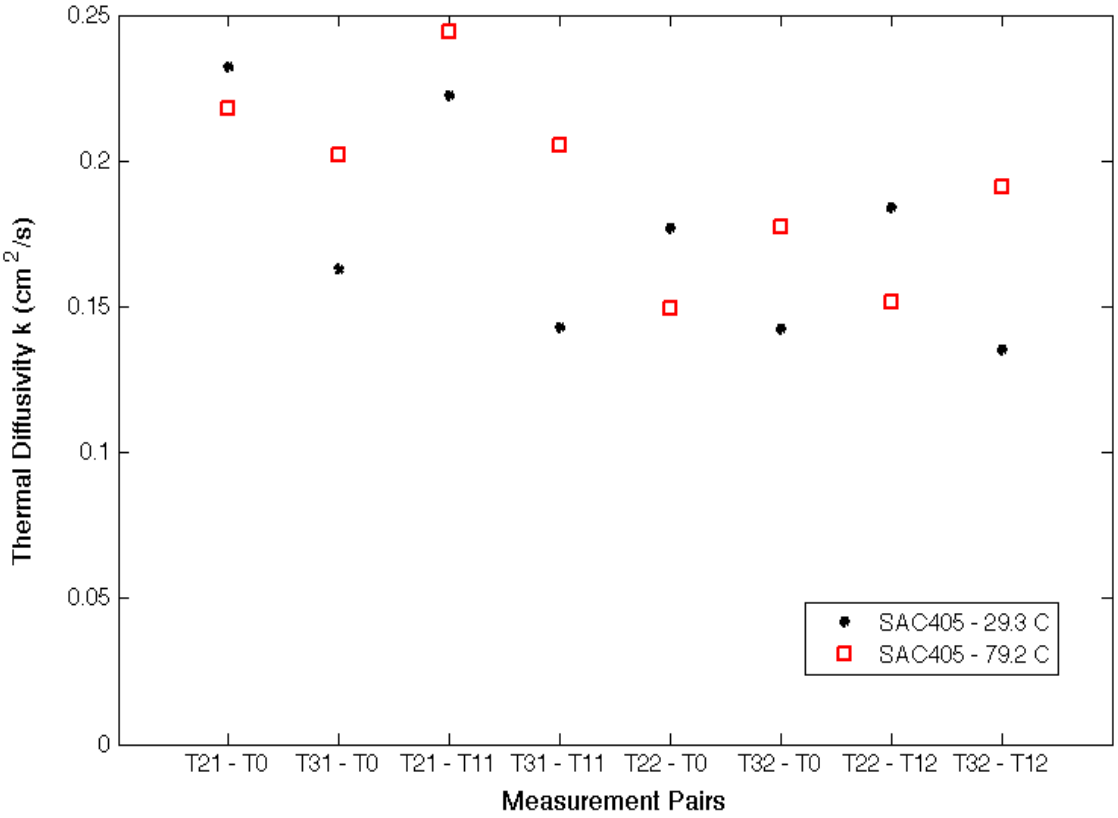

Figure 4.21 The values of thermal diffusivity for each measurement pair at 29.3°C and 79.2°C for SAC305

SAC405 follows the same trend as SAC305 to some extent, but not as strongly. It can be seen that *T21-T0* and *T21-11* are have the highest thermal diffusivities, but as for the lowest, *T32-T0* and *T32-T12* have the smallest values at room temperature, and *T22-T0* and *T22-12* have the smallest values at 79.2°C.

Figure 4.21 shows the value of thermal diffusivity of each measurement pair at 25.1 °C and 85.9 °C for SAC387.

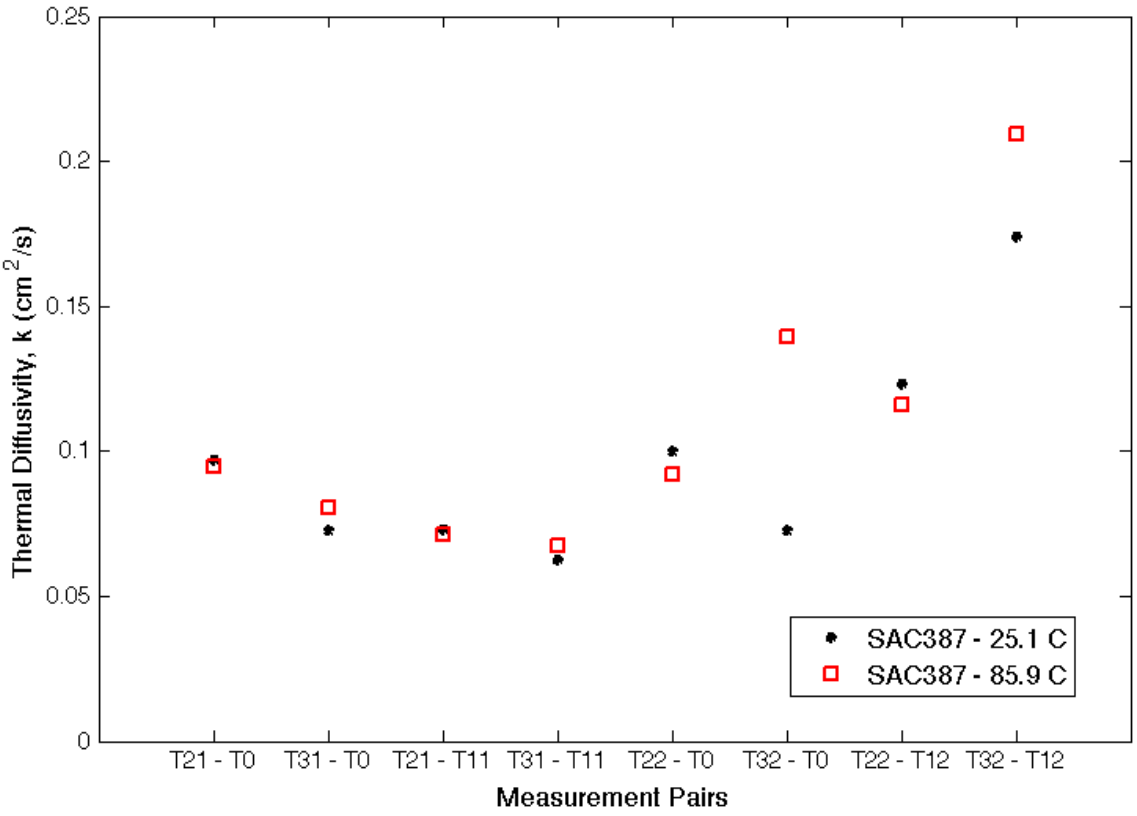

Figure 4.22 The values of thermal diffusivity for each measurement pair at 25.1°C and 85.9°C for SAC387

In this alloy, all measurement points follow the same trend and it can be seen that for T21-T0, T31-T0, T21-T11, T22T0 and T22-T12 pairs the results are very close, whereas the T32-T0 pair shows the irregular behavior where is has lower thermal diffusivity compared to other pairs at room temperature, and higher at 86°C. This irregular behavior of T32-T0 pair was also shown in Figure 4.19.

4.7 Microstructure

In order to investigate the non-uniform properties observed at different points on the sample, the microstructure was studied using an optical microscope. As expected

from the diagram phases, all three Sn rich phase, Cu_6Sn_5 phase, and Ag_3Sn phase were recognized in the microstructure.

Figure 4.23 shows the microstructure of SAC305 with 60X magnification at 3 different points on the sample. It can be seen that the amount and distribution of the intermetallic compounds is not uniform at different points of the sample. The amount of the needle-like Ag_3Sn phase increases from 4.23a to 4.23b and 4.23c, and also the amount of the Sn-rich region (light color) changes at different locations.

Figure 4.24 shows the microstructure of SAC405 with 60X magnification. This set of images also shows how the microstructure changes in direction and size along the sample. It can be seen that from 4.24a to 4.24b the direction of the dendritic structure changes and in 4.24c the amount of the Sn-rich region is increased (thicker dendritic structure).

The microstructure of the eutectic compound (SAC387) is presented in Figure 4.25. The fine eutectic structure (dark background) is penetrated by Sn-rich dendritic beta phase.

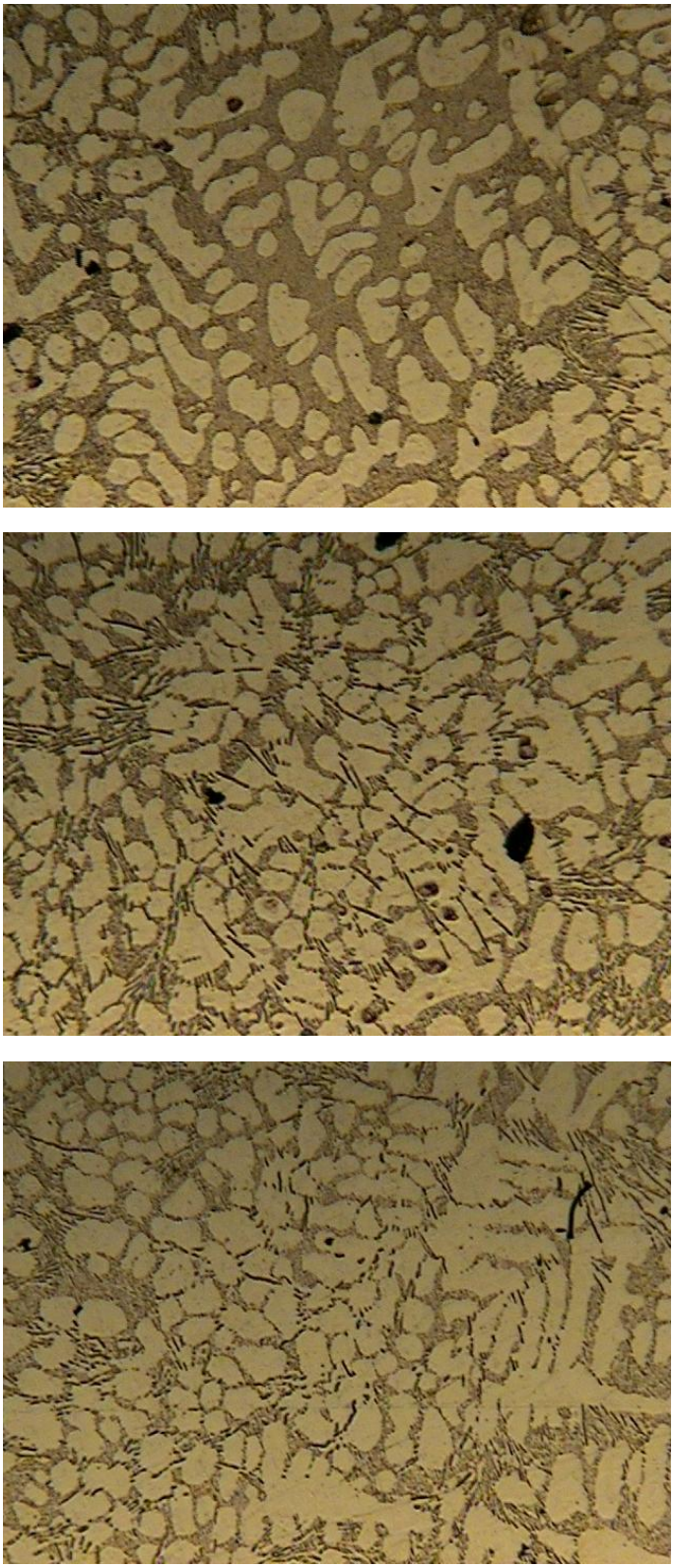

Figure 4.23 The microstructure of SAC305 with 60X magnification at 3 different points on the samples

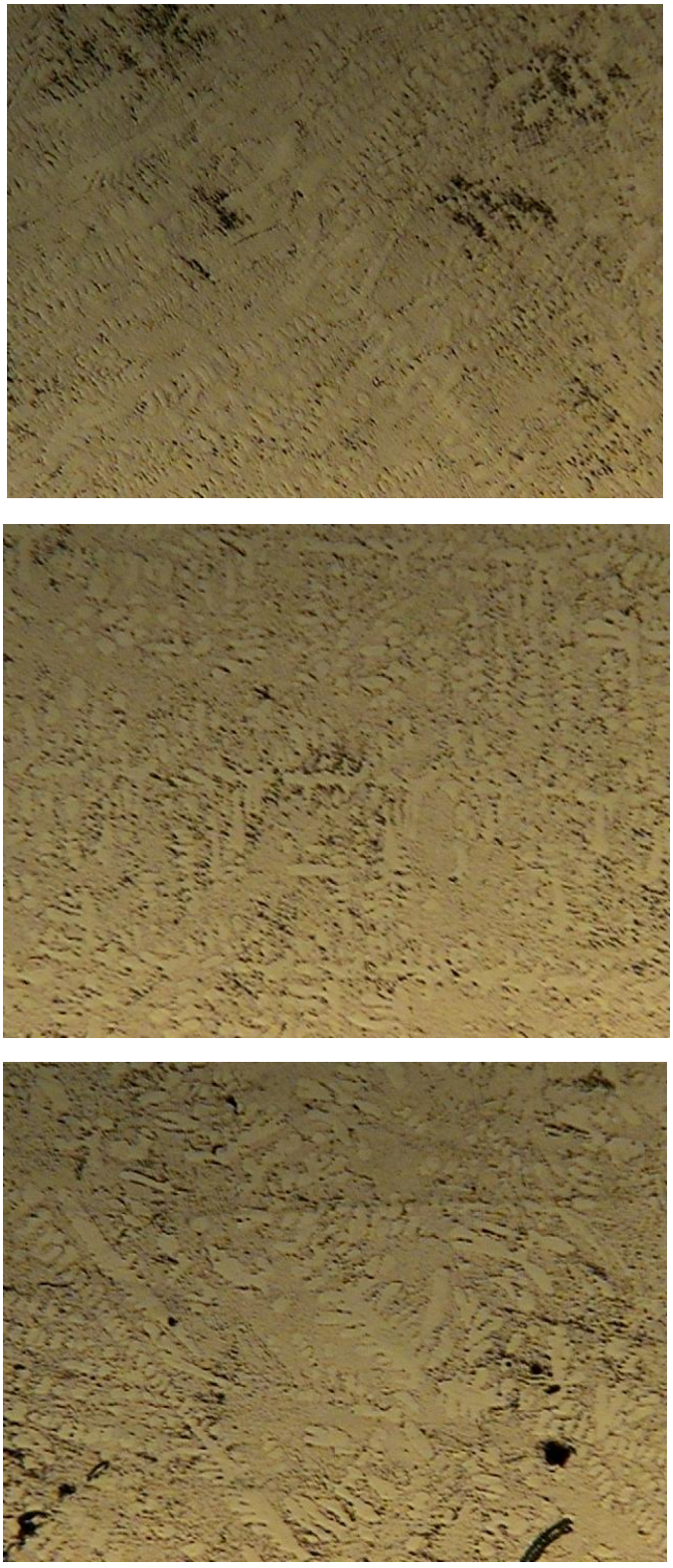

Figure 4.24 The microstructure of SAC405 with 60X magnification at 3 different points on the samples

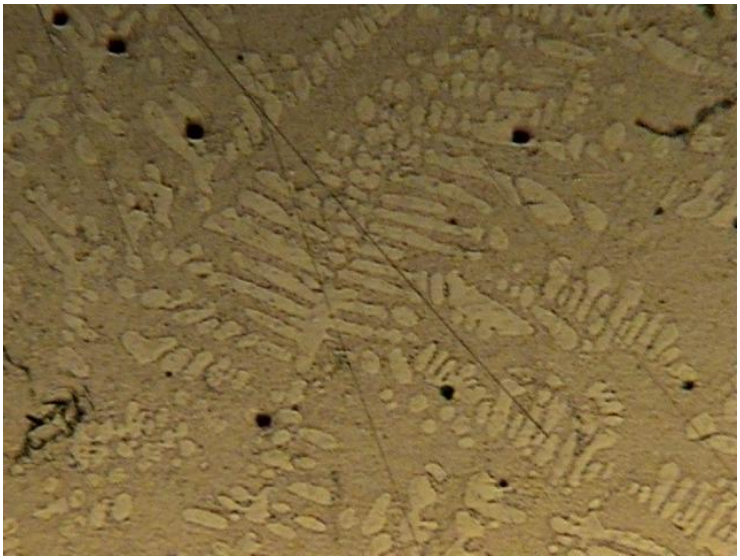

Figure 4.25 The microstructure of SAC387 with 60X magnification

Figures 4.26 to 4.28 show the microstructure at different points on each sample. (To be compared to the numerical results of thermal diffusivity). Figures 4.26.a and 4.26.b each show one half of the sample for ease of comparison. The values of thermal diffisivity between the points that the images are taken from are shown on each image. Also there's a schematic image of each half of samples, showing where the images were taken on each sample. It can be seen in these micrographs that the microstructure is strongly non-uniform and differ considerably from one point of the sample to the other with respect to the size and distribution of the microstructures. The mushroom-like Sn-rich regions differ in size and also the amount, direction and density of the intermetallic compounds is non-uniform throughout the samples.

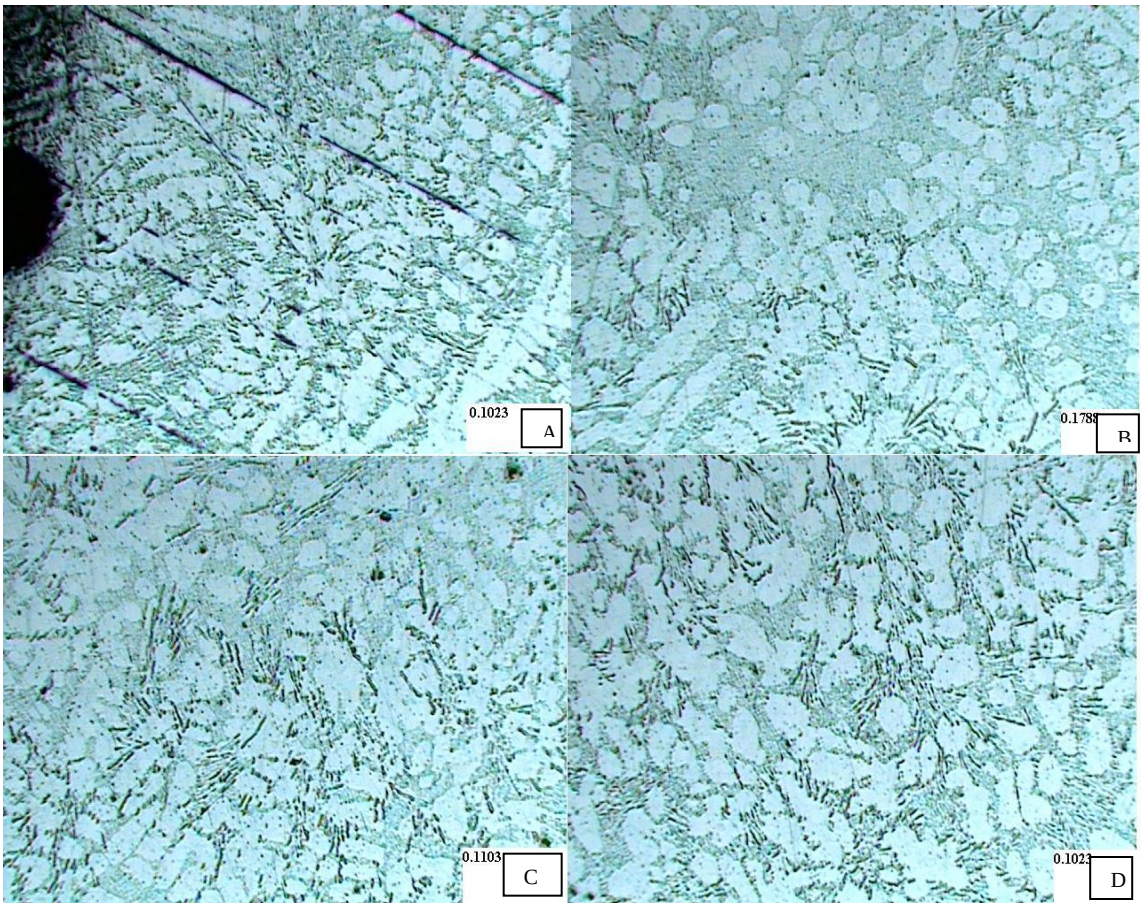

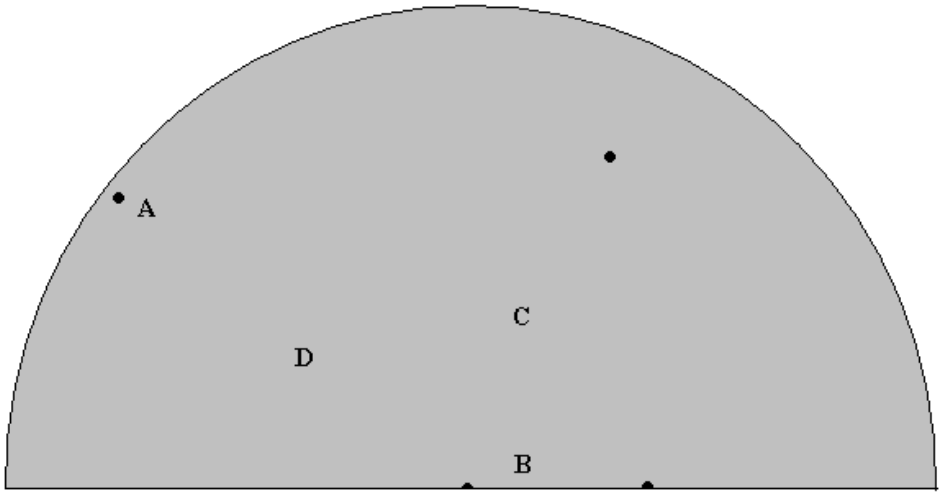

Figure 4.26 The microstructure of the upper half of SAC305 at different points and the areas on the sample where the images were taken

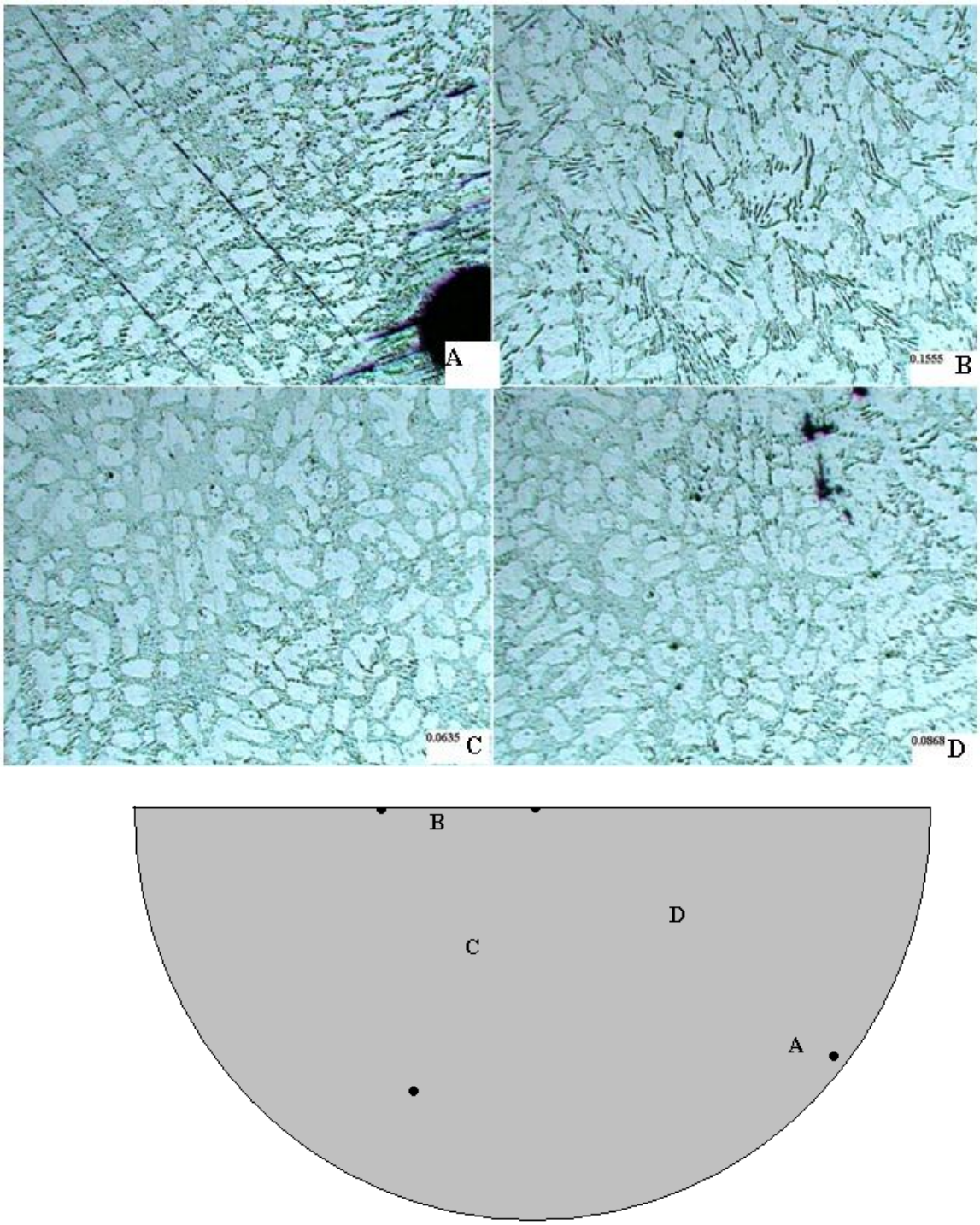

Figure 4.27 The microstructure of the lower half of SAC305 at different points and the areas on the sample where the images were taken.

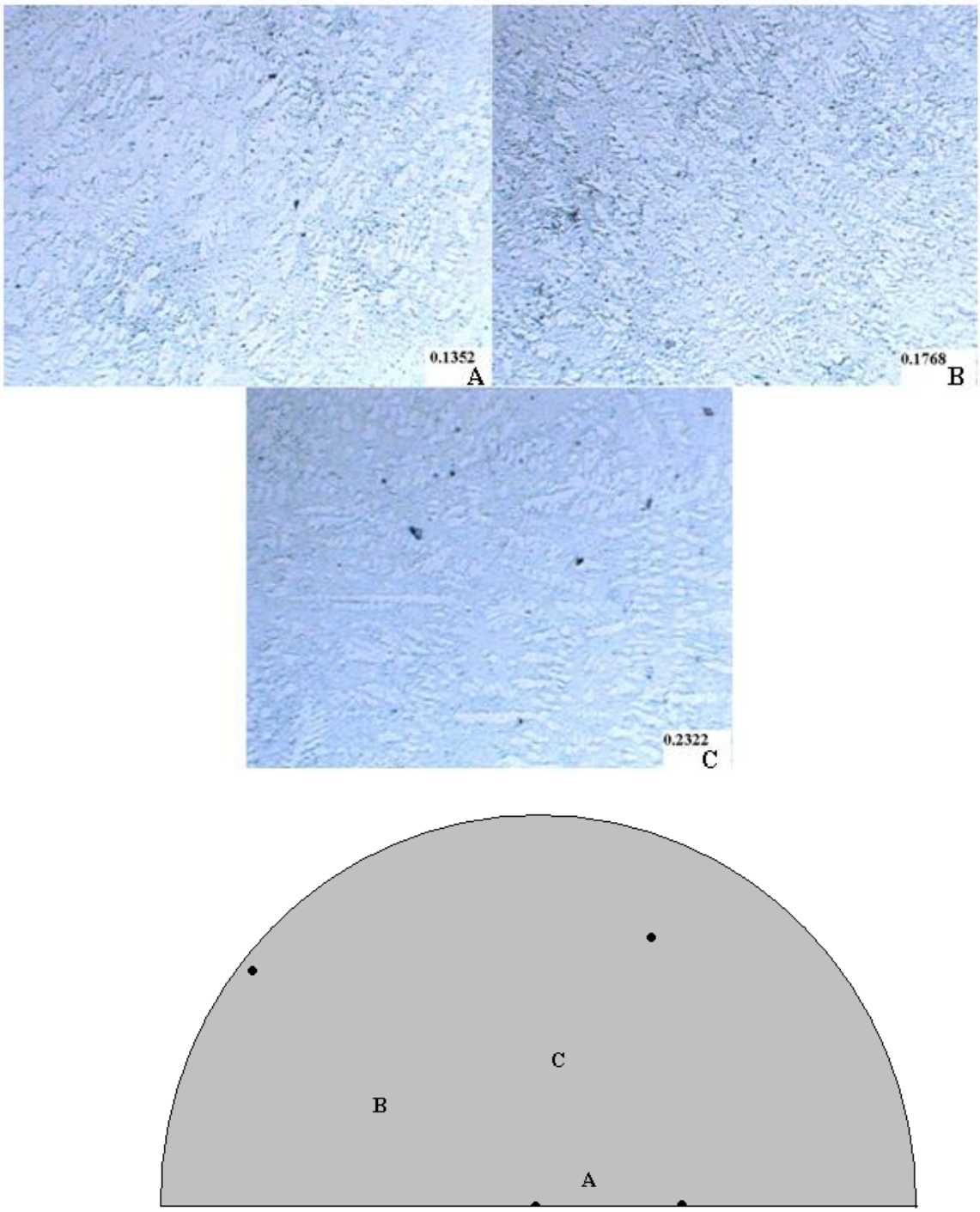

Figure 4.28 The microstructure of the upper half of SAC405 at different points and the areas on the sample where the images were taken.

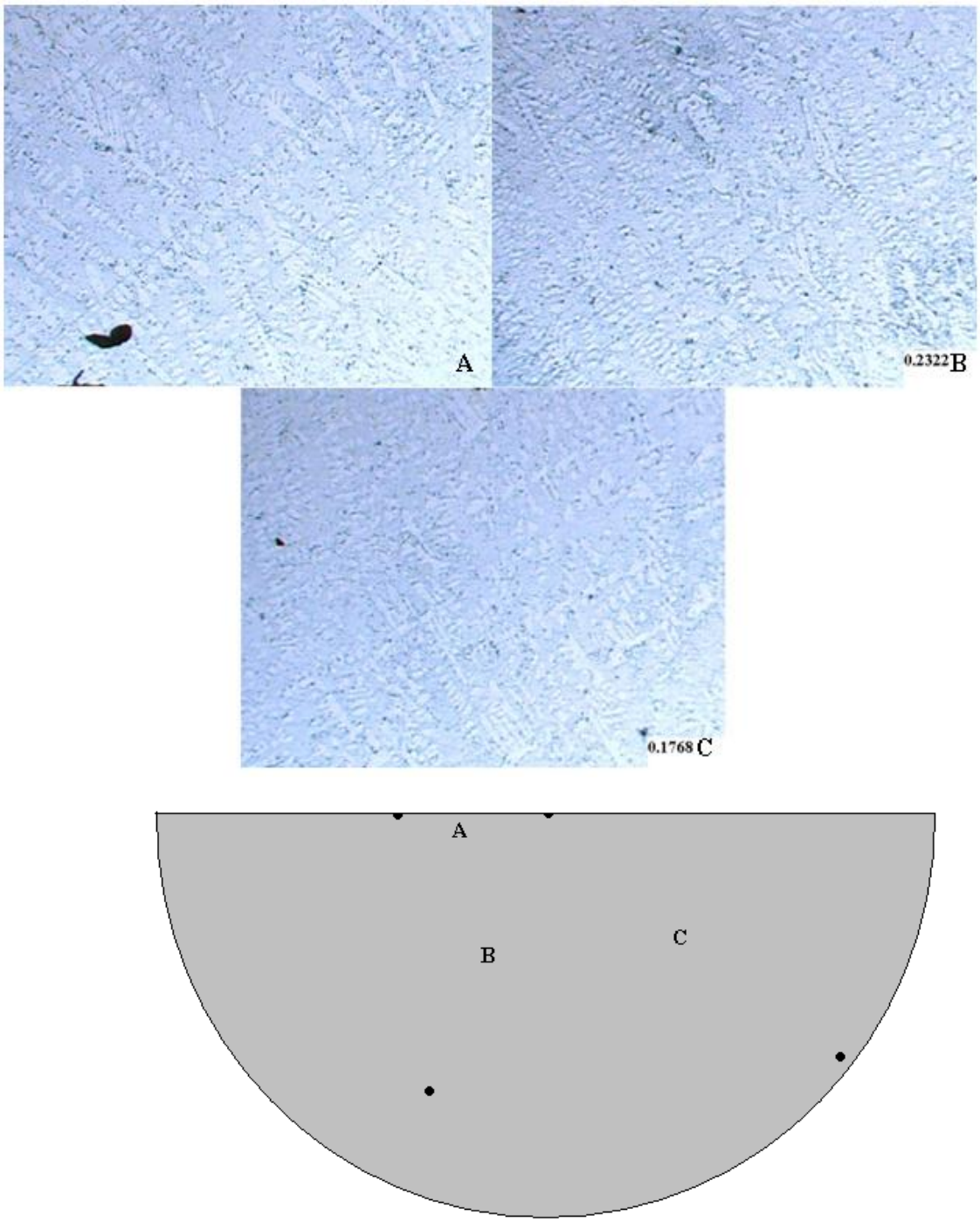

Figure 4.29 The microstructure of the lower half of SAC405 at different points and the areas on the sample where the images were taken.

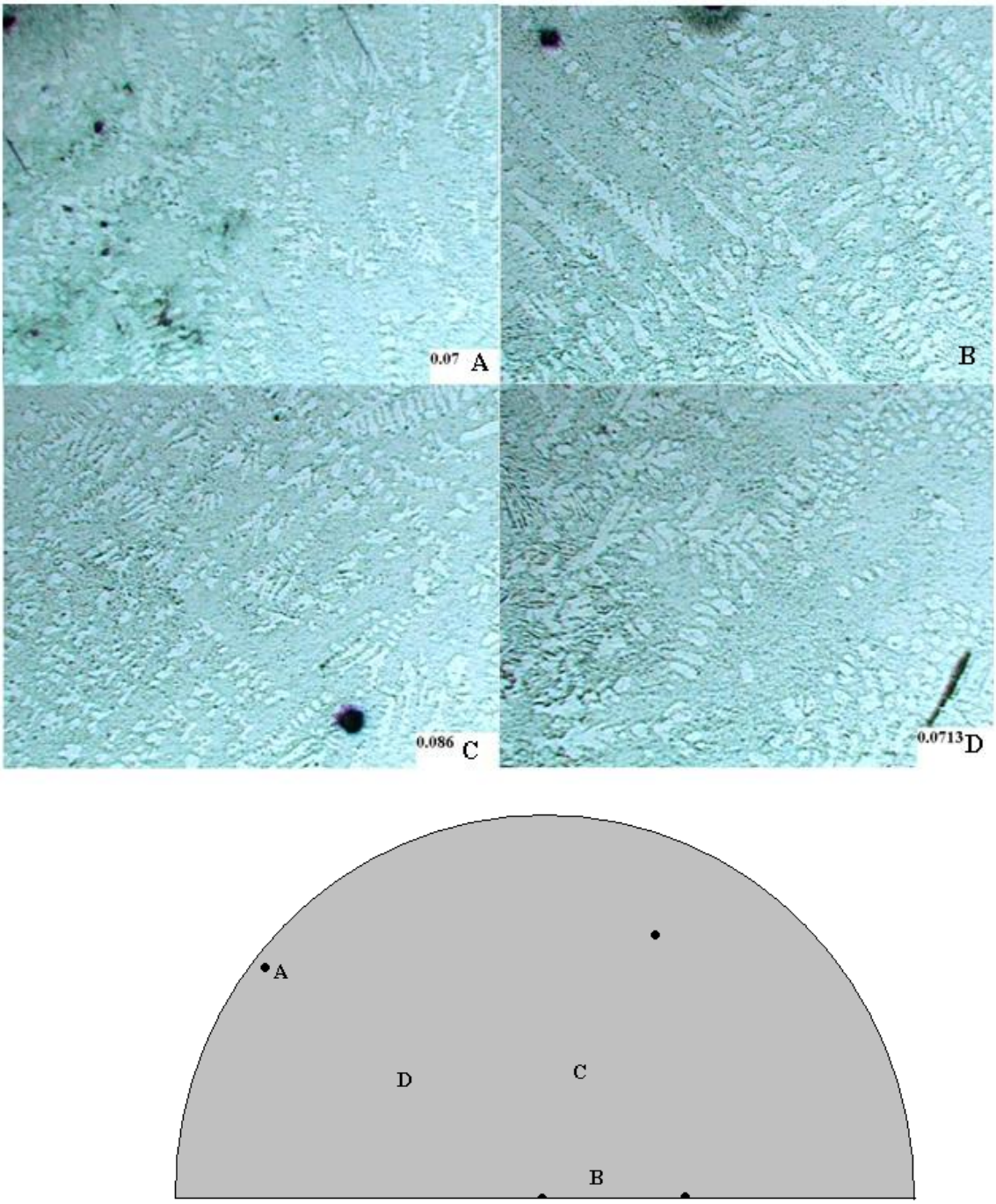

Figure 4.30 The microstructure of the upper half of SAC387 at different points and the areas on the sample where the images were taken.

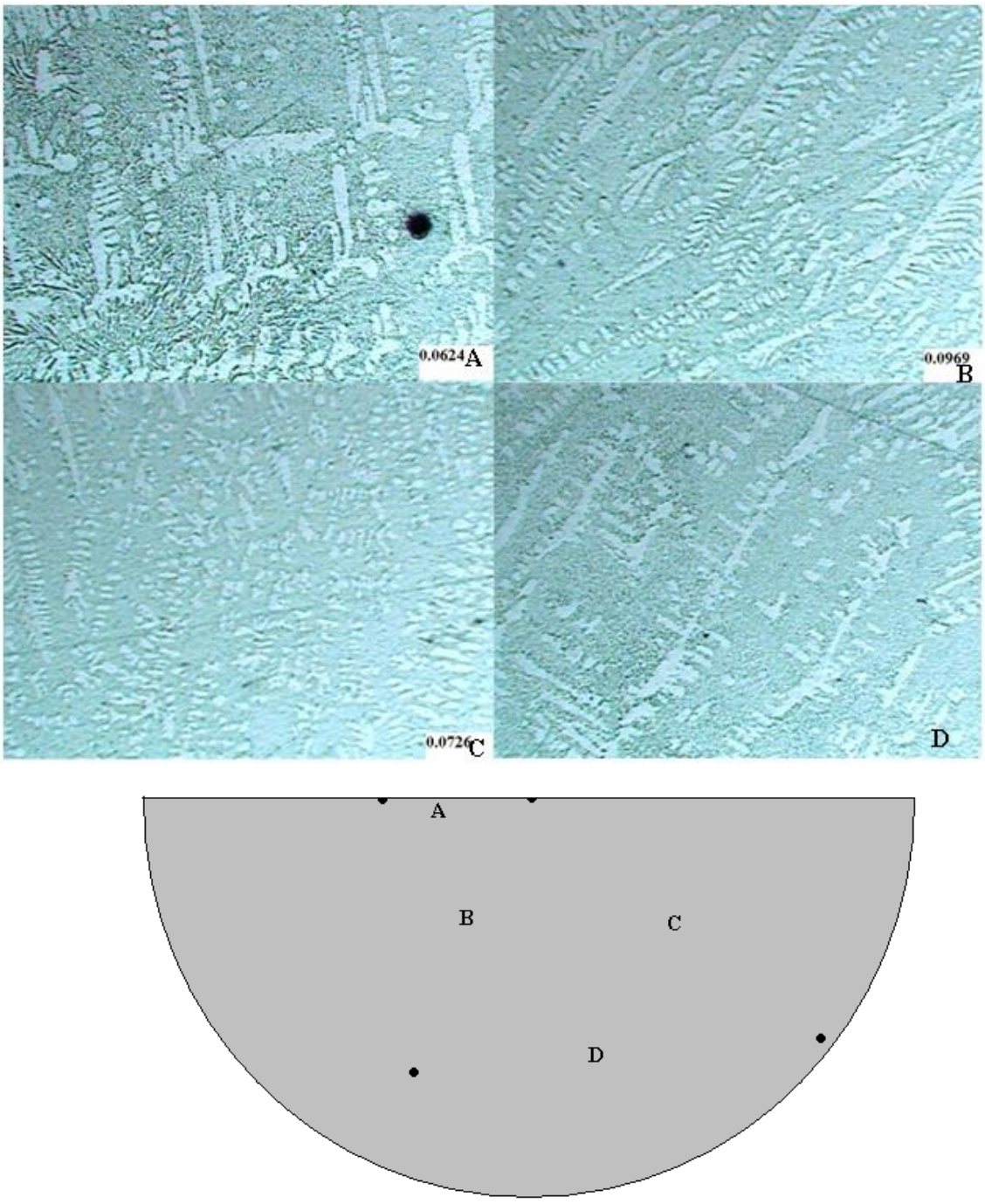

Figure 4.31 The microstructure of the lower half of SAC387 at different points and the areas on the sample where the images were taken.

CHAPTER 5
SIMULATIONS

As it was shown in Chapter 4, the values of thermal diffusivity show extreme differences at different locations on the sample, which suggests the effect of grain structure, and the shape and orientation of the intermetallic phases on the overall thermal diffusivity. The microstructure was analyzed in Section 4.7 which showed the non-uniform distribution of the intermetallic compounds and grain boundaries along the bulk of the sample. In order to simulate this behavior, different shapes (dendritic, bulk, etc.) and structures of the second phase were defined and their effect on the overall thermal diffusivity was determined. Also in order to show the effect of dislocations and grain boundaries, a layer of low thermal diffusivity region was defined around the second phases to represent the dislocations which slow down the rate of heat propagation.

This chapter explains the simulation process which was performed using COMSOL Multiphysics. The numerical modeling was performed in 2D and 3D. In Section 5.1 COMSOL and its different features are introduced, in Section 5.2 the procedure of the simulation is explained, and in Section 5.3 the results are shown and compared to those of the experimental procedure.

5.1 Introduction to COMSOL Multiphysics

COMSOL (previously called FEMLAB) is a finite element solver and simulation software. The company was founded by Littmarck and Saeidi in 1986. The first version of the software under the name of COMSOL was published in 1998 [21].

The current version of COMSOL Multiphysics package consists of 14 modules, specific to each application. These modules are AC/DC, Acoustics, Batteries and Fuel Cells, CFD, Chemical Reaction Engineering, Earth Science, Electrodeposition, Geomechanics, Heat Transfer, MEMS, Microfluids, Plasma, RF, Structural Mechanics and subsurface Flow.

There are also two modeling tools that are the Material library and Optimization Module. Material Library consists of an extensive materials data base with different categories of materials with physical and chemical properties, which can be changes temporarily by the user.

COMSOL can also be used in interface with other products such as CAD, Autocad, Inventor, MATLAB, Pro/ENGINEER, SolidWorks and SpaceClaim. For the present work, COMSOL 4.1 with Heat Transfer and Materials Library modules were used. At the time this text is being prepared, version 4.2 is being released.

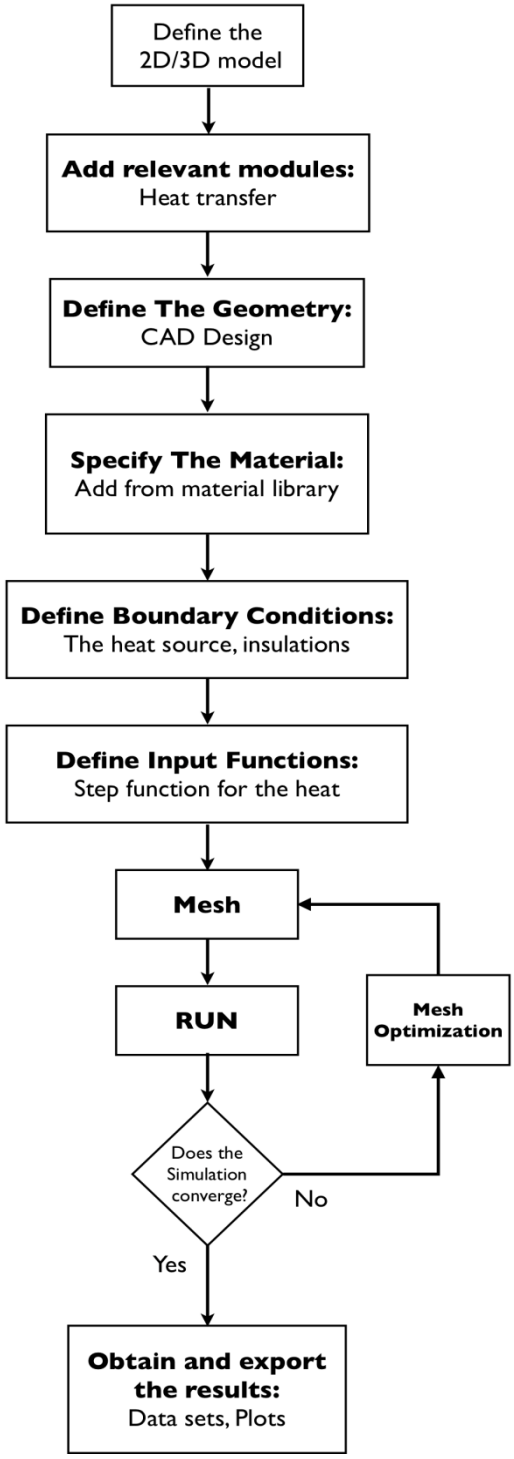

Figure 5.1 The flow chart of the simulation procedure

5.2 Simulation Procedure

Figure 5.1 shows the flow chart of the simulation process. The first step to define a model in COMSOL is to define the dimensions and the study type. In the case of this study, the model was a 3D time dependant model. The module can be added any time during the simulation. Heat transfer module was selected for this model.

The next step is to define the geometry units, i.e., the length and angular units. Centimeters and degrees were chosen as the units.

A simple geometry is shown in this section. A cylinder with radius of 3cm and 1cm height is created, and the second phase is presented as a cube inside of the cylinder. A simple circle of radius 3cm is first drown in geometry section, then a square of 1cm side is added inside it. Two points are also added to represent the thermocouple measurement points (points 1 and 2 in Figure 5.3). Then the geometry is extruded for 1cm to result in the sample geometry used in the experiment. These steps are shown in Figures 5.2 and 5.3.

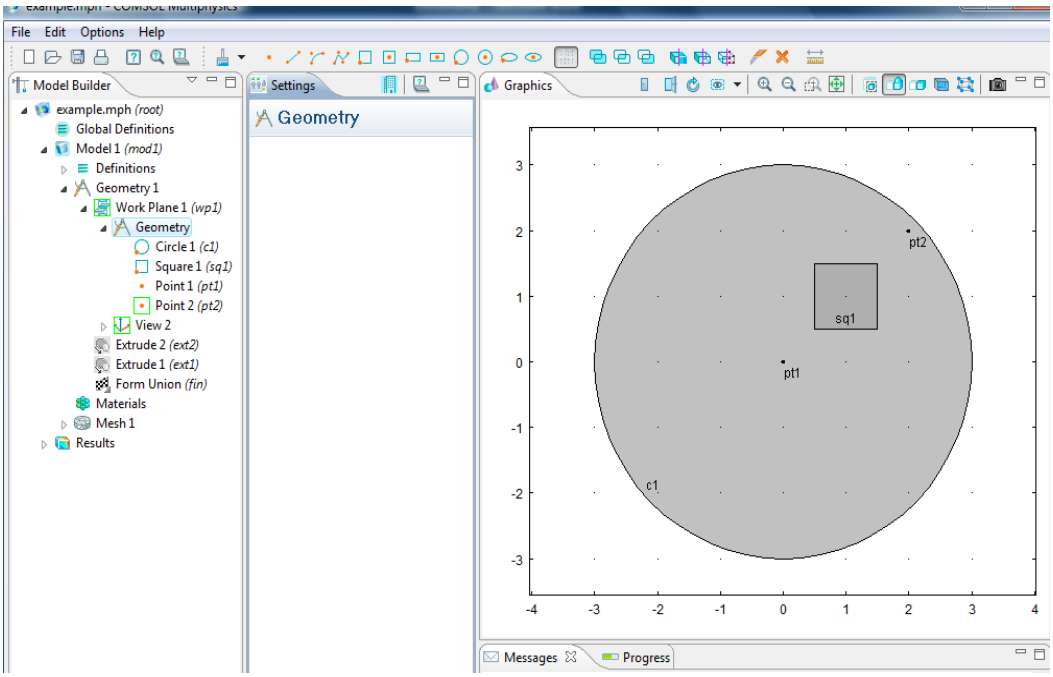

Figure 5.2 An example of a 2D geometry and the measurement points

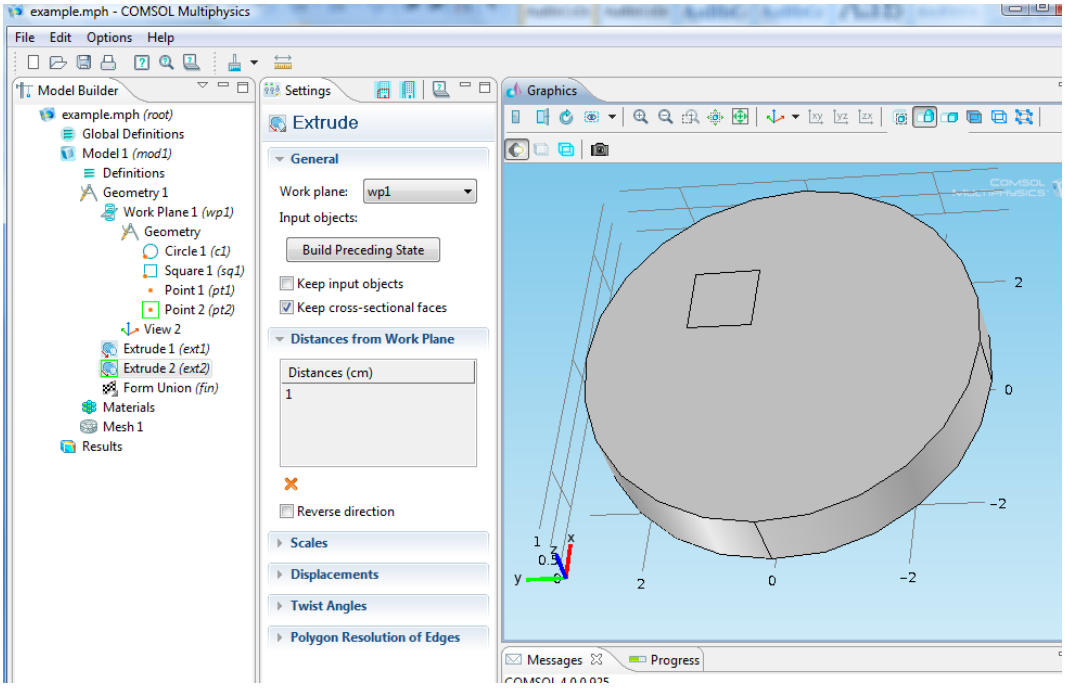

Figure 5.3 The 2D geometry is extruded to result in a cylinder with a cube of the 2nd phase

The next step is to define the materials and their properties. COMSOL's materials library was used to select two alloys with considerable difference in thermal conductivity and heat capacity. The second phase was given the material with the higher thermal diffusivity. The values of the thermal diffusivity are presented in Section 5.3.

After selecting the materials, the heat source needs to be defined. In order to simulate the experimental procedure, a "boundary heat source" was used, and the cylinder walls were selected to be the heat source. The amount of heat was then chosen to be 35000 W/m^2 and a step function was defined to apply the heat only for 2 seconds.

The top and bottom of the cylinder were defined to be isolated, and the initial temperature was set as 293.15K. The surface radiosity was also set as zero.

The last step is to mesh the geometry. Due to the simplicity of this geometry, the meshing is straightforward. The free tetrahedral shape was used, and different mesh sizes were tried to assure convergence. Convergence is defined as the improvement of the solution when the mesh is refined [22]. Four different mesh sizes are shown in Figure 5.4. In the case of the example here, all four mesh sizes result in the same results. But as more second phase sections are added to the sample, and the sizes decrease, much smaller mesh sizes become necessary to keep the results accurate. Using this procedure, the optimal mesh size was determined in each case.

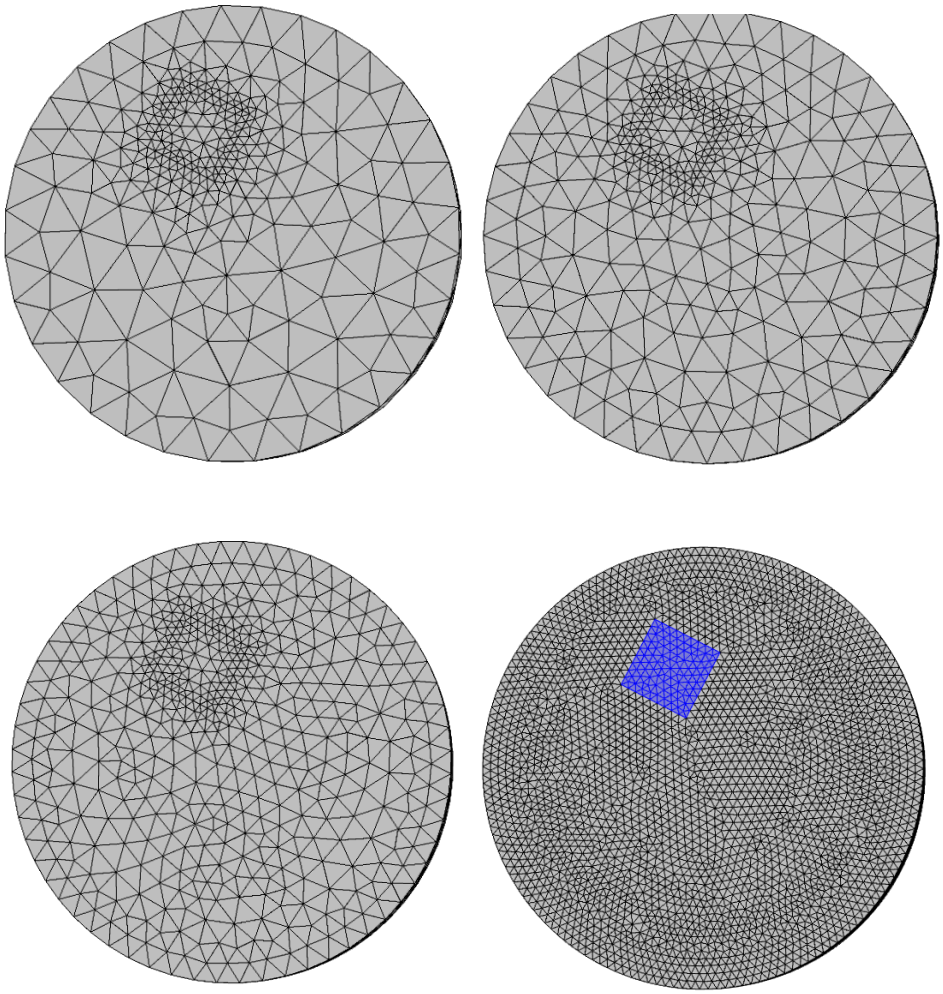

Figure 5.4 Four different mesh sizes for the sample geometry

After the suitable mesh size is determined, the program is set to record the data for 50 seconds with 0.1sec intervals to make sure that the temperature reaches equilibrium. Then the program is run and the temperature versus time data is recorded.

5.3 Simulation Results and Discussion

In this section, the results of COMSOL simulations are shown starting with the more simple results to more complex models. In order to make the models simpler, the results are shown only at two measurement points. It was shown in before that the results would be the same for other measurement points.

Section 5.3a shows the results of a simple case where the effect of the size of the second phase is studied.

5.3.a The Size Effect-Rectangular Second Phase

In this case, a rectangular piece of the second phase is placed between the two measurement points. The two measurement points are at x=0.5cm and x=2.5cm and the length of the second phase is 2cm. The thickness of the second phase increases in 0.2cm increments to make up for 0 to 90% of the distance between the measurement points. As it was mentioned before, the Cp (specific heat capacity) of both phases is assumed to be 400 J/kg.K and the Heat conductivity of the second phase is defined 2 times higher than the background phase (k=80 W/m.K for the second phase, and k=40 W/m.K for the background).

Figure 5.5 shows the placement and the size increase of the second phase block. The thermal diffusivity results are shown in Figure 5.6. It can be seen that the increase in the thermal diffusivity in slightly non-linear, which is due to the heat profile on the side walls of the second phase rectangle. In order to prove this point, a ring-shaped second phase was used in Section 5.3.b.

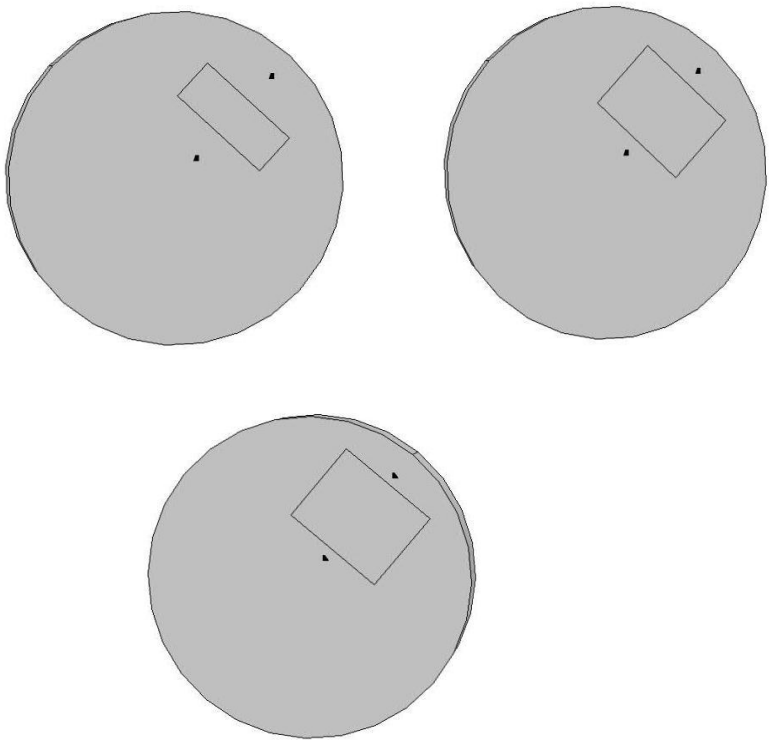

Figure 5.5 The simple case of size effect in rectangular second phase increasing from 0 to 90%

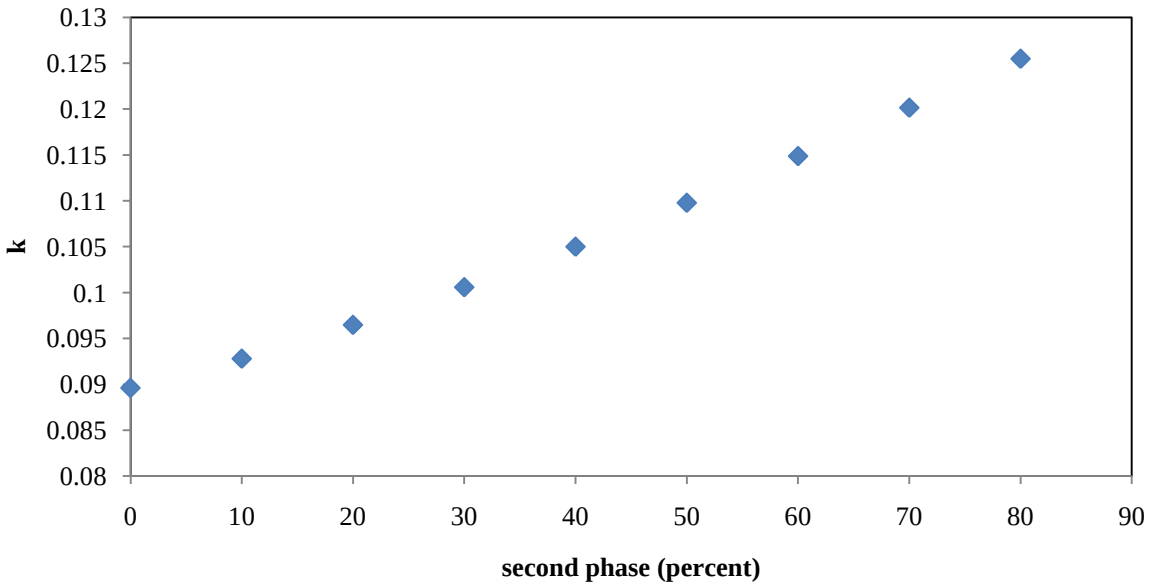

Figure 5.6 Shows the size dependence of the thermal diffusivity with increasing the size of the rectangular second phase.

5.3.b The Size Effect–Ring Shaped Second Phase

In this section, the previous model was repeated for a ring-shaped second phase in order to eliminate the heat exchange on the side walls of the second phase block. The material properties where defined the same as before, and the thickness of the ring was increased in each step. Figure 5.7 shows the set-up of the model, and Figure 5.8 shows the results. It can be seen that in this case, the effect of heat-loss at the walls is eliminated and the trend of thermal diffusivity increase with the size of the second phase is completely linear.

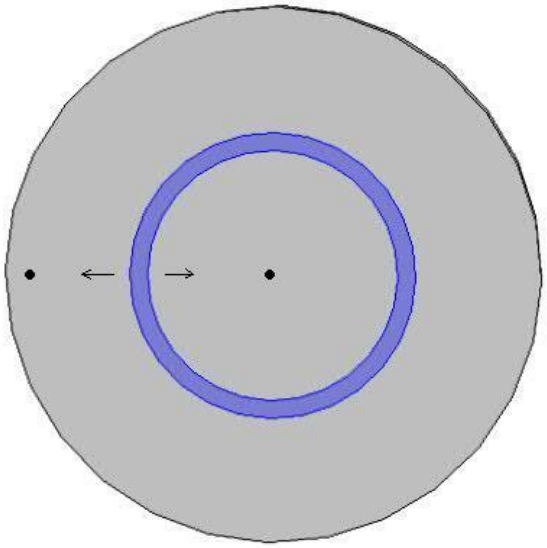

Figure 5.7 The simple case of size effect in a ring-shaped second phase increasing from 20 to 90%

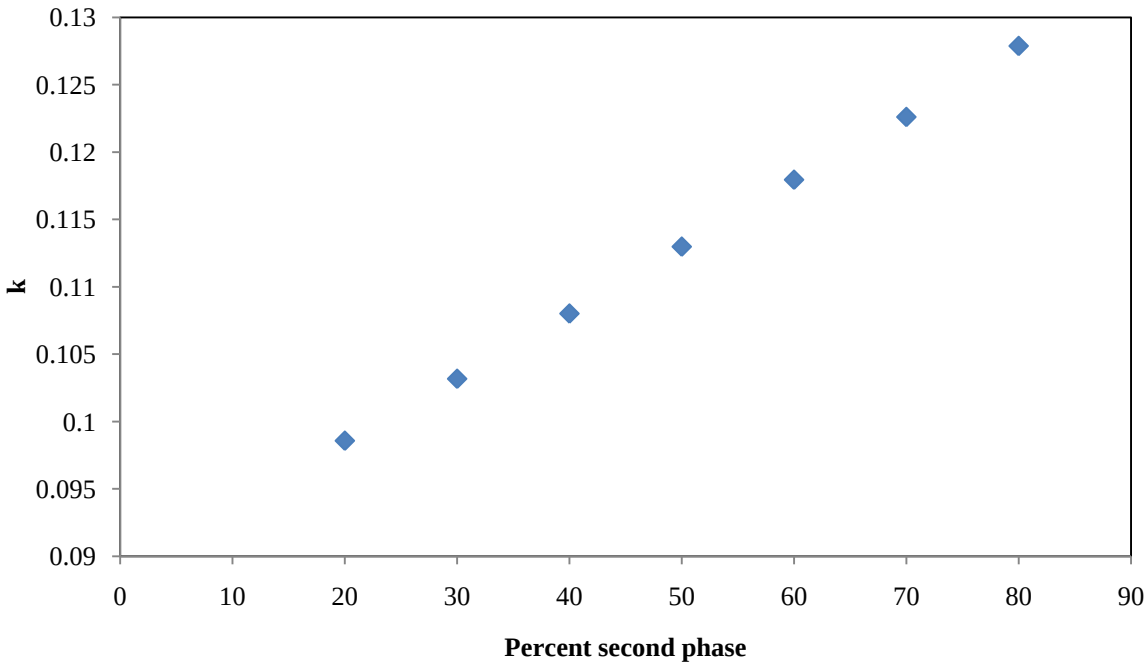

Figure 5.8 The linear dependence of thermal diffusivity on the percentage of the ring-shaped second phase.

5.3.c The Distribution Effect-Rectangular Second Phase

In this section, The sum of the second phase block sizes are the same but they are set in one, two and three pieces to show the effect of the second phase distribution in a very simple case.

Figure 5.9 shows the model set-up where the block of the second phase is divided into two and three pieces with constant length. Figure 5.10 shows the results of this case.

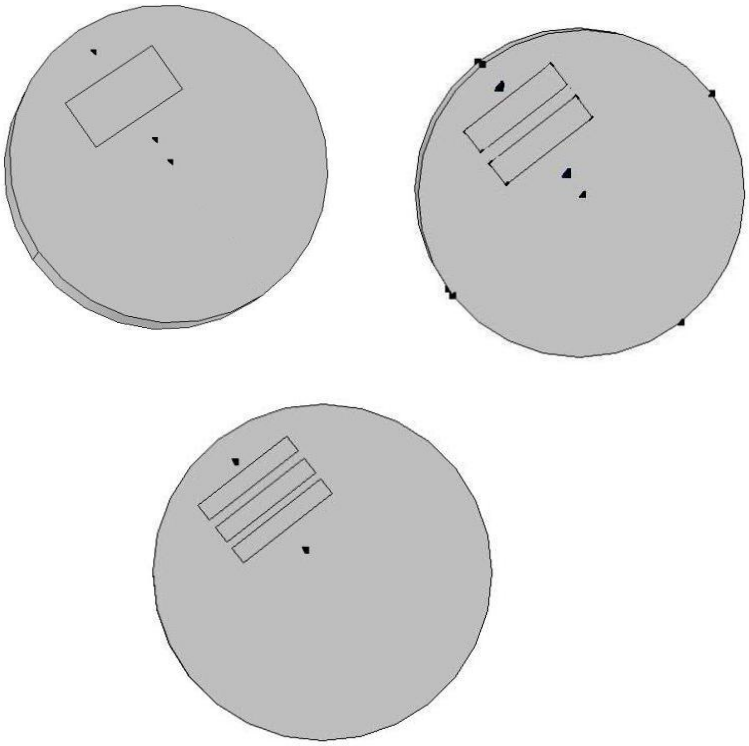

Figure 5.9 A simple case of determining the effect of distribution of the second phase on the overall thermal diffusivity.

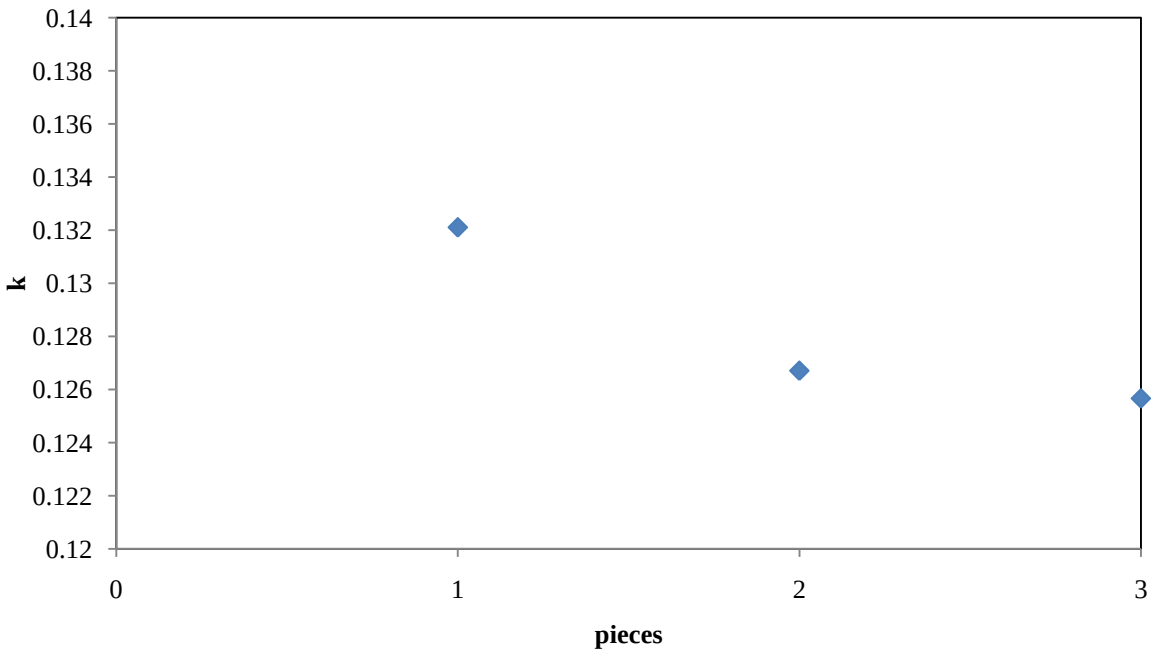

Figure 5.10 The overall thermal diffusivity decreases slightly as the second phase is divided into more pieces.

It can be seen in Figure 5.10 that the overall thermal diffusivity shows a slight decrease as the block of the second phase is divided into more pieces. This shows that as the heat enters the phase with higher thermal diffusivity and exits, each time there is heat propagation in the transition that would decrease the overall thermal diffusivity. This is why although the total amount of the second phase is the same; the final thermal diffusivity values are slightly different. This also suggests the effect of boundary mismatch as the heat enters and exits a phase, which is discussed later in this chapter.

5.3.d The Distribution Effect-Multiple Squares of Second Phase

In this case, the total amount of the second phase is 25.5% of a quarter of the circle. The second phase blocks in this case are 5, 10 and 25 squares distributed

randomly in a quarter of the sample, and the sum of their areas are the same. Figure 5.10 shows the distribution of these phases. In Figure 5.11.a the second phase is divided into 5 pieces. The total area is 1.802 cm^2 (25.5% of the area of a quarter of the circle). So in the first case, the length of each square side is 0.6 cm. In Figure 5.11.b there are 10 pieces (each with a side of 0.42 cm), and in Figure 5.11.c there are 25 squares of the second phase (each with a side of 0.27 cm).

The measurement points are placed at x=0 and x=2.8 cm. There is one measurement pair for case a, 3 for case b and 5 for case c. The slopes are shown in Figure 5.12.

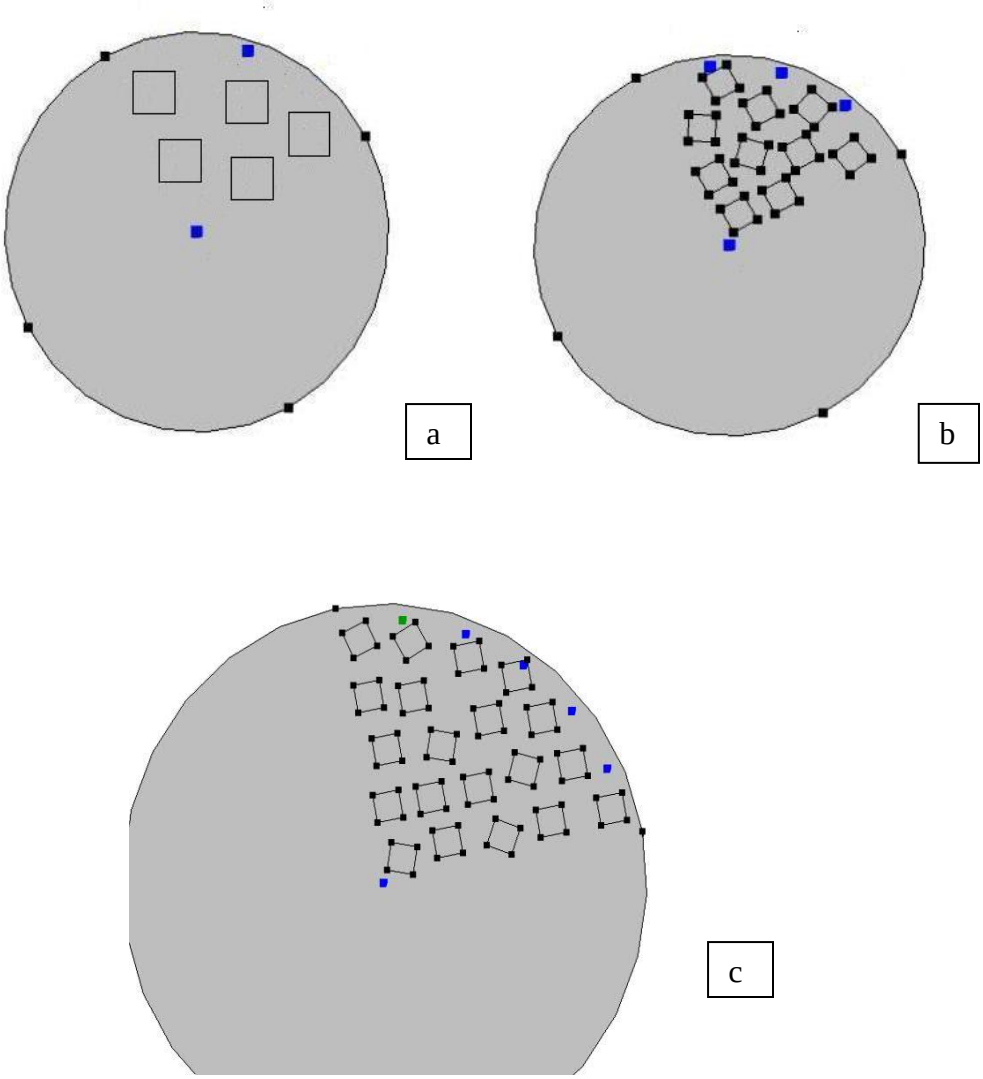

Figure 5.11 The distribution of the second phase squares with the same overall area of 25.5% of the area of a quarter of the circle.

Table 5.1 The slope values for three different distributions of the second phase.

a	b	c
0.1116	0.1099	0.0991
	0.1124	0.1006
	0.1140	0.1008
		0.1007
		0.0991

It can be seen that the first case with bigger blocks of the second phase shows the highest thermal diffusivity and as the blocks become smaller and more distributed in the second and third case, the values decrease which is in agreement with the results from the previous sections. It can also be seen that as the size becomes smaller and the distribution more normal, the values between different measurement points become closer.

5.3.e The Width Effect

In this section the length of the second phase block is held constant and the width is increased. This is to show that not only the length of the area between the two measurement points that is occupied by the second phase affects the overall thermal diffusivity, but also the width of the block changes the heat propagation around the block, hence changing the thermal diffusivity values. In this case the distance between the two measurement points is 2cm and the length of the block is a constant 1 cm. The width is

increasing from 0.2cm to 1cm with 0.1cm increments. The set-up and the results are shown in Figures 5.12 and 5.13, respectively.

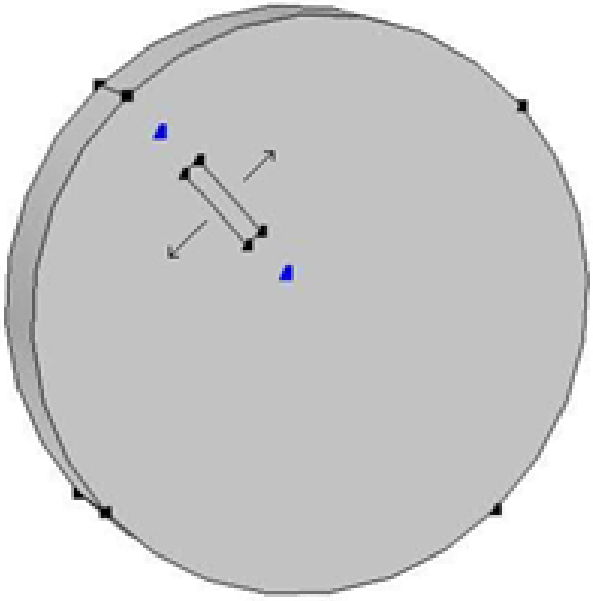

Figure 5.12 The set-up for the second phase width effect on the overall thermal diffusivity

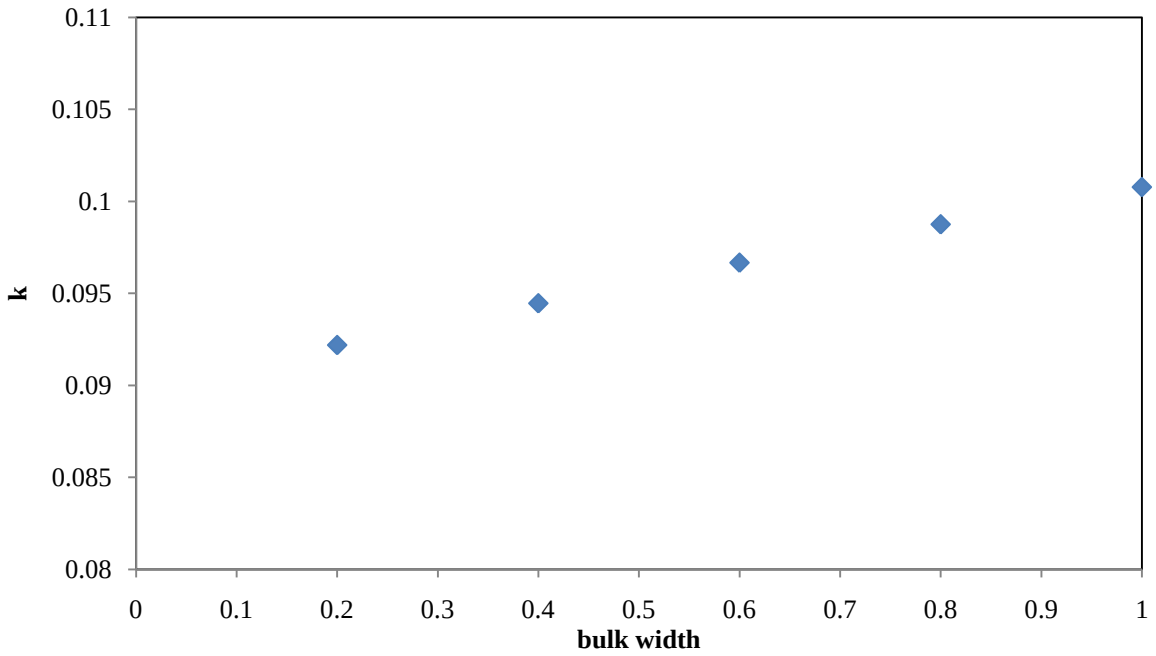

Figure 5.13 The effect of the second phase width on the overall thermal diffusivity

5.3.f Effect of Dendritic Arms

In order to achieve a model closer to the actual dendritic structure observed in Section 4.6, dendritic arms were added to the initial block of the second phase, and the length and number of the arms were changed to see the effect on the thermal diffusivity between the two measurement points. The body of the dendrite was held constant and the length and number of the arms were increased. Figures 5.14.a through f show the model set up. The value of the slope of the temperature gradient between the measurement points versus time in mentioned under each model. In Figure 5.14.a there is one short arm on each side of the block, and the model shows the lowest thermal diffusivity. Then the lengths of the arms are increased by a factor of 2.5 in 5.14.b and the overall thermal diffusivity has increased by 0.75%. In case c, there are two short arms on each side and

the results are higher than the case with one short arm, and lower than one set of long arms. This is repeated for 2 long arms (5.14.d) and three short arms (5.14.e) which show similar results. Figure 5.14.e shows the case with one set of long arms and 2 sets of short ones, and as one expects, the results lie between cases d and e.

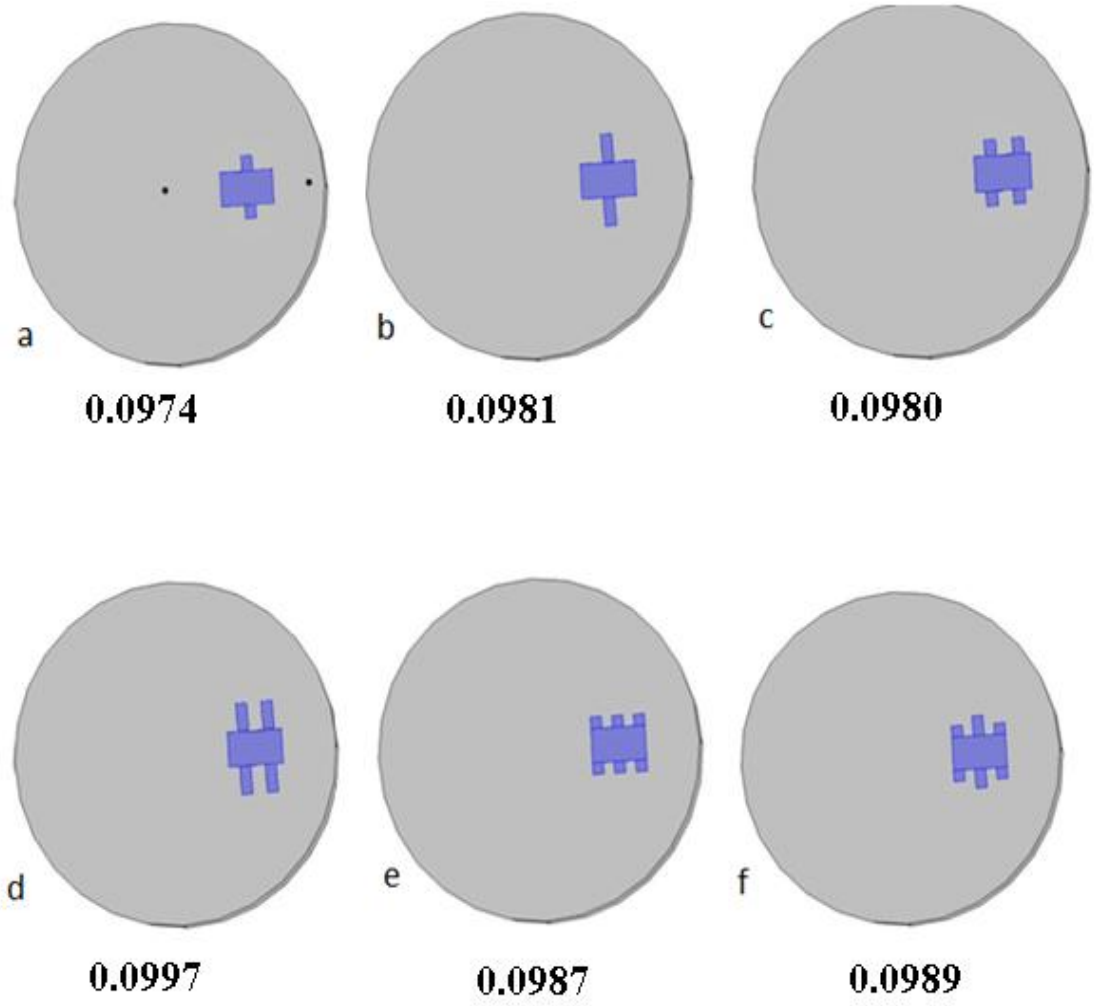

Figure 5.14 Modeling the dendritic arms with constant body size and the resulting values for the slope of $\ln\Delta T$ vs. t

5.3.g Boundary Mismatch Effect

In this section, the effects of boundary mismatch are studied to some extent. In order to simulate the dislocations and boundary mismatch at the interface between different phases, a thin layer of a third material was placed around the bulk of the second phase. The different thermal diffusivity of this thin layer would act the same as boundary mismatch that prevents the otherwise normal flow of heat. The thermal conductivity of the mismatch layer was set to one tenth (0.1), one fifth (0.2) and one half (0.5) of that of the second phase bulk. The thickness of this layer was set to 1mm (small enough value compared to the sample size) in all cases. The rest of the set-up is the same as before, meaning that the thermal conductivity of the second phase bulk is twice as much as the background, and there are two measurement points at (0 ,0) and (0, 2.8).

The model was run for the ring shape similar to Figure 5.7, for a square shaped second phase bulk centered at midway between the two measurement points (point (0, 1.4)) and for rectangles with variable lengths and widths.

Figure 5.15 shows the ring-shaped set-up where the thickness of the ring changes from 0.2cm to 2.2cm while there is one constant 0.1cm thick layer of the third phase (mismatch) on the outer layer of the ring. The results are shown in Figure 5.16.

It can be seen in Figure 5.16 that in the beginning, when the thickness of the ring (the second phase) is small and in the same order to that of the mismatch, the low thermal conductivity of the mismatch layer is the dominant factor in the overall thermal diffusivity and makes it decrease with the thickness of the second layer. But at some

minimum point (thickness=1cm here), the thicker second layer overcomes the mismatch effect and the overall thermal diffusivity starts to increase. This shows that depending on the thermal diffusivity difference and the amount of dislocations at the boundary, there can be major effects on the overall thermal diffusivity between the two measurement points.

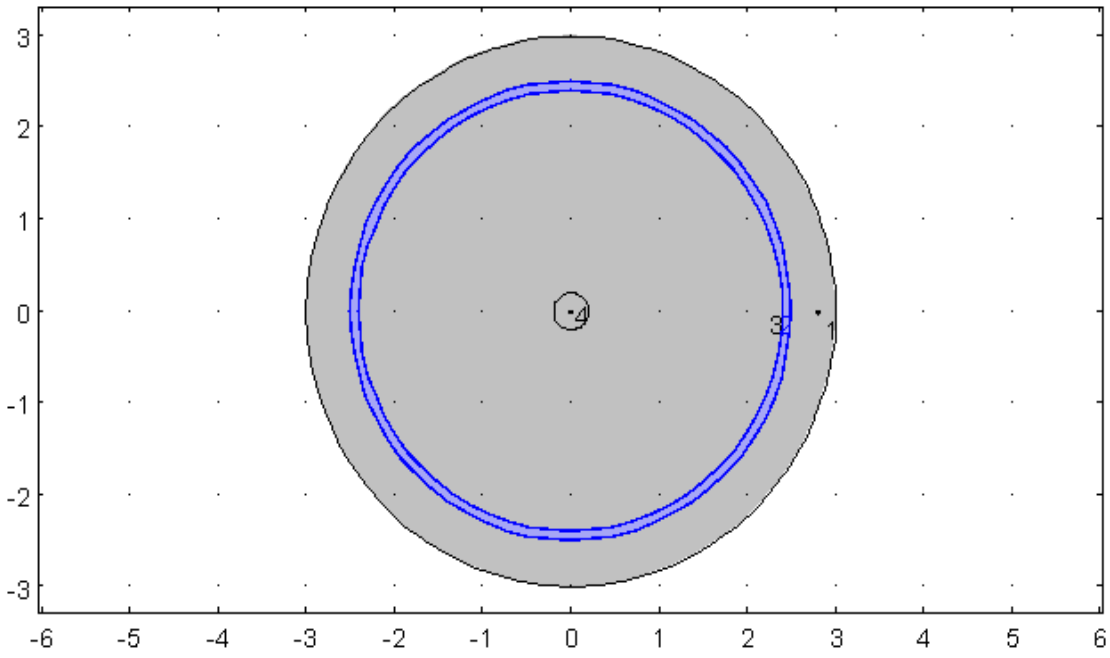

Figure 5.15 The ring shaped second phase bulk with a 0.1cm thick layer of mismatch layer with thermal conductivity of 0.1 that of the second phase

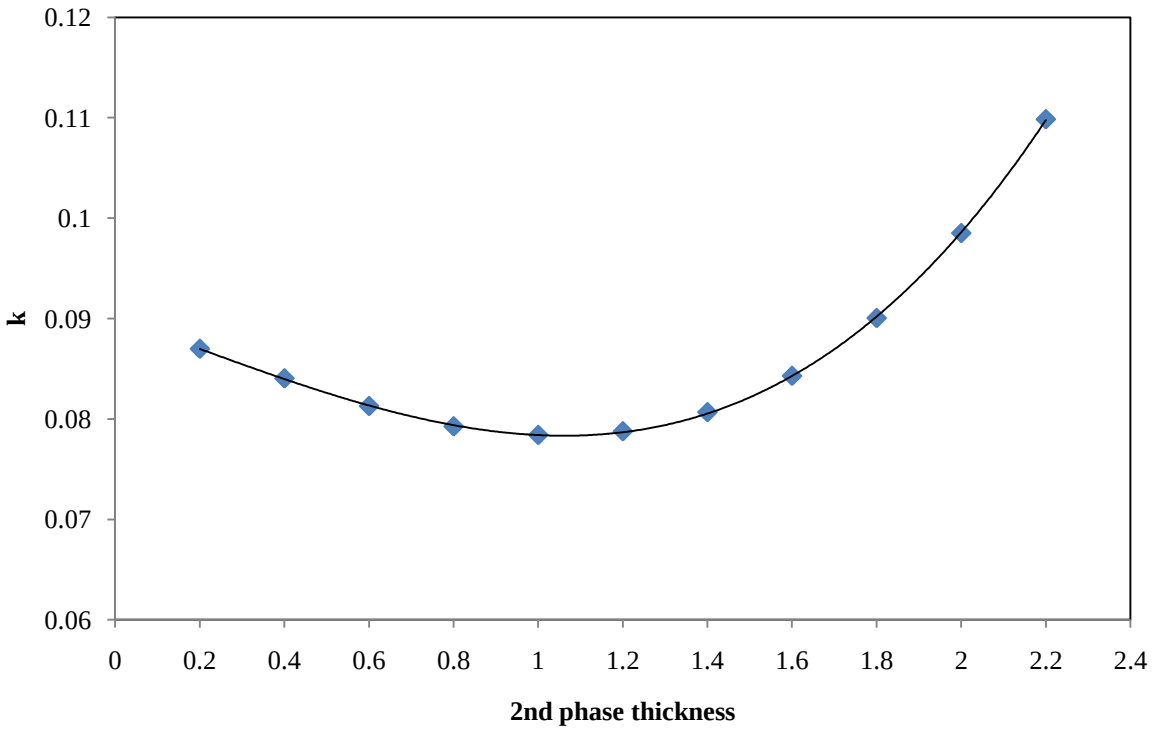

Figure 5.16 The effect of the thickness of the second phase ring with mismatch layer on the overall thermal diffusivity between the two measurement points

The next model is a square centered on the (0, 1.4) point halfway between the two measurement points, with a 0.1cm thick mismatch layer again with thermal conductivity 10 times smaller than that of the second phase, increasing in size from 0.2cm to 2.2cm.

Figure 5.17 shows the square at the beginning and the end size (0.2 and 2.2cm) with the mismatch layer highlighted. The results are shown in Figure 5.18.

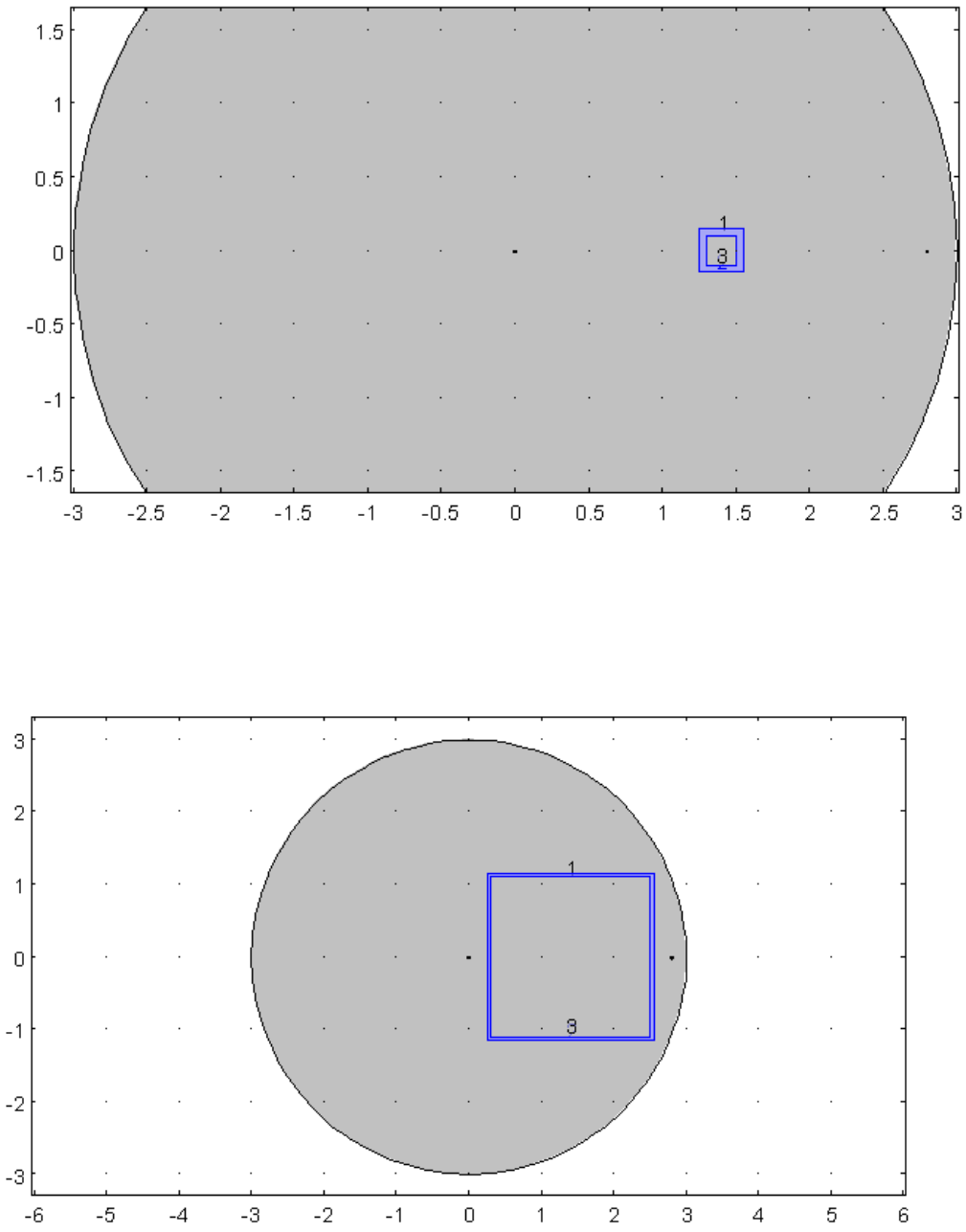

Figure 5.17 The Square shaped second phase bulk at two different sizes with the mismatch layer highlighted

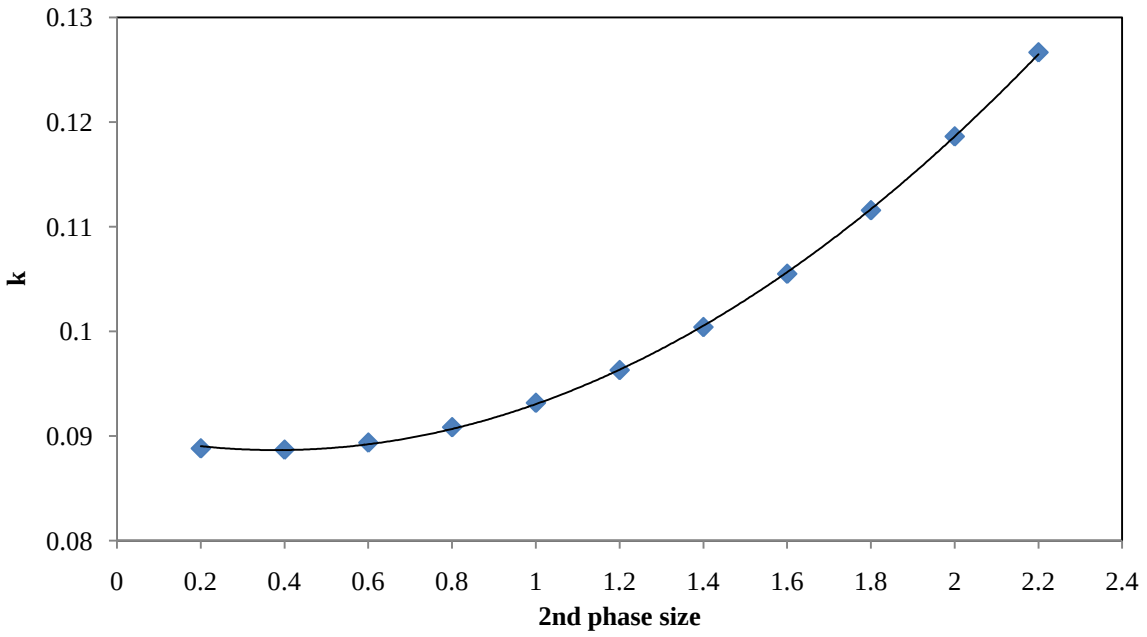

Figure 5.18 The effect of the square shaped second phase size with a mismatch layer on the overall thermal diffusivity of the sample

In this case it can be seen that as the size of the second phase increases by a factor of 2, the overall thermal diffusivity shows a slight decrease showing that the low thermal conductivity mismatch layer is dominant to this point, but after the size increases more, the overall thermal diffusivity starts to increase.

In the next model, the width of the second phase is held constant (once at 1cm and once at 0.2cm), and the length is increased as much as the geometry allows. This is repeated for 3 cases where the thermal conductivity of the mismatch layer is 0.1, 0.2 and 0.5 of the thermal conductivity of the second phase. It should be noted that the thermal conductivity of the background phase is also half of that of the second phase.

Figure 5.18 shows the results of the thermal diffusivity (slope) versus the length of the second phase, where the thickness of the second phase is 1cm and the thickness of the mismatch layer is 0.1cm. The three curves in the graph show the three cases where the thermal conductivity of the mismatch layer is one tenth, one fifth and one half of that of the second phase.

It can be seen in Figure 5.19 that when the mismatch layer is stronger (blue line), the increase in the second phase can not affect the overall thermal diffusivity much because of the dominance of the mismatch layer. In the case where the thermal conductivity difference is less (red line), the overall thermal diffusivity increases with length of the second phase, but the mismatch layer still slows down the increase compared to the case where the mismatch layer has a thermal conductivity similar to that of the background (green line).

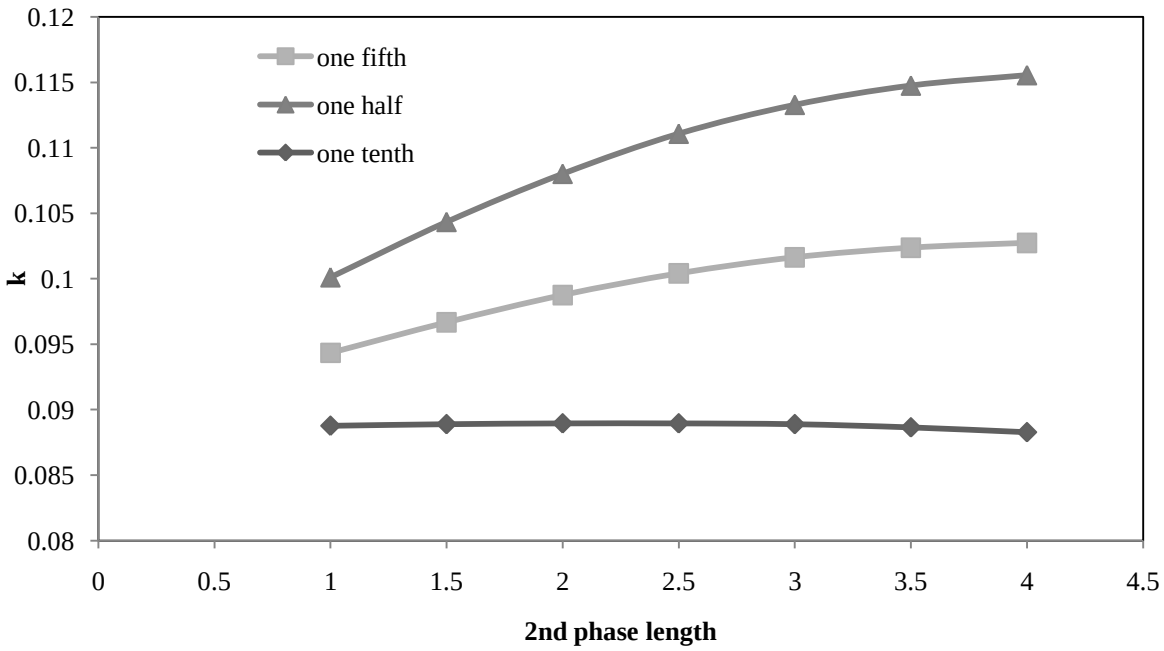

Figure 5.19 The thermal diffusivity versus the length of the second phase bulk with 1cm width and a mismatch layer of 0.1cm thickness. The thermal conductivity of the mismatch is 0.1, 0.2 and 0.5 of that of the second phase.

Figure 5.20 shows the same case with the only difference being the width of the second phase bulk (0.2cm in this case). It can be seen that in this case, since the thickness (width) of the second phase is smaller, the mismatch layer has a more dominant effect and when the mismatch layer is 10 times less conductive, the overall thermal diffusivity decreases considerably although the length of the second phase is increasing. Even when the mismatch layer conducts the heat 5 times slower that the second phase (red line) the overall thermal diffusivity decreases, and it only increases when the mismatch layer has a thermal conductivity in the same order as the background.

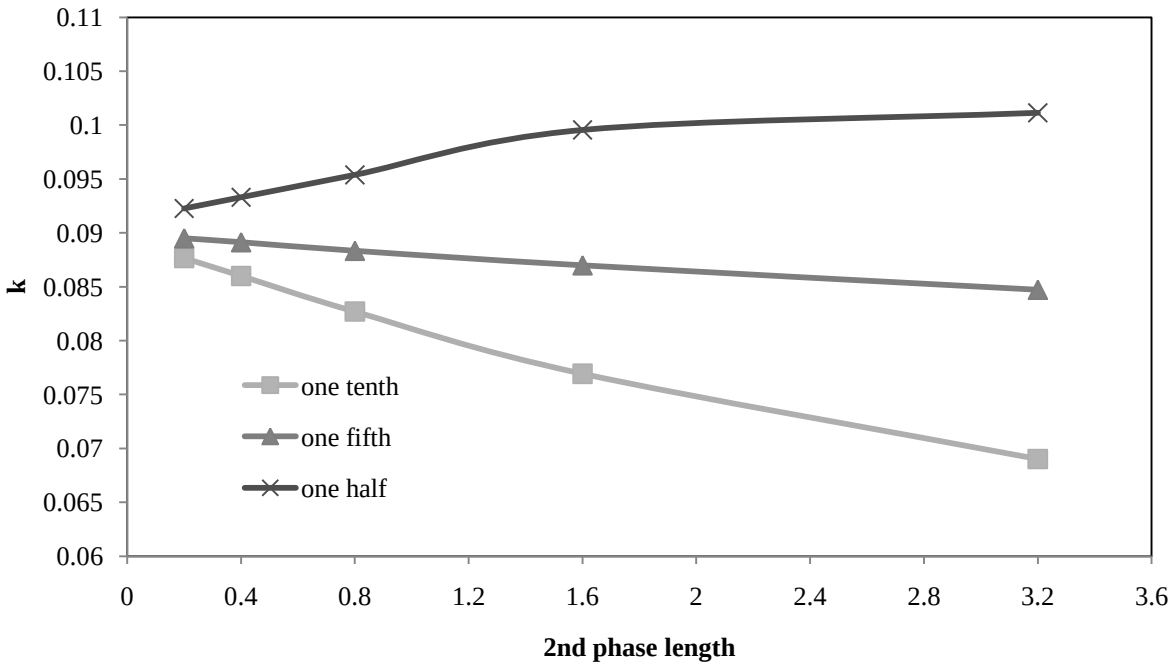

Figure 5.20 The thermal diffusivity versus the length of the second phase bulk with 0.2cm width and a mismatch layer of 0.1cm thickness. The thermal conductivity of the mismatch is 0.1, 0.2 and 0.5 of that of the second phase.

In order to show this effect more clearly, the thermal diffusivity versus the ratio of the thermal conductivity of the mismatch layer to the second phase is determined at each length in Figure 5.21. This shows more clearly how when the thermal conductivity difference between the mismatch layer and the phases is high, the bigger second phase (blue line) shows the lowest thermal diffusivity but it shows the highest value when the mismatch layer has similar thermal conductivity to that of the background.

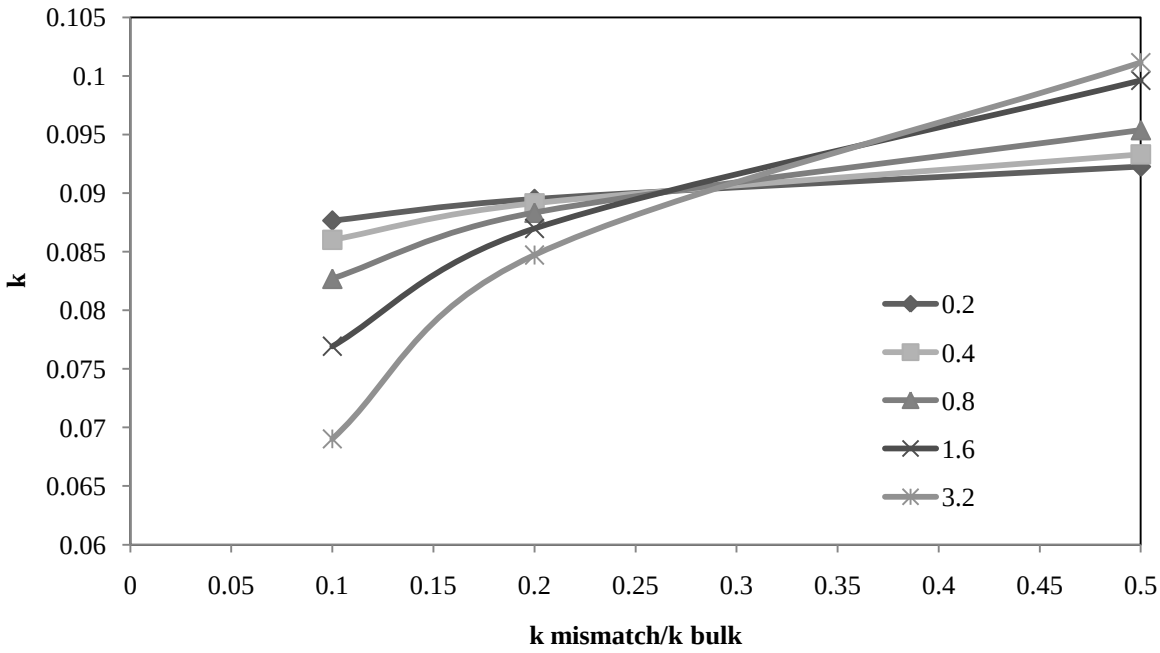

Figure 5.21 The overall thermal diffusivity versus the ratio of the thermal conductivities of the mismatch layer and the second phase of 5 different lengths of the second phase. The width of the second phase is held constant at 0.2cm with 0.1cm thick mismatch

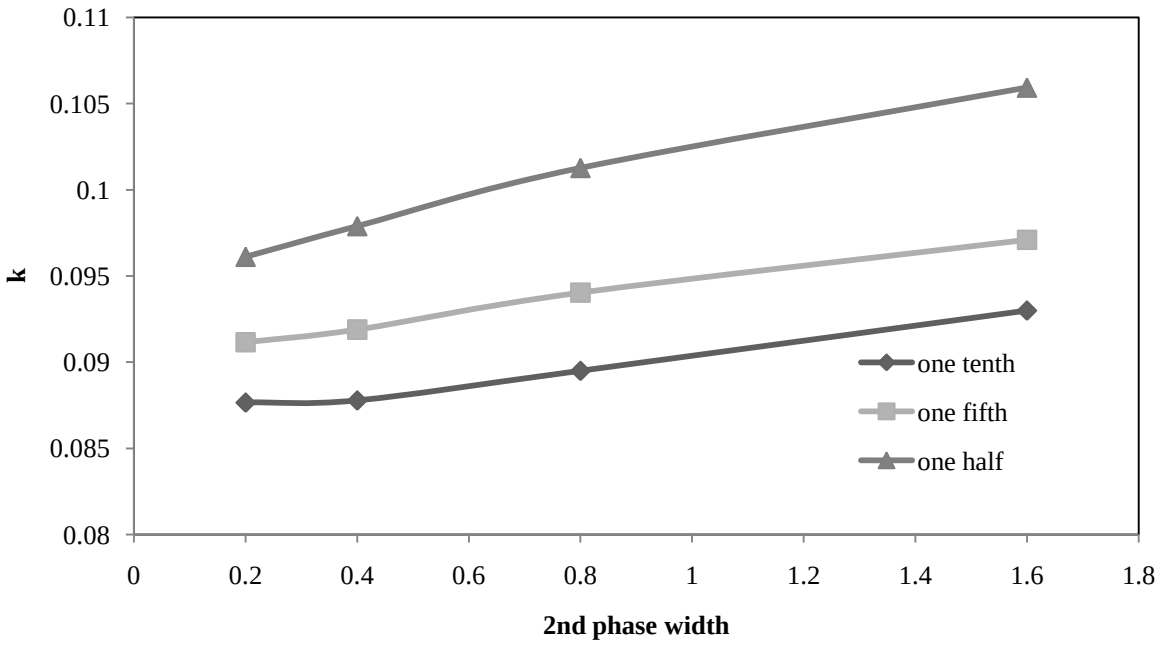

Figure 5.22 The thermal diffusivity versus the width of the second phase bulk with 0.2cm length and a mismatch layer of 0.1cm thickness. The thermal conductivity of the mismatch is 0.1, 0.2 and 0.5 of that of the second phase.

CHAPTER 6
CONCLUSIONS

In this work a reduced solution of the heat transfer in a cylinder was used to determine the thermal diffusivity of three different solder alloys and their intermetallic compounds from room temperature to up to 120°C. The alloys consist of the hypoeutectic SAC405, the hypereutectic SAC305, and the eutectic SAC387. The intermetallic compounds at this composition are Ag_3Sn and Cu_6Sn_5 for which the thermal diffusivity values have been measured for the first time in this work.

The intermetallic compounds showed a consistent behavior at different points in the sample and in their behavior with respect of temperature. The thermal diffusivity of the Cu_6Sn_5 alloy showed a slight increase with temperature from 0.1907cm^2/s at 20.2°C to 0.2016cm^2/s at 78.1°C. The Ag_3Sn alloys though, shows a constant thermal diffusivity of 0.17cm^2/s as the temperature rises.

The thermal diffusivity of the solder alloys on the other hand, showed considerable dependence on the microstructure. SAC305 and SAC405 show as much as 300% difference in thermal diffusivity across the samples. The eutectic SAC387 showed a more consistent behavior compared to the other two alloys. The study of the microstructure also shows that this alloy has a comparatively more uniform structure than the others.

The experiment was repeated after a year for comparison, and the considerable difference between the results from “as-received” samples with those of the “processed” ones show that the thermal processing the samples went through has caused changes in the microstructure of the samples which lead to considerably different thermal diffusivity values.

COMSOL Multiphysics was used to simulate the dependence of the overall thermal conductivity on the size, distribution and direction of the second phases. Also the effect of grain boundary mismatch and dislocations was simulated using a thin layer of low thermal diffusivity layer around the modeled second phases. It showed that the presence of dislocations decreases the overall thermal diffusivity and the magnitude of this effect depends on both the density of the dislocations (here shown by the difference in the thermal diffusivity of the mismatch layer and that of the second phase), and the size and direction of the second phase.

The thermal diffusivity of the solder alloys is always considered a given parameter, constant at each temperature, in design of the components. But this work shows that the properties are structure dependent and the microstructure needs to be controlled to have the desired thermal diffusivity in the joint.

CHAPTER 7
FUTURE WORK

The main issue in this study was the non-uniform microstructure across the sample which leads to non-uniform thermal properties. In this regard, the best suggestion for future work would be to develop a process to control the grain structure by rapid solidification rates and also directional solidification. By controlling the solidification speed and direction, one can control the grain boundaries, hence the density of dislocations, and also the direction of grains and dendritic structures.

The long-term aging behavior of the solders also needs to be studied while at use on the electronic boards rather than in bulk. It should be determined when the difference in the thermal diffusivity at different grain structures comes into play as far as affecting the reliability of the components.

REFERENCES

1] Salazar et al. Thermal diffusivity of nonflat plates using the flash method. Review Of Scientific Instruments (2011) vol. 82 (1) pp. 014902.

[2] S. Carslaw and Conrad Jaeger. The conduction of heat in solids. (1959) pp. 510.

[3] Bison et al. Cross-comparison of thermal diffusivity measurements by thermal methods. Infrared Physics and Technology (2002) vol. 43 pp. 127-132.

[4] Parker et al. Flash Method of Determining Thermal Diffusivity, Heat Capacity and Thermal Conductivity. Journal of Applied Physics (1961) vol. 32 pp. 1679-1684.

[5] Cernuschi et al. Comparison of thermal diffusivity measurement techniques. Infrared Physics and Technology (2001) vol. pp. 211-221.

[6] A. J. Angstrom. A new method of determining the thermal conductivity of bodies. Philosophy Magazine (1863) vol. 25 pp. 130.

[7] A. M. Bouchard. Angstrom's method of determining thermal conductivity (2000) pp. 1-4.

[8] Banish et al. Real-time determination of thermal diffusivity in a disk-shaped sample: Applications to graphite and boron nitride. Review Of Scientific Instruments (2000) vol. 71 (12) pp. 143-148.

[9] Brantschen et al. Review Of Scientific Instruments. (2004) vol. 75 (9).

[10] H. Hernandez. Thermal diffusivity measurements in curing portland cement: A Thesis (2006) The University of Alabama in Huntsville.

[11] B. K. Seelig. A study of lead-free solder alloys (1995) vol.(1) pp. 7-9.

[12] Sundelin et al. Mechanical and microstructural properties of SnAgCu solder joints. Materials Science and Engineering A (2006) vol. 420 pp. 55-62.

[13] S. Nurmi. The effect of solder paste composition on the reliability of SnAgCu joints. Microelectronics Reliability (2004) vol. 44 (3) pp. 485-494.

[14] Park et al. Measurement of deformations in SnAgCu solder interconnects under in situ thermal loading. Acta Materialia (2007) vol. 55 (9) pp. 3253-3260.

[15] Janne et al. Mechanical and microstructural properties of SnAgCu solder joints. Materials Science and Engineering A (2006) vol. 420 pp. 55-62.

[16] Kang et al. Controlling Ag3Sn plate formation in near-ternary-eutectic Sn-Ag-Cu solder by minor Zn alloying. Journal of Materials (2004) vol. 56 (6) pp. 34-38.

[17] Berthou et al. Microstructure evolution observation for SAC solder joint: Comparison between thermal cycling and thermal storage. Microelectronics Reliability (2009) vol. 49 (9-11) pp. 1267-1272.

[18] Pang et al. Microstructure and intermetallic growth effects on shear and fatigue strength of solder joints subjected to thermal cycling aging. Materials Science and Engineering: A (2001) vol. 307 (1-2) pp. 42-50.

[19] Peng et al. Effect of thermal aging on the interfacial structure of SnAgCu solder joints on Cu. Microelectronics Reliability (2007) vol. 47 (12) pp. 2161-2168.

[20] D. Yu. Improvement on the microstructure stability, mechanical and wetting properties of Sn-Ag-Cu lead-free solder with the addition of rare earth elements. Journal of Alloys and Compounds (2004) vol. 376 (1-2).

[21] The COMSOL group. http://www.comsol.com/company/

[22] A. Bradji and E. Holzbecher. On the convergence order of COMSOL solutions. Proceeding of COMSOL Conference (2007) vol. 3 pp 2-7.

[23] NIST Phase Diagrams & Computational Thermodynamics. http://www.metallurgy.nist.gov/phase/solder/solder.html

[24] The Engineering Toolbox. http://www.engineeringtoolbox.com/air-properties-d_156.html

[25] N. B. Warkaftig. Handbook of thermal conductivity of gases (1993) CRC press.

[26] Forest Products Laboratory. http://www.fpl.fs.fed.us/documnts/fplgtr/fplgtr190/Chapter_01.pdf

[27] HukseFlux Thermal Sensor Website. http://www.hukseflux.com/thermalScience/thermalConductivity.html

[28] The Engineering Toolbox. http://www.engineeringtoolbox.com/thermal-conductivity-liquids-d_1260.html

[29] National Physical Laboratory of United Kingdom Online resource. http://www.kayelaby.npl.co.uk/general_physics/2_7/2_7_9.html

[30] Engineering Edge Online Resource. http://www.engineersedge.com/properties_of_metals.htm

[31] Good Fellow Online Resource. http://www.goodfellow.com/E/Stainless-Steel-AISI-410.html

[32] The Engineering Toolbox. http://www.engineeringtoolbox.com/thermal-conductivity-metals-d_858.html

[33] J. Wilson. Thermal diffusivity. Electronics Cooling (2007).

[34] R. Reed-Heel and R. Abbaschian. Physical metallurgy principles 4th edition (2008) pp. 168-170.

[35] E. O. Hall. Proceeding of physical society of London (1951) vol. B64 747.

[36] N. J. Petch. The cleavage strength of polycrystals. Journal of Iron and Steel Instruments (1953) vol. 174 (25) pp. 743-752.

[37] Hopkins et al. Effect of dislocation density on thermal boundary conductance across GaSb/GaAs interfaces. Applied Physics Letters (2011) vol. 98 (16).

[38] G. Z. Voyiadjis and F. H. Abed. Effect of dislocation density evolution on the thermomechanical response of metals with different crystal structures at low and high strain rates and temperatures. Archive of Mechanics of Polish Academy of Science (2005) vol. 57 (4) pp. 299-343.

[39] Y. S. Touloukian. Thermal diffusivity (1973) New York IFI.